THE UNIVERSITY *of* EDINBURGH

An Image Analysis-Based Framework for Adaptive and Focal Radiotherapy

Yang Feng

Doctor of Philosophy

THE UNIVERSITY OF EDINBURGH

March, 2015

Abstract

It is estimated that more than 60% of cancer patients will receive radiotherapy (RT). Medical images acquired from different imaging modalities are used to guide the entire RT process from the initial treatment plan to fractionated radiation delivery. Accurate identification of the gross tumor volume (GTV) on computed tomography (CT), acquired at different time points, is crucial for the success of RT. In addition, complementary information from magnetic resonance imaging (MRI), positron emission tomography (PET), cone-beam computed tomography (CBCT) and electronic portal imaging device (EPID) is often used to obtain better definition of the target, track disease progression and update the radiotherapy plan. However, identifying tumor volumes on medical image data requires significant clinical experience and is extremely time consuming. Computer-based methods have the potential to assist with this task and improve radiotherapy. In this thesis a method was developed for automatically identifying the tumor volume on medical images. The method consists of three main parts: (1) a novel rigid image registration method based on scale invariant feature transform (SIFT) and mutual information (MI); (2) a non-rigid registration (deformable registration) method based on the cubic B-spline and a novel similarity function; (3) a gradient-based level set method that used the registered information as prior knowledge for further segmentation to detect changes in the patient from disease progression or regression and to account for the time difference between image acquisition. Validation was carried out by a clinician and by using objective methods that measure the similarity between the anatomy defined by a clinician and by the method proposed. With this automatic approach it was possible to identify the tumor volume on different images acquired at different time points in the radiotherapy workflow. Specifically, for lung cancer a mean error of 3.9% was found; clinically acceptable results were found for 12 of the 14 prostate cancer cases; and a similarity of 84.44% was achieved for the nasal cancer data. This framework has the potential ability to track the shape variation of tumor volumes over time, and in response to radiotherapy, and could therefore, with more validation, be used for adaptive radiotherapy.

Acknowledgements

I'd like to thank my supervisors Prof. David Argyle, Dr. William Nailon and Dr. Duncan McLaren for being patient and supportive of my research. I would also like to thank Prof. Stephen McLaughlin for providing thoughtful advice and Dr. Lisa Forrest for help with the veterinary data collection. I must also thank Dr. Jessica Lawrence for her collaboration on the application of the registration-segmentation framework on veterinary patients. I am also grateful for the help of my colleagues Dean Montgomery, Kun Cheng, Dan Welsh, Roushanak Ramat and Fraser Robinson.

I need to thank my parents for funding my living expenses during the past three years and thank my wife for being patient of my work and taking care of my life.

I am grateful for the generous support from NHS Lothian, Edinburgh and Lothians Health Foundation (charity number SC007342), the James Clerk Maxwell Foundation, the Jamie King Uro-Oncology Endowment Fund, a University of Edinburgh Darwin Award and a University of Edinburgh Individual Stipend.

Declaration

I declare that this thesis was composed by myself, that the work contained herein is my own except where explicitly stated otherwise in the text, and that this work has not been submitted for any other degree or professional qualification except as specified.

Yang Feng

Acronyms and Abbreviations

2D/3D/4D	Two/Three/Four dimensional
ANN	Artificial neural network
ART	Adaptive radiotherapy
CBCT	Cone-beam computed tomography
CRT	Conformal radiation therapy
CT	Computed tomography
CTV	Clinical target volume
DICOM	Digital Imaging and Communications in Medicine
DNA	Deoxyribonucleic acid
DOG	Difference-of-Gaussian
DR	Distinctive regions on the reference image
DRR	Digitally reconstructed radiograph
DT	Distinctive regions on the target image
EBRT	External beam radiotherapy
EPID	Electronic portal imaging device
FAIR	Flexible algorithms for image registration
FDG	Fluoro-deoxyglucose
FFD	Free form deformable registration
FLIRT	Flexible linear image registration toolkit
FLT	Fluorothymidine
GR	Gabor feature elements on the reference image
GT	Gabor feature elements on the target image
GTV	Gross tumor volume
IGART	Image guided adaptive radiation therapy
IGRT	Image guided radiation therapy

IMRT	Intensity modulated radiation therapy
IORT	Intraoperative radiotherapy
IR	Interventional radiology
ITK	Insight segmentation and registration toolkit
keV	Kilo electron voltage
linac	Linear accelerator
MeV	Mega electron voltage
MI	Mutual information
MLC	Multi leaf colimator
MRI	Magnetic resonance imaging
MU	Monitor unit
OAR	Organ at risk
OBI	On Board Imager
PET	Positron emission tomography
PTV	Planning target volume
RCS	Reference coordinate system
RF	Radio frequency
RFD	Reference feature descriptor
RFP	Feature points on the reference image
RT	Radiotherapy
SBRT	Stereotactic body radiation therapy
SIFT	Scale invariant feature transform
SPECT	Single-photon emission computed tomography
SRS	Stereotactic radiosurgery
SRT	Stereotactic radiation therapy
SSD	Sum of squared distance
SUV	Standardized uptake value
SVM	Support vector machine

TFD	Target feature descriptor
TFP	Feature points on the target image
TPS	Thin-plate spline

Nomenclature

T_x, T_y, T_z	Translation parameters in rigid registration
α, β, γ	Rotation parameters in rigid registration
μ_X	Average attenuation coefficient of X
I/G	Image intensity or gray value
$DeT(P)$	Delaunay triangulation for a set of points P
Pe	Intensity value of salt and pepper noise
Po	Probability of every pixel in an image being a noisy pixel (salt and pepper)
IDO	Injected dose after decay correction
SUV_{max}	The maximum of SUV in the image
H	Hessian matrix
$H(A)$	Entropy of A
G/D	Gaussian function/Difference-of-Gaussian function
σ	Standard deviation
Tr	Trace
Det	Determinant
n_d	Size of SIFT descriptor
n_f	Number of selected feature points
n_g	Number of Gabor features for every pixel
n_m	Number of selected matches between feature points
T_{best_rigid}	The optimized rigid transformation
ϕ	Phase offset
θ	Orientation
ζ	Spatial aspect ratio
C	Criteria
$T_{best\_nonrigid}$	The optimized non-rigid transformation

Δt	Time interval
u	Level set function
$C_R/C_T/C_G$	Reference/Target/Automatic generated contour
R1/R2/R3/R4	Ratios defined to evaluate the volume of the focal region inside the prostate
V_{MRI_Focal}	The original focal volume on MRI images
$V_{CT\_Original\_Focal}$	The original focal volume on CT images
$V_{CT\_Rigid\_Focal}$	The rigidly registered focal volume on CT images
$V_{CT\_Nrigid\_Focal}$	The non-rigidly registered focal volume on CT images
$V_{In\_1}/V_{In\_2}/V_{In\_3}/V_{In\_4}$	The overlap volume between V_{MRI_Focal}, $V_{CT\_Original\_Focal}$, $V_{CT\_Rigid\_Focal}$, $V_{CT\_Nrigid\_Focal}$ and their corresponding prostate respectively

Contents

Figures and Tables

Figures

Tables

Chapter 1

Introduction

1.1 Introduction

RT or radiation therapy is a commonly used treatment approach based on ionizing radiation to control or kill malignant cells. RT is curative in many types of cancers that have localized tumor volume and has proven to be synergistic with chemotherapy [49]. In general, radiation is delivered to cancer cells and works by damaging the Deoxyribonucleic acid (DNA) of cancerous tissue leading to cellular death. Although abnormal cancer cells are more sensitive to radiation and divide more quickly than normal cells, which can repair themselves more effectively, the goal of RT is to maximize the dose delivered to cancer cells and minimize the dose delivered to healthy tissues [43]. There are several different types of RT methods that are suitable in different situations such as external beam radiotherapy (EBRT), internal radiotherapy (brachytherapy) and intraoperative radiotherapy (IORT) which will be introduced in Section 2.2.

Different RT approaches can be combined with each other or with other treatment methods to achieve the best clinical outcome. However, all types of EBRT methods follow the same general principles: 1. Precisely locate the target. 2. Accurately direct the radiation beam. 3. Deliver a radiation dose that damages abnormal cells and spares normal cells [18]. In practice this translates into the typical patient journey shown in Figure 1.1. The field of RT has gained substantial momentum in recent decades with significant advances in conformal treatment planning, image guided radiation therapy (IGRT) and intensity modulated radiation therapy (IMRT) techniques. As medical images with information from structural, functional and histological sources providing disease-specific insights are now used to guide the process of RT, improvements have been made in image alignment (registration), target volume delineation, and identification of critical structures [108]. There is a large body of evidence supporting the use of RT for optimal local tumor control, therefore identification of the tumor volume is of utmost importance when determining a treatment plan or evaluating changes in tumor volume. Although accurate segmentation results are required for this, currently there is no single solution for it. A typical IGRT process where image registration is vital in order to merge information from multi-modality images and therefore provide accurate guidances for RT delivery is illustrated in Figure 1.2.

Figure 1.1: Left: the four steps of curative RT. Right: illustration of the Novalis RT platform for stereotactic radiosurgery and stereotactic body radiation therapy. The orthogonal beams are used to obtain images of a patient with brain cancer on a flat treatment couch [31].

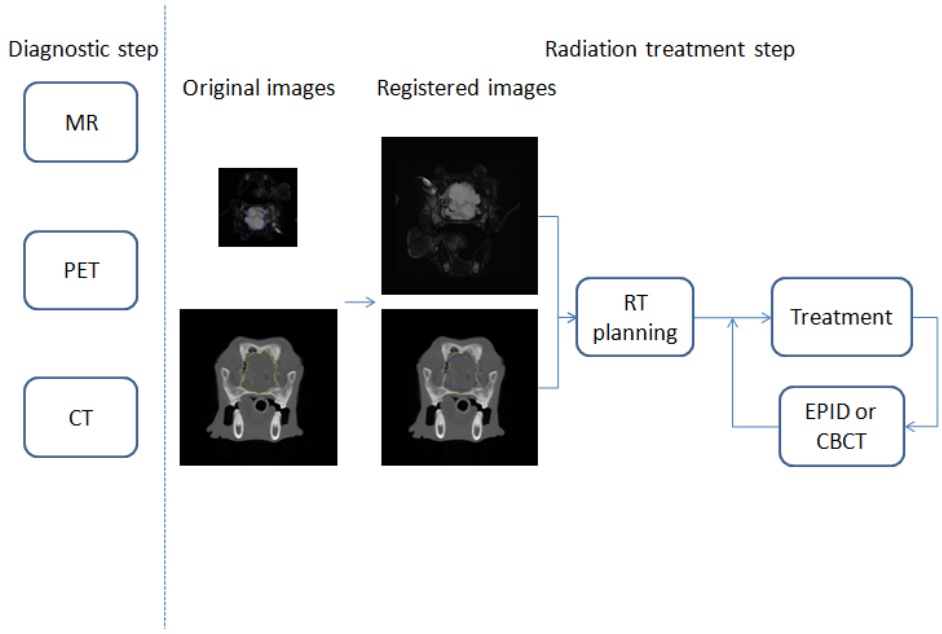

Figure 1.2: A typical IGRT workflow in the case of a canine nasal tumor, highlighting the need for registration, using a canine nasal tumor as an example. Diagnostic images are obtained and registered to the reference image for treatment-planning. Each fraction of radiation is administered with the aid of EPID or CBCT images that are registered to the treatment-planning reference image.

However, in practice, a significant amount of manual effort is needed in the process of RT, especially in tumor segmentation. Therefore, medical image processing is used to improve the accuracy of radiation delivery and to assist clinicians by providing efficient and objective segmentation techniques.

1.2 Similarity between veterinary and human cancer

There are many similarities between human and veterinary cancers, which forms the basis of comparative oncology. In the case of medical image processing, approaches applied to humans can be suitable for veterinary patients and the opposite is also true. The concept of comparative oncology is not new and most often refers to the study of cancer etiology, biology and treatment in companion animals that develop spontaneously-occurring cancer.

In oncology, the comparative studies can help reveal some lesser known aspects, such as the more or less exclusive appearance of certain neoplasms in one species or another, and the involvement of some organs or tissues common to several species, but with the maintenance of differences between the various species. Comparative oncology has developed into two branches: spontaneous oncology and experimental oncology. Spontaneous oncology focuses on the research of spontaneous tumors and helps understand the disease by comparing results obtained from animals with humans. Experimental oncology is more concerned with scientific investigations, the knowledge of this field is always acquired from a large amount of results under experimental conditions.

Testing image processing algorithms on both patient groups presents a unique opportunity to improve RT given that each patient group has its own advantages for image studies. Image registration is a vital branch of image processing, it is defined as the process of aligning two or more images from the same or different imaging modalities. It provides a geometric transform that makes it possible to map information between the images, often with sub-pixel resolution. Image registration and data fusion are useful in veterinary radiation oncology and often occur without regard to the robustness of the technique and without mention in the reporting of radiation studies. Most modern treatment planning systems allow for use of datasets (often termed secondary datasets) in addition to the treatment-planning CT for target and OAR delineation and visualization. Likewise, many systems permit the inverse transformation, where dose information can be transferred to the secondary dataset. Limitations in veterinary reporting of RT planning, dose and delivery have recently been highlighted so it is no surprise that differences undoubtedly exist across institutions and board-certified radiation oncologists [64].

Dose distributions generated for conformal radiation therapy (CRT) have been accurately predicted with CT-based treatment planning systems and are already widely used in veterinary

oncology [69]. CT data includes the Hounsfield units as a linear transformation of radiation beam attenuation that varies with electron densities of materials as the beam progresses through tissue. Most RT planning software obtains the relative electron density from the relationship between the linear attenuation coefficients and Hounsfield unit values in order to determine heterogeneity in the body. Non-contrast CT images are typically utilized for treatment planning, given that contrast agents are high-Z radio-opaque materials, which would attenuate a radiation beam more than normal, resulting in higher than normal electron density. Post-contrast CT data used for a treatment plan would theoretically give rise to higher monitor unit (MU) values, and therefore radiation dose, compared to MU values taken from calculating a plan using pre-contrast CT data. As veterinary radiation oncologists often use commercially available human treatment planning software, automatic registration methods may be built-in to the software, although other "in house" registration algorithms may be adapted for use [47, 67, 72, 90, 93, 115]. One of the most common automatic registrations used in routine treatment planning is the merging of pre-contrast and post-contrast CT data in order to delineate the GTV, CTV, PTV and OAR. Because regions of interest are often best identified on post contrast CT images, many commercial software programs (such as Eclipse, Varian Medical Systems, Palo Alto) automatically permit Digital Imaging and Communications in Medicine (DICOM)-coordinated registration and facilitate contouring on fused multi-modality images. This eliminates a potential source of error as radiation oncologists historically may have estimated tumor volume on the pre-contrast CT data based on visual examination of alternative imaging studies. Evaluating the veterinary literature to date, it is often difficult to firmly understand how tumor volumes were identified prior to treatment; for example in one study evaluating RT for canine intracranial tumors, the GTV was defined on planning CT scans by the contrast-enhancing area on CT or MRI data [105]. It is presumed that contours for the GTV were drawn on pre-contrast CT images after evaluation of diagnostic scans, however this presumption may be incorrect. In most other veterinary studies, it is unclear how the GTV was derived, as irradiated volumes have been inconsistently defined [64]. The delineation of target volumes is paramount to effective RT, as geographic miss could occur if the GTV, CTV and PTV are ineffectually contoured and/or unexpected toxicity could result from a poorly defined OAR. As veterinary reporting of RT planning improves, information regarding registration should be included.

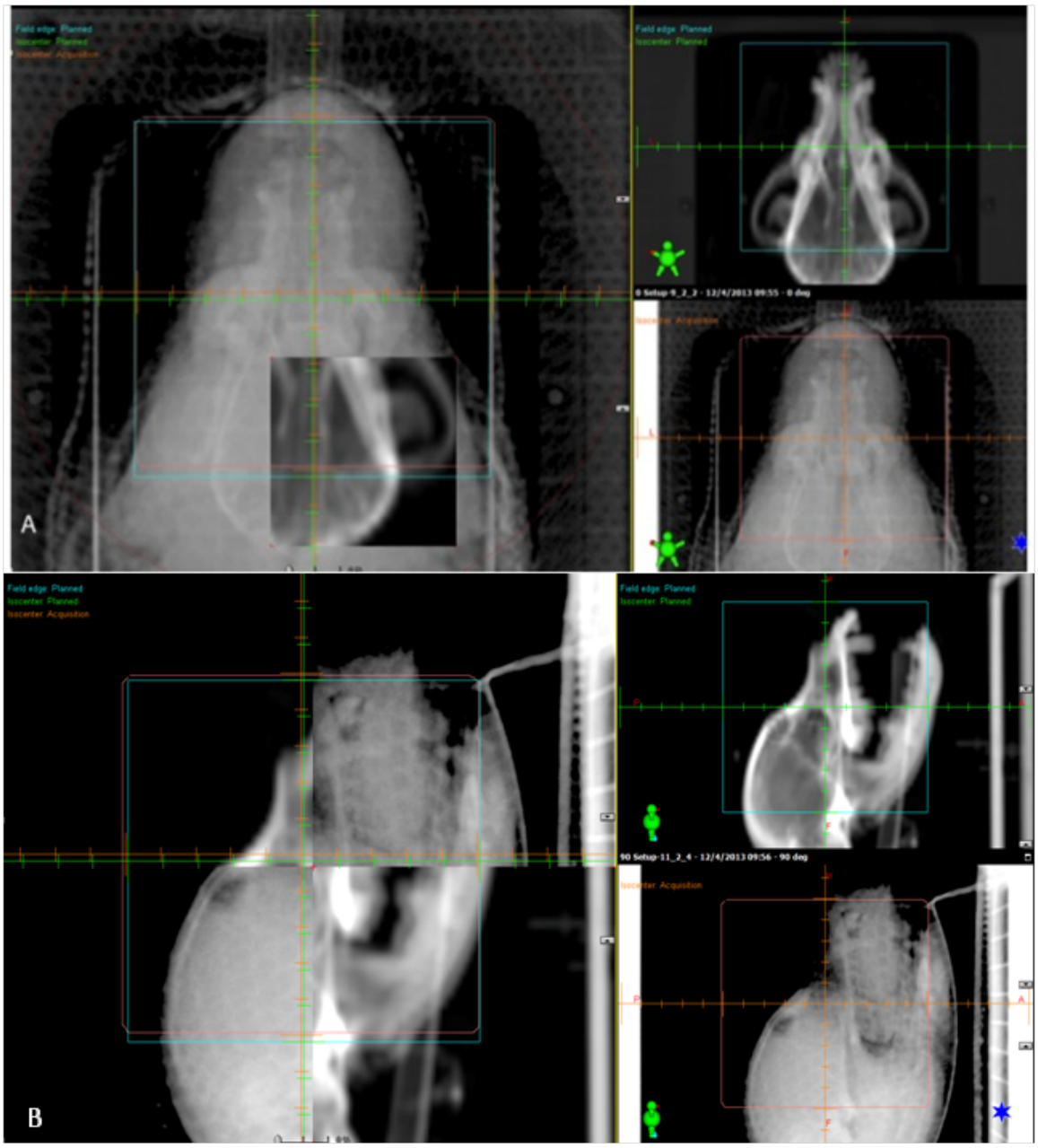

Figure 1.3: Portal images obtained from a dog with a sinonasal tumor undergoing definitive intent radiation therapy; orthogonal images were obtained and analyzed immediately prior to treatment delivery.

In addition to RT planning, image registration has made its way into the routine assessment of daily patient positioning, enabling better tumor targeting [61, 86, 91]. One of the key concepts of IMRT, stereotactic radiation therapy (SRT) or SRS and IGRT planning is that tight dose constraints can be placed around the PTV provided the clinician is confident that the patient's positioning will be reproducible during treatment. One of the most common practices immediately prior to treatment delivery is to generate a pair of orthogonal DRR images from the

planning CT images and to register simulated radiographs with MV radiographs acquired by a flat-panel imager (EPID) attached to the linear accelerator (Figure 1.3) [61, 86]. More advanced OBI (On Board Imager) equipment involves cone-beam CT systems or helical CT systems built into the treatment unit [91]. Automated image registration at the treatment unit can use successively finer data resolution and MI to determine rotations and translations required to align the datasets, thus decreasing some of the variability with daily patient setup and intrapatient shifts [47, 62, 67, 72, 90, 93]. Little veterinary literature has evaluated the utility or validity of various registration algorithms other than an early study demonstrating an in-house computer program developed on the basis of an MI algorithm; the algorithm was evaluated visually [115]. This study highlighted the widespread potential of image registration by evaluating corresponding images from CT and MRI, CT images before and after surgical treatment, and CT and post-mortem cryosection images in dogs or cats [115]. Currently at our institution, for follow-up imaging, standardized response criteria are applied when assessing tumor response following treatment [29]. Responses for tumors of the head and neck (intracranial, sino-nasal, cervical) are often assessed by the radiology and radiation oncology team on serial CT scans, without consideration for image registration over time, which may not accurately reflect the response of the tumor or the assessment of treatment-induced toxicity [90]. Often toxicities are inferred by tissue changes, however easier implementation of image registration in the clinic may provide more objective information regarding tumor and normal tissue changes following radiation, particularly as varying fractionated protocols are used across veterinary radiation oncologists [69].

With the incorporation of functional imaging into veterinary oncology, determination of structural and, indirectly, pathological changes may be better assessed. Changes such as fibrosis and tumor recurrence can be difficult to distinguish on CT and MRI images; functional imaging with PET may help clarify differences and alter future therapy. 2-deoxy-2-[18F]-fluorodeoxyglucose (FDG), 3'-deoxy-3'-[18F]-fluorothymidine (FLT), and copper(II)-diacetyl-bis (N4-methylthiosemicarbazone) (Cu-ATSM) have been used to assess various neoplastic conditions in dogs and cats in veterinary medicine currently [15–17, 45, 71, 73–75, 102, 134]. In particular, several studies have evaluated functional imaging over time in an attempt to correlate pre-treatment scans to post-treatment scans; ideal comparisons would require registration of image datasets to avoid interpretation errors [15, 17, 71, 75]. One study that assessed pre-radiation therapy FDG, FLT and Cu-ATSM PET/CT scans to post-treatment FDG PET/CT scans demonstrated the complexity and utility of registration methods in dogs with sinonasal tumors [15]. Dogs in this study underwent a radiation-planning CT scan that served as the reference dataset; bony anatomy from pre-radiation PET/CT scans was registered to the bony anatomy of the radiation-planning CT; rigid registration using cross-correlation resulted in affine transformations that were applied to the corresponding PET images. The translated and rotated PET matrices were subsequently re-sampled using a spline filter defined by the reference PET image that was obtained at the same time as the treatment-planning CT [15]. While

complex, the registration process ensured that each voxel index of the pre-treatment PET/CT scans corresponded as closely as possible to the same region in the post-treatment FDG PET image for each patient, enabling assessment of changes in tracer uptake [15]. Imaging and registration advances will undoubtedly lead to more work being performed in a similar fashion and may alter current criteria for response assessment and/or response prediction.

1.3 Overview of image registration and adaptive radiotherapy

As the use of multi-modality image data in RT increases, medical image registration is essential to combine the information from each modality. As a result it has become a very active area of research [97]. In RT, images can be registered to obtain comprehensive information whether they were obtained on patients in dissimilar positions or immobilization devices, from different points of view, at various time points, or by different sensors. Registration may also be used to combine multiple images from the same imaging modality [37], or to combine information from multiple modalities such as CT, MRI, PET and single-photon emission computed tomography (SPECT) [80]. In this thesis, the reference image is defined as the source image containing the reference information while the target image is defined as the movable image spatially matched to the reference. After registration information from the reference image, for example contoured structures, can be used on the target image.

In general a course of radiotherapy is delivered over several different days or even weeks in both human and veterinary oncology. By fractionating the course in this way small non-lethal doses of radiation can be delivered at each fraction, or day, of treatment. While the GTV are currently considered standard targets in radiation oncology, the planning target volume (PTV) is created to make sure that dose plans are robust to uncertainties [2]. The GTV and clinical target volume (CTV) are oncological-anatomical concepts, which are heavily dependent on the experience and judgment of the radiation oncologist and radiologist. The PTV, on the other hand, is a geometrical scheme used for treatment planning in order to ensure that the prescribed dose targets the CTV [2]. Alternatively, one might view the PTV as decreasing the risk that patient positioning, setup uncertainties, and organ at risk (OAR) or target position uncertainties will lead to a severe under-dosage of the CTV. As the impact of setup uncertainties decreases with IGRT, the CTV to PTV margins may be reduced, thus decreasing normal tissue toxicity. Taking this a step further, if diagnostic imaging, interpretation, and registration with the initial treatment plan are performed frequently while a patient is on therapy, the treatment plan can be "adapted" to optimize tumor control and minimize normal tissue damage. Adaptive radiotherapy (ART) is defined as changing a radiation plan during RT to account for anatomy or biology changes of patients [132]. Studies have shown clear advantages and gains in clinical application of ART. However, clinical implementation is limited as ART is time-consuming and requires an additional work-load on clinicians to quickly contour follow-up images manually [132].

Adaptive planning could be used at different fractions (off-line) and at different time points within one fraction (on-line) [76]. Identifying changes in the GTV between images acquired for the purpose of RT planning and images acquired for the purpose of assessing response to RT is challenging. This is mainly because of: 1. Uncertainties of soft tissues and internal organ motion [14]. 2. The response of the GTV to radiation or other treatments is difficult to predict, which may cause anatomical changes [131]. 3. Distortions or contrast variability between different modalities, which makes it difficult to register the information between multi-modality images [38, 53]. To overcome these difficulties, image guided adaptive radiation therapy (IGART) is the most reliable method for a comprehensive ART approach [24]. Research into known, documented uncertainties in soft tissue and organ motions in prostate [120], head and neck [96] and lung [116] are well developed and directly impact ART approaches. Furthermore, registration methods that combine information and realize deformable mapping between structural and functional images are essential to make IGART more practical and enable individualized plans [55].

1.4 Motivation and contribution

The final aim of an image processing method is to find the correct GTV boundary on medical images. However, it is particularly difficult to generate a generally applicable method for it without any prior knowledge. In practice, the GTV boundaries drawn by clinicians involve not only image information but also clinical information and experience. This makes it even harder to provide accurate results for an algorithm only depending on image information.

As a result, most literature focuses on automatic or semi-automatic methods for certain types of cancers. In this thesis, the GTV contours on pre-treatment images or planning CT images generated from clinicians are taken as a prior for the post-treatment images. Rigid and non-rigid registration algorithms can map the information from the pre-treatment reference image to the post-treatment target image so that they can be used in follow up segmentation algorithms. All of them are included in an automatic registration-segmentation framework to generate a general pipeline of the GTV identification on follow up images.

Specifically, there are three main reasons for registering images from different imaging modalities.
Firstly, the registration between CBCT and planning CT images is a commonly used method to verify the position of patients receiving RT. This is usually carried out manually by radiographers, however, an automatic registration would provide a faster and more objective way of achieving registration. Here, the contribution of this work was the combination of the scale invariant feature transform (SIFT) algorithm and mutual information (MI) for rigid registration. SIFT finds key points and their descriptors and extracts robust image features. The maximum MI between SIFT features on corresponding images is used to determine the best image match.

The approach combines feature extraction and the MI similarity criterion and therefore is more focused on the representative pixels in both 2D and 3D. This rigid method has been applied to register CBCT and CT data from lung cancer patients.

Secondly, the techniques developed can assist in the delivery of boost dose to the dominant cancer focus thereby preserving the organ function. A non-rigid registration method which can simulate the distortion between images from different modalities is necessary to map the focal information from MRI to planning CT images. A major contribution of this thesis is the cubic B-spline based non-rigid registration method which can be applied after rigid registration. Here the rigid method previously mentioned was used for image conditioning, which makes the non-rigid method more accurate. A robust similarity function that includes the sum of squared distance (SSD) between corresponding feature points and MI between pathologically identified distinctive regions is used in this approach. With appropriate weights, this similarity function balances the distortion generated from corresponding Gabor feature points and the stability generated from the non-deformed distinctive regions. As a result, it can track the variation of the GTV or target organ if the feature points are extracted from corresponding contours. Data from focal prostate cancer patients has been used to assess the performance of this method.

Thirdly, the variation of the GTV between different fractions of RT limits the effectiveness of the treatment. To achieve adaptive dose planning, an automatic segmentation method is essential for the post-treatment data of patients. A further major contribution of this thesis is a registration-segmentation framework for adaptive radiotherapy (ART) which not only includes rigid and non-rigid registration algorithms but also the follow-up level set based method for segmentation. By using the registered contour as the initialization of the level set method this approach automatically finds the GTV contour on follow-up CT images. The original clinical contour on pre-treatment images is treated as a prior. Because of the similarities between cancers in humans and veterinary patients, veterinary test data sets were used to validate these algorithms. The Dice coefficient was used to assess the performance of these algorithms by comparing the automatically generated results with clinical opinions.

1.5 Outline of the thesis

In this chapter, an overview of definition, workflow and challenges in RT is presented. As the similarities between human and veterinary cancers provide a unique opportunity to improve RT, comparative oncology including a review in veterinary field is introduced in Section 1.2. Image registration is an important branch of image processing and is the most important part in this thesis. Therefore, a general introduction of image registration in RT and its application in ART are provided in Section 1.3. In Section 1.4, the specific aims of image processing for different data sets, motivations for the automatic GTV segmentation, challenges faced in developing suitable algorithms and the novelties of this thesis are presented.

In Chapter 2, background of various technical topics is introduced. Specifically, in Section 2.2, commonly used modern RT techniques and their rationales are presented. Also, the advantages and disadvantages of IGRT, IMRT, EBRT and brachytherapy are introduced. In Section 2.3, the basic definitions in the image processing field are presented. Because medical images are the main concern in this thesis, the commonly used DICOM tags and information are introduced in this Section too. Imaging techniques including both structural and functional imaging techniques are important for diagnosis, dose planning and treatment in RT. The rationals, advantages and disadvantages of them are introduced in Section 2.4. In general, transformation function, similarity function and optimization methods are the necessary parts of an image registration algorithm. A comprehensive technical review on these aspects and the classification of image registration algorithms are presented in Section 2.5. In Section 2.6, a brief overview of commonly used image segmentation techniques in medical field and its classification is presented.

In Chapter 3, technical details of all the algorithms used in this thesis are introduced. Various pre-processing (image conditioning) methods including de-nosing, re-sampling, down-sampling and pre-segmentation algorithms are presented in Section 3.2. A rigid registration method including SIFT feature extraction method and MI-based similarity function are presented in Section 3.3. In Section 3.4, a non-rigid registration method based on cubic B-spline interpolation together with the Gabor filter-based feature extraction method are introduced. The level set method, which is a robust and accurate contour segmentation algorithm, is applied after the non-rigid registration method for further segmentation and is presented in Section 3.5. Section 3.6 introduces the calculation of Dice coefficient which is the most commonly used similarity measurement between two contours in this thesis.

In Chapter 4, the test results and conclusions of the rigid registration method are presented. The Dice coefficient was used to evaluate its performance. The various test data sets are summarized in Section 4.2. As PET is an important and powerful functional imaging technique which is commonly used in modern RT, a PET pre-segmentation algorithm is introduced in Section 4.3. The test results of the SIFT-based rigid registration algorithm on phantom data, CBCT data and EPID data are presented in Section 4.4, 4.5 and 4.6 respectively.

In Chapter 5, the test results and conclusions of the non-rigid registration method are introduced. Test data for this algorithm are introduced in Section 5.2. The test results on manually warped prostate data are presented in Section 5.3. In Section 5.4, Diagnostic MRI images and planning CT images with clinically identified focal regions from prostate cancer patients are used to test the non-rigid algorithm. Because it is very difficult to assess a non-rigid algorithm judgments of clinicians are treated as the gold standard to validate the results.

In Chapter 6, a registration-segmentation framework including all the algorithms mentioned in Section 3.3, 3.4 and 3.5 is introduced. Veterinary data sets used to test this framework which include pre-treatment CT images, follow-up CT and MRI images at different time points are

summarized in Section 6.2. The basic workflow of this framework and the step by step Dice evaluation of it are introduced in Section 6.3. Test results are introduced and assessed in Section 6.4 and 6.5.

In Chapter 7, Conclusions of all the work presented in this thesis are made. Also, further work based on the discussion of the results is introduced.

Chapter 2

Background

2.1 Introduction

Medical images with information from structural, functional and histological sources can provide disease-specific insights and assist in the management of cancer patients. In the radiotherapy of the prostate, CT images are acquired to provide structural information and electron density information which can indicate the ability of materials to block the radiation beams and therefore help calculate the dose distribution. PET images and/or MRI images provide functional information to identify the biological features of tumor regions. The resolution of medical images and their ability to provide functional and structural information has significantly improved in recent years. CT images provide good structural information and MRI images provides very good soft tissue contrast. MRI perfusion can also be used as a surrogate marker of hypoxia, which is a noticeable feature of cancer cells with radiation resistance. Increasing radiation dose to hypoxic areas may improve clinical outcome. Functional image information can also be obtained from PET images which offer advantages in terms of delineation and the description of biological processes. Metabolic pathways can be visualized by using PET whose diagnostic properties have been clinically evaluated [30].

Therefore, the registration of functional and structural multi-modality images will increase understanding in cancers. Furthermore, the correlation of histological image information with structural and functional image information from MRI and CT will increase this more and lead to improved radiotherapy target volume delineation.

In this chapter, various modern RT techniques and their applications are introduced in Section 2.2. In order to introduce further image processing algorithms, fundamental definitions in image processing and the DICOM standard are presented in Section 2.3. Scanners such as CT, MRI and PET are the source of medical images and are important for diagnosis, dose planning treatment. Therefore, the commonly used imaging techniques are introduced in Section 2.4. Figure 2.1 shows a typical image registration process, technical details in aspects of transformation, similarity calculation, optimization and assessment are included in a literature review of registration which is presented in Section 2.5. A similar brief review of image segmentation and its classification is introduced in Section 2.6.

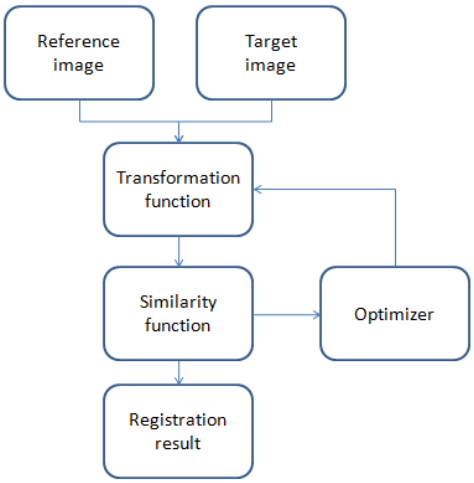

Figure 2.1: A typical flow chart of image registration demonstrating the steps - transformation function, similarity function, and optimization - that are required to obtain a registration result.

2.2 Modern RT technology

RT can be divided into EBRT and brachytherapy based on the position of radiation sources. EBRT is the most commonly used approach of RT, in which the radiation beam is delivered from an external source to patients on a couch. Typically, photons (x-rays or gamma-rays), electrons and other heavier ions (protons or neutrons) can be used as the source of the radiation beam. Among them, x-rays and electron beams are the most widely used sources in EBRT. Clinical x-rays can be generated by decelerating high energy electrons using special metallic targets. Because electrons can be accelerated by a linear accelerator (linac), linacs are capable of generating treatment beams of electrons or photons for EBRT. Figure 2.2 shows the schematic diagram of a typical linac [98]. In addition to linacs, electrons can be accelerated by other accelerators for example microtrons or betatrons and particle beams (protons or neutrons) can be accelerated by specially designed accelerators, which are much more expensive than standard linacs.

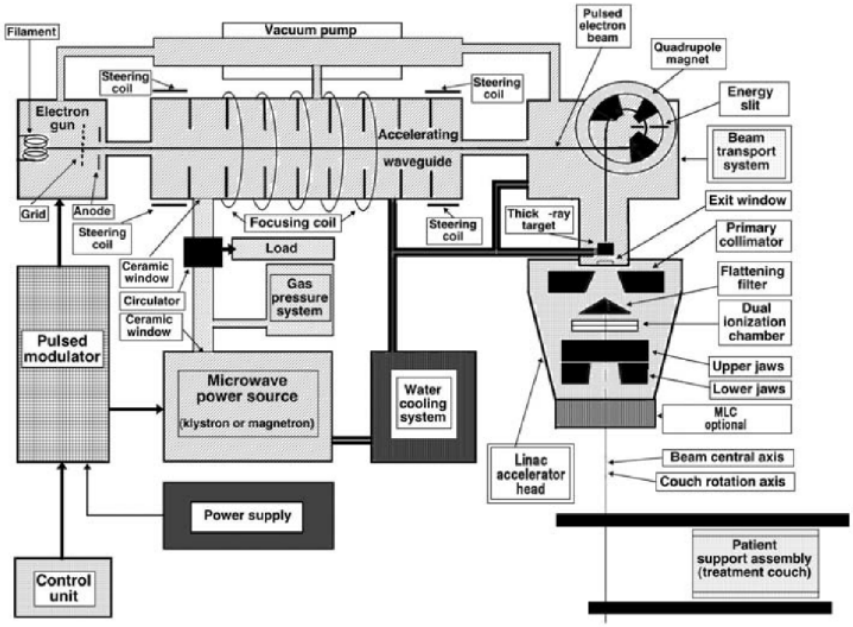

Figure 2.2: The schematic diagram of a typical linac [98].

Linacs accelerate electrons using microwave radio frequency (RF) field in accelerating waveguides, where electrons go through the relatively low potential difference several times. A magnetron or a klystron is usually used to generate the RF power in lower energy linacs or higher energy linacs respectively. Energy of photon or electron beams is commonly measured in terms of kilo electron voltage (keV) or mega electron voltage (MeV). Beams with different levels of energy are usually used in different fields. For example, diagnostic x-rays have the energy from 20 keV to 150 keV and 50-200 keV x-rays can be used to treat superficial tumors. MeV x-rays are usually used to treat deep-seated tumors such as bladder, lung or prostate cancers. Typical modern linacs are capable of providing 4-25 MeV photon beams and electron beams with several levels of energy from 4 MeV to 22 MeV [98].

Because the radiation source is outside of patients, the delivery of the radiation beam to the region of interest is an important issue in external beam RT. In modern RT, several powerful techniques such as stereotactic RT (SRT), image guided RT (IGRT) and intensity modulated RT (IMRT) have been well developed to improve radiation delivery. IGRT delivers radiation to patients under the guidance of information from images such as CT, MRI, CBCT, DRR and EPID. In IGRT, 2D or 3D images are frequently obtained before, during and after a course of treatment. Image processing techniques are also included to process these images and provide accurate guidance for oncologists, physicists and clinicians. As a result, the accuracy of IGRT usually depends on the imaging techniques and image processing algorithms used [44]. For example, registration between CBCT images and planning CT images and matching between EPID images and DRR images can make sure patients are at the correct position during

treatment. IGRT cannot only improve radiation delivery and reduce the geometric uncertainties during treatment, it can also help improve the GTV identification and further treatment assessment. IGRT benefits from many developments in modern imaging techniques (Section 2.3) such as high resolution imaging and four-dimensional (4D) imaging. As IGRT increases the amount of image data acquired for each patient, it helps improve to track of the variation of tumor shape between different fraction of treatment (off-line) or during the time of treatment (on-line). On the other hand, the GTV can vary its shape and position due to movement of patients or respiration. 4D radiation therapy, which combines real-time imaging techniques and adjustment techniques, is designed to overcome this issue in IGRT. Also, multi-modality images can be combined to provide more comprehensive information to assist clinicians in tumor segmentation. As a result, high doses can be delivered to the segmented GTV with small margin of uncertainty and therefore increase tumor control. Furthermore, based on novel registration and segmentation methods, IGRT has the potential ability to achieve semi- or fully-automatic tumor segmentation and radiation delivery [99].

3D conformal radiation therapy (3DCRT) is a widely used RT approach which makes very precise dose planning and reshapes the dose volume to fit the GTV under guidance of planning CT images. IMRT is a development of 3DCRT and is a sophisticated radiation method for accurate radiation delivery. Patients usually have scans with different modalities like MRI or PET in IMRT [135]. As a result, IMRT can provide more accurate treatment planning and can minimize the amount of normal tissue being irradiated. In IMRT, the radiation dose is highly tailored to achieve an optimization in treatment planning system. The modulated intensity of dose can be generated by moving the leaves of a multi leaf colimator (MLC) which consists of 80-120 leaves (typical MLC) and can be moved to block part of the beam as shown in Figure 2.3 [34]. IMRT allows radiation oncologists to vary the intensity very precisely based on the shape of the tumor and therefore limit the side effects. Although IMRT can be treated as the improved technique of 3DCRT and is increasingly used in the treatment of different cancers, 3DCRT is still the main treatment method around the world. The complex treatment planning process of IMRT involves cooperation of medical physicists and dosimetrists and manual segmentation the GTV limits its development. However, novel image processing techniques can assist in this process.

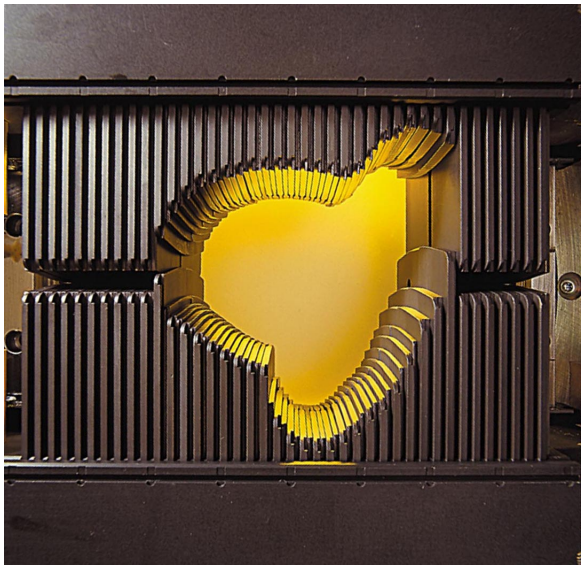

Figure 2.3: Varian's 80-leaf multileaf collimator for shaping a radiation beam [34].

Stereotactic radiotherapy is a novel EBRT technique in which a 3D virtual volume of the tumor region is correlated with the anatomy, the GTV can therefore been irradiated precisely without a surgical incision. It delivers high dose of radiation precisely to a focus or tumor volume under the guidance of multi-modality image information. As a result, stereotactic radiotherapy is usually used for small volume cancers and is usually delivered in fewer fractions than conventional radiotherapy. Due to its high accuracy, immobilization devices and/or movement adjustment techniques are usually used in stereotactic radiotherapy to make sure patients are always in the correct position. In generally stereotactic radiotherapy includes stereotactic radiosurgery (SRS) and stereotactic body radiation therapy (SBRT). SRS refers mainly to the stereotactic treatments of spinal or brain tumors while SBRT focuses on the (chest, lung and pelvis). As a result, it can be used to treat cancers that difficult to treat with surgery or conventional EBRT [9].

In practice, RT is usually applied on patients combining with surgical removal of the tumor. Because of the delay between surgery and RT, the tumor bed or other soft tissues may change positions and/or shapes and therefore affect the accuracy of radiation delivery. To solve this problem, intraoperative radiotherapy is a specially designed technique to apply RT during the process of surgery so that the tumor region is immediately irradiated. On the other hand, complex localization of the GTV can be varied manually during surgery and healthy tissues around the tumor region can be displaced or shielded during the surgery. As a result, a higher dose can be delivered to cancer cells with minimal exposure of the healthy tissues [13].

2.3 Medical image processing fundamentals

In digital imaging, a pixel is a basic element of an 2D image and is the smallest unit that can be varied. In 3D, a pixel turns into a voxel which represents a volume on medical images. Pixel size or voxel size is the physical size that a pixel or voxel represents (usually in mm) on an image. Pixel size is usually related to the resolution and image size in medical image processing. In this thesis, image size is not the physical size of an image, it represents the pixel number of a data set in x, y and z directions. For example, a 512×512 images means the width and height of this 2D image are both 512 pixels. Similarly, a $256 \times 256 \times 47$ image means the width and height of this 3D image are both 256 pixels and it has 47 slices in total.

Spatial resolution is commonly used as a measurement of imaging quality. However, there are various definitions of this concept depending on which field it is being used in. Only the spatial resolution of images is of concern in this thesis. The spatial resolution of an image is most commonly measured by PPI (pixels per inch). For example, an image is 8 inches wide, 6 inches high and has 100 PPI resolution. It means that the image size is 800×600 and 0.48 million pixels are included in this image. If this image is enlarged into 16 inches wide and 12 inches high (twice as big), the image resolution will reduce to 50 PPI. However, the image size of it has not changed and therefore the larger image and the smaller image will look like exactly the same when they are displayed on screen.

Intensity is a basic value given to every pixel in a gray scale image and controls what it looks like when it is displayed on screen. Intensities are usually used to calculate further features of medical images. Dynamic range is the ratio between the largest and smallest possible intensity values on an image. CT data sets have a very high dynamic range which can be re-scaled to a suitable value for image processing algorithms. Medical images can be acquired through different planes in the body such as sagittal plane, coronal plane and transverse plane as shown in Figure 2.4.

Unlike normal images, medical images have not only the image information but also various medical information. This medical information is consistent because it follows the DICOM standard. DICOM information is commonly used to map image data between different coordinates systems (eg. between the patient-based system and image-based system). Important parameters of patients and clinical data can be read from DICOM information directly including:

1. Slice Thickness, is the thickness that one slice can represent. Slice thickness is usually the same for every slice in a data set and is save in terms of mm. It is important in image registration because the slice thickness must be re-sampled to be the same between different data sets before applying any mapping algorithms.

2. Pixel Spacing, is the pixel size of a medical image. It illustrates how large every pixel represents and is saved in terms of mm. Re-sampling slice thickness to be the same with pixel spacing can make the data volume isotropic and is important for 3D image processing

algorithms.

3. Image Position Patient, represents the position of patients. It is usually used as the origin of the patient-based coordinate system.

4. Image Orientation Patient, is the orientation of the patient-based system. Clinical data (eg. tumor contours) need to be transfered to image-based system based on the origin and orientation of patient-based system before being used.

5. Structure Set ROI Sequence, can only be read from a RT structure file. The names of clinical contours are saved in this file (GTV, bladder, prostate, Focal disease etc.).

6. ROI Contour Sequence, can only be read from a RT structure file. The coordinates in patient-based system of clinical contours are save in this location.

7. Registration Sequence, can only be read from the RT registration file. It represents the manual registration parameters between two different reference coordinate systems (RCS). The gold standard parameters of the registration between two different data sets (such as CT and CBCT) can be calculated from it.

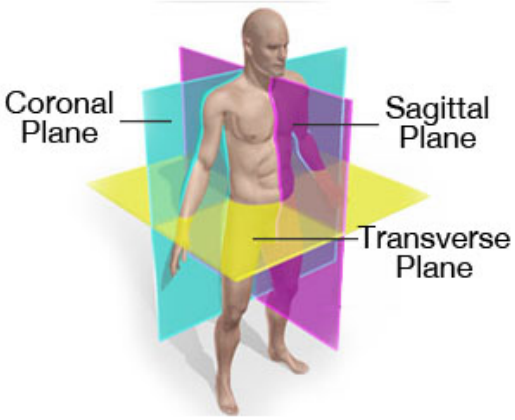

Figure 2.4: Anatomical planes of human body. Sagittal plane: plane that runs down through the body, dividing the body into left and right portions. Coronal plane: plane that runs perpendicular to the sagittal plane and divides the body into anterior and posterior (front and back) portions. Transverse plane: horizontal plane that divides the body into upper and lower portions [39].

2.4 Imaging techniques used in RT

2.4.1 CT

The term CT is mostly used to refer to X-ray CT which uses x-rays processed by computer to generate tomographic images. It provides a view inside an object without cutting it open by giving different image intensities to different parts inside the object based on their ability to attenuate the X-ray beam. Generally, the highest intensity on CT image is 3071 and the lowest

is -1024 on the Hounsfield scale. Intensity for other materials can be calculated using Equation 2.1 based on their average attenuation coefficient μ_X. The intensities of some typical materials are shown in Figure 2.5, water is defined to have an intensity of 0, while air is -1000, lung is -500, bone is 400, cranial bone can reach 2000 or more.

$$H = \frac{\mu_X - \mu_{water}}{\mu_{water}} \times 1000 \tag{2.1}$$

Usage of CT has increased dramatically over the last 20 years, about 72 million CT images were taken in the USA in 2007 [52]. CT images are widely used in diagnosis, dose planning (Figure 2.6) and assessing the response of the GTV to radiation.

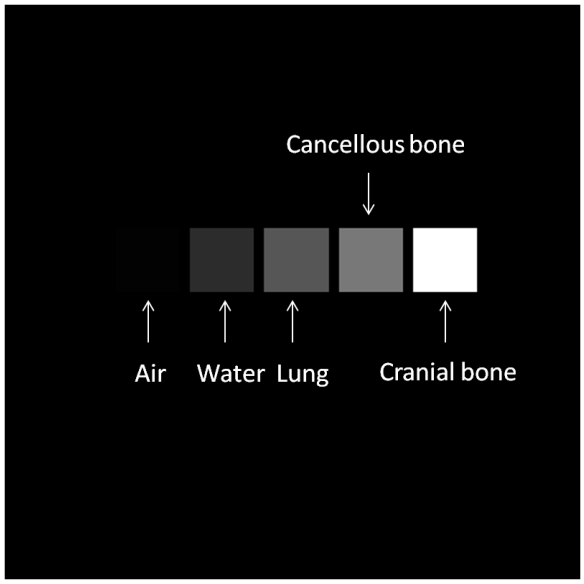

Figure 2.5: Different intensities of some typical materials on CT image: water is 0, air is -1000, lung is -500, cancellous bone is 400, cranial bone can reach 2000 or more.

As shown in Figure 2.6, in a conventional CT imaging system, patients lie on a couch which can move through a circular opening. An x-ray source rotates around the patient and sends a narrowly collimated beam of x-rays through the patient. Typically, the width of this fan-shaped beam can be set to be 1-10 mm and it forms the slice thickness of CT slices after computation. Detectors installed on the opposite side of the patient detect the x-rays exiting from the patient and pass these data to computers where they are reconstructed into CT slices. CT slices can be easily reconstructed into DRR images which are commonly used to verify the position of patients in RT (Figure 2.6).

On the other hand, the shape of the scan beams can be varied and therefore generate different types of images. CBCT is a 3D imaging technique in which cone-shaped x-ray beams are used. CBCT was firstly used in 1990s and it has been widely used in dentistry, interventional radiology (IR) and IGRT now. CBCT scanners generate 3D image data by rotating around the

regions of interest and taking a series of distinct images which will be reconstructed into a 3D volume. CBCT is also widely used to verify the position of patients in IGRT. However, soft tissue imaging quality is limitation of CBCT. Compared with conventional CT images, CBCT images usually have much poorer quality with more noise and motion artifacts which may be induced during the acquisition process [30].

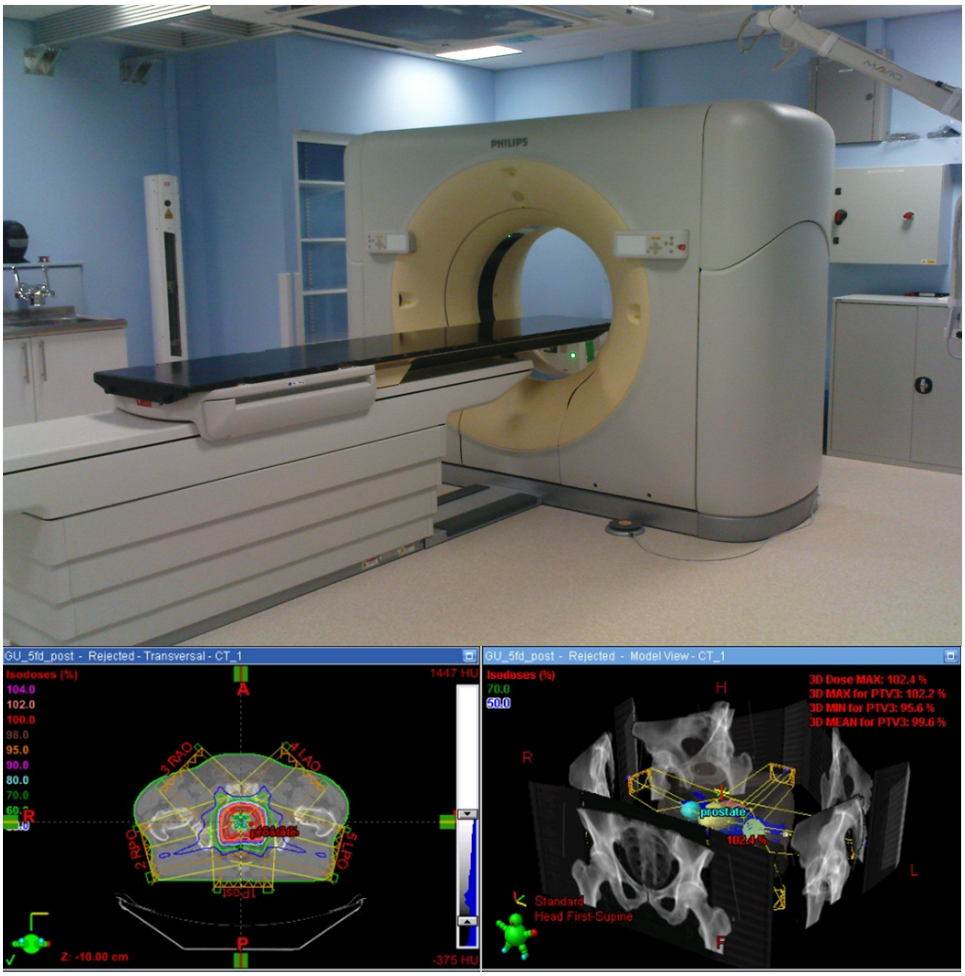

Figure 2.6: The Philips Brilliance 85 cm big bore 16-slice CT imaging device with flat couch and external lasers (top), CT image with 5 field prostate IMRT treatment information and dose distribution (left bottom), DRR images (bones) with dose information of prostate area, the orientation and the position information of the patient in treatment planning system (right bottom) [12].

There are a lot of advantages of using CT in RT. Firstly, CT can provide accurate identification of structures with negligible distortion and can eliminate the superimposition of images. Secondly, the improved resolution of CT can distinguish the differences between tissues that have less than 1% differences in physical density. Thirdly, the geometric consistency of CT images allows 3D images to be constructed. Fourthly, CT data can be viewed in transverse, coronal, or sagittal planes, depending on different purposes (Figure 2.4) [21]. The disadvantages (adverse

effects) of CT imaging techniques have been increasingly noticed during recent years. Normal healthy cells can be damaged in CT scanning because x-rays are used in this scan and therefore deliver a radiation dose to patients.

2.4.2 MRI

MRI is also a widely used imaging technique in RT and it can be applied in diagnosis, follow-up assessment and disease staging. By 2013, there were over twenty-five thousand MRI scanners in use around the world [3]. Generally, MRI is considered to be safer than CT so that it is recommended in preference to CT when the same information can be extracted from either of them. A typical MRI scanner is shown in Figure 2.7.

Figure 2.7: The GE Signa HDxt 3.0T MRI scanner which can deliver comprehensive and advanced 3.0T whole-body imaging for the full range of clinical applications. It has great tissue characterization and artifact reduction [126].

There are three different magnetic fields in a typical MRI scanner: the main magnetic field, the gradient magnetic field and the oscillating magnetic field. The hydrogen nuclei (proton) in water molecules, which make up approximately 70% of human body, can be treated as spinning balls with charges. As a result, under the main static magnetic field, they will precess around the axis of this field. As the protons have two possible precession directions, they distribute in either low-energy state or high-energy state. In a macroscopic view, their transverse magnetization component is zero since they have different rotation phases and offset each other. They have a longitudinal magnetization component because protons in low-energy state are a little more than protons in high-energy state in an equilibrium state. In addition, an oscillating magnetic

field (RF pulse) is applied to patients with fixed frequency (equal to the precession frequency). This RF pulse generates two results: 1. Protons in low-energy state can absorb energy from it and jump to the high-energy state, which makes the longitudinal magnetization component fade away when the numbers of protons in different energy states reach the same. 2. Protons are forced to have the same phase and therefore generate transverse magnetization component. Since this RF pulse rotates the magnetization component by 90°, it is commonly named as 90° RF pulse. The transverse magnetization component generated by the 90° RF pulse can be detected by the receiver coils and show the density difference of protons. Also, gradient magnetic field is used to vary the main magnetic field (therefore vary the precession frequency) along different directions and record the position information. However, it is not enough just to find the difference between proton density in clinical. After removing the oscillating magnetic field, protons return to the equilibrium state and start to recover the original magnetization vector (relaxation). There are two different types of relaxation time: spin-lattice (T1) and spin-spin (T2). T1 is the relaxation time between removing the RF pulse and the completely recovery of the longitudinal magnetization component, it is also known as longitudinal relaxation. T2 is the relaxation time between removing the RF pulse and the completely disappear of the transverse magnetization component, it is also called transverse relaxation. Because different parts of human body have different T1 and T2, contrast of MRI images can be weighted by either of them to generate T1 or T2 weighted MRI images. On the other hand, the time between sending the RF pulse and the signal collection is defined as echo time (TE) while the time between sending two RF pulses is defined as repetition time (TR). Because T2 is usually much smaller than T1, large TR can ensure sufficient longitudinal relaxation and therefore clear the T1 difference between different tissues. Similarly, small TE can make sure signal is collected before transverse relaxation finished and therefore clear the T2 difference between different tissues. As a result, large TR and TE are commonly used to highlight the T2 difference (T2 weighted) and small TR and TE are used to highlight the T1 difference (T1 weighted). While T1-weighted MRI images is mainly used for identification of cerebral cortex, fatty tissue and focal liver lesions, T2-weighted MRI images focuses on detecting edema, white matter lesions and anatomy in the prostate and uterus [125].

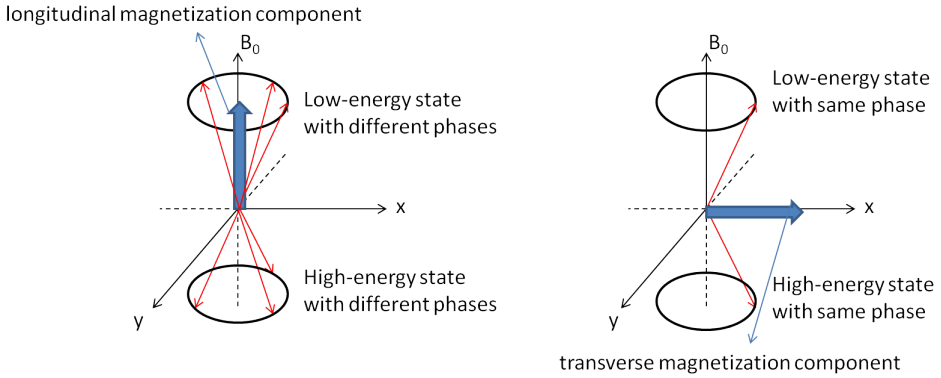

Figure 2.8: The precession and magnetization of protons under main static field B_0 (left). The variation of magnetization orientation after 90° RF pulse (right).

CT and MRI are complementary imaging approaches, the combination of them can provide more comprehensive information for cancer diagnosis and the GTV identification [19]. However, to achieve this, non-rigid registration method must be used to find the distortions between them. Compared to CT, the biggest advantage of MRI is that no radiation dose is delivered to patients. As a result, MRI is more recommended when either of them can provide the same information. Practically, MRI and CT both have their own advantages and disadvantages for different applications. For example, MRI provides much more specific information on bones than CT and has excellent resolving ability for soft tissues. MRI is more flexible by using different weights for different diseases. However, CT works better on prostate, lung and liver. Also, acquisition of CT is usually much cheaper and faster and than MRI. Unlike CT, MRI can provide both structural and functional information. Functional MRI is designed particularly for brain. Increasing neural activities in brain will increase the demand of oxygen, which will lead to overcompensation of oxygenated hemoglobin. Magnetic resonance signal will increase due to this effect because signals are attenuated by less deoxygenated hemoglobin [121].

MRI-guided RT has been the research hotspot in recent years and it can be achieved by combining MRI scanner with linac. Compared with CBCT-guided RT, MRI/linac can provide images at time-of-treatment, which have all of the benefits of MRI such as excellent soft-tissue based images and robust functional images [68]. The main obstacle to the realization of MRI/linac is that the strong magnetic field required by the MRI scanner may affect the function and normal operation of the linac. This problem has been overcome and the first clinical MRI/linac system was built in 2014 at the University Medical Center Utrecht [26].

Comparing with CT/PET, MRI/PET is a technique combing MRI and PET which can provide naturally registered MRI and PET images. An MRI/PET system can provide more robust and comprehensive comparison between the information obtained in molecular and metabolic aspects. The main difficulty limiting the application of MRI/PET is that how to decrease the interference of the strong magnetic field with the detection of PET signal [110].

2.4.3 PET

PET also uses a computed tomography technique which can provide functional information of patients in RT. Compared with other imaging techniques, PET images provide very useful and accurate functional information but with poor resolution and high cost. In practice, PET is usually taken together with CT by a PET-CT machine so that they are naturally registered (rigid). Compared with MRI, PET can detect molecular biology detail in the regions of interest and is more useful to be combined with structural images.

Radioactive isotopes are used in PET imaging technique to generate positron emission. Annihilation occurs and generates a pair of photons (gamma-rays) in approximately opposite directions when a positron encounters electrons. Light-sensitive devices (photomultiplier tubes or silicon avalanche photodiodes) are designed to detect the light which is triggered by these photons in a scintillator. Only coincident detections of a pair of photons are considered to be validate. PET images are computed and reconstructed based on these coincidences by computers. [11]. Generally, the radioactive isotopes (tracers) are injected in the body of patients incorporated with biologically active molecules. Currently, the most commonly used biologically active molecule is FDG which can be used to detect tissue metabolic activity. Figure 2.9 shows a GE PET-CT 560 scanner.

Figure 2.9: The GE Optima PET/CT 560 scanner which can provide a complete head-to-toe study of patients. It can generate registered PET/CT images and can be used as a standalone 8- or 16-slice CT scanner as well [12].

PET is widely used in RT of lung cancer, neuroimaging and small animal imaging. Both 2D

and 3D images can be reconstructed based on different locations of detectors and reconstruction techniques. On the other hand, PET imaging delivers minimization of radiation dose to patients because short-lived isotopes are used. It can be used for diagnosis, cancer staging and assessment of the response to RT or other treatments. However, acquisition of PET images is usually expensive and complex which limits its application. The reason for this is that the radioactive isotopes must be generated by high-cost cyclotrons a short time before being used and biologically active molecule must be combined with the radioactive isotopes very quickly due to its short life time.

2.5 Image registration

Image registration methods have been used widely in human medicine for atlas building [32], anatomy segmentation [23], RT [70], image-guided surgery [85], computational model building [41] and contrast-enhanced imaging [81]. Preclinical studies have utilized a multitude of applications involved with image registration including registration approaches for atlas based segmentation [58, 83], 3D reconstruction [56], high-resolution imaging [40], algorithms focusing on 3D distance transform [128], affine transform [136], point-based fusion [133], and multi-modality registrations for PET-MRI [50], SPECT-CT [107], and PET-CT [130]. Over the past 25 years, image registration has grown into a distinct field with several independent software programs, such as insight segmentation and registration toolkit (ITK) [57], 3D slicer [36], flexible linear image registration toolkit (FLIRT) [54] and flexible algorithms for image registration (FAIR) [89] now available.

In general, an image registration algorithm can be divided into four parts: image conditioning, geometric transformation, similarity function and optimization (Figure 2.1). Any step that alters the original data to make it more suitable for applying image registration is known as image conditioning. Examples of image conditioning include de-noising, re-sampling, down-sampling and pre-segmentation.

2.5.1 Transformation

As it is common for the patient orientation and immobilization to vary between imaging studies, the first and key component of registration is the transformation. This describes the geometrical shift that is required to be applied on the target image to match it to the reference image. The complexity of the transform can have a decisive effect on the computation cost and is chosen based on the spatial variation of test data, computing power and accuracy required. Rigid transformation methods are the most commonly used methods and are usually applied between images that have no distortion (such as CT to CT). Generally, a rigid geometric transformation can be achieved by translation and rotation; for example, a 3D rigid transformation can be defined by six parameters: three for translation (T_x, T_y, T_z) and three for rotation (α, β, γ).

Rigid registration is commonly used to match between bones on medical images, such as the skull [7, 77]. An affine transform is a general linear rigid transformation that allows for rotations, translations, scaling and shearing in order to preserve collinearity [62]. The DICOM standards support various transformation models to specify spatial relationships between two imaging studies and in general commercial RT planning systems can support image registration using affine transformations and some non-rigid methods [1, 62]. Rigid registration can also be applied before a non-rigid registration as an image conditioning step [51, 84].

The assumption that rigid movement of anatomy occurs globally is incorrect in any number of situations, therefore limiting the widespread use of rigid registrations for sites other than the head [62]. Most non-rigid registration methods are based on deformable models. Deformable transformation models range in complexity and may be very simple with relatively few parameters or more complicated as in the case of local models in which each independent point or voxel moves independently [62]. There are two directions in deformable registration: free form (non-parametric) deformable registration (FFD) and guided deformable registration, which are controlled by models based on prior knowledge of the registered objects or organs. The fundamental difference between them is that the FFD allows any deformations by moving the positions of its control grid. Control points in the grid are moved individually and the coordinates of the control points are treated as variables in an optimization algorithm. The most commonly used guided deformable registration methods are elastic-based and flow-based. Elastic-based methods treat organs as elastic solids and define two forces: internal forces that oppose the deformation and external forces that try to deform the images. The best transform can be obtained by finding equilibrium between both internal and external forces. Flow-based methods include fluid flow and optical flow. These methods treat the registration problem as a motion problem and therefore the best match is achieved by minimizing the energy term in a physical model. A popular FFD approach is based on the interpolation provided by the cubic B-spline method [106]. Figure 2.10 illustrates a B-spline control grid on the reference and target image of a dog with a sinonasal tumor. The registration algorithm based on B-spline treats the deformation of an image as a combination of several basic functions that can be adjusted as required [33]. In this situation, the issue becomes how to determine appropriate coefficients of the basis functions in order to optimize the similarity function. A similar method called thin-plate spline (TPS) can also generate the interpolation of a global FFD registration using a set of corresponding control points identified on both image datasets, however a major drawback is that any single control point will affect the entire deformation [87]. As a result of the various advantages and limitations that exist between deformation models, a great deal of research is focused on defining a global transformation by several local transformations [95].

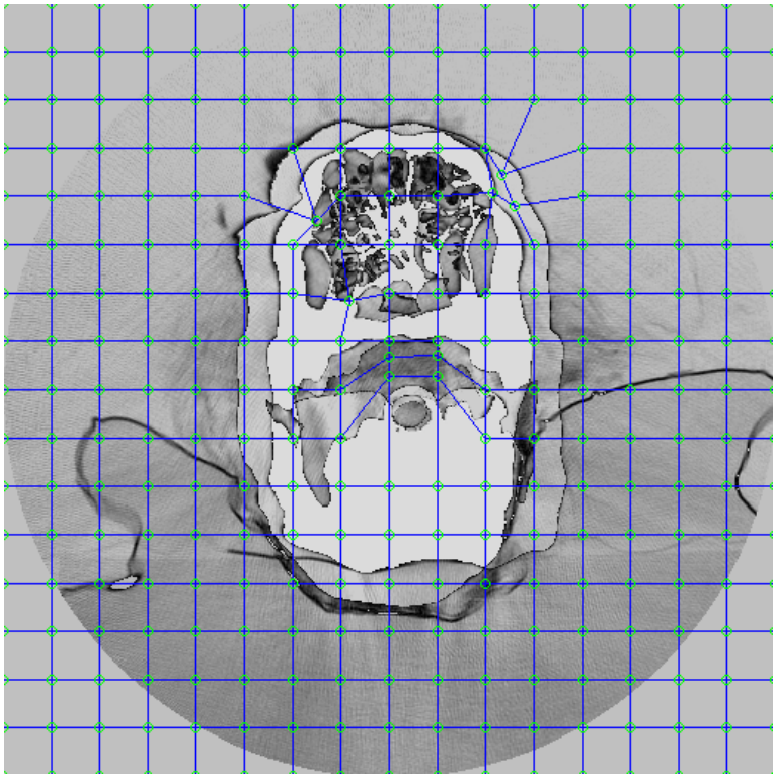

Figure 2.10: An example of a B-spline control grid on the reference and target image of a dog with a nasal carcinoma. This demonstrates a 20×20 control grid on the pre-treatment and post-treatment CT image(512×512) images (manually warped).

2.5.2 Similarity Function

The parameters of a transformation that bring the image datasets into alignment are assessed by measuring the similarity between the image sets [62]. Generally, there are two kinds of similarity measurements: intensity-based and feature-based measurements. The most popular intensity-based similarity function is based on intensity difference or intensity correlation. Sum of the squared distance (SSD) is the common measurement in clinical use that is based on the intensity difference. The basic assumption of this approach is that corresponding pixels in two images have identical intensities. SSD may be applied in cases with little noise as the intensities will not be substantially different between images, or in cases with simple backgrounds as pixels in the background will not heavily affect the calculation [10]. A more complex intensity correlation based measurement is typically used for medical images that have a complex environment (intensities on different images are considerably different and noise significantly affects the calculation). Correlation ratio, correlation coefficient, entropy and mutual information (MI) are commonly used similarity calculation methods. In particular, MI, normalized MI and MI based on different types of entropy calculations have proven to be very powerful, sensitive and efficient on a wide variety of image registration situations [62, 118, 124]. MI is an accurate way to measure the relevance between two variables where

the intensities of corresponding pixels on the reference and target image are treated as variables. MI utilizes the basic assumption that the intensity between corresponding pixels has the same transform function, therefore is robust when there is missing or limited data (for example, a clearly defined intracranial tumor on MRI images but indistinct on CT images) [62]. MI can also be used to measure other image variables such as the gradient of intensities [20].

The success of feature-based similarity functions depends on the feature structure extracted, such as anatomic (bones) or artificial landmarks (fiducials). Texture, scale invariant methods, methods based on the organ boundaries or internal landmarks can all be used in this context. Most feature-based algorithms use points, lines, or surfaces for matching [62, 63, 94]. A minimum of three or four pairs of points are required in order to compute the rotations and translations for a rigid or affine transformation. Unlike point matching, line and surface matching do not require a one-to-one match between images but rather attempt to maximize the overlap between equivalent lines and surfaces such as the skull surface, ribs or pelvis [62, 63, 94]. In general, SSD, MI and other similarity measurements can be used to measure the similarity between features just as in intensity based cases. Euler distance, which can be treated as the square root of SSD in different dimensions, measures the distance between feature points or their descriptors while MI is usually used to measure the similarity between feature regions [35, 137].

The similarity function used for rigid registration, which only considers one term such as MI, is simpler than in non-rigid registration. At least two terms must be used in non-rigid registration: similarity terms and penalty terms. The latter can be used as a constraint or regularization term which is a relative term to the distortion field that contains information on the spatial variation caused by distortions [80]. Regularization thus discourages illogical or random deformations from affecting the registration process [62]. The most commonly used penalty term is the second order derivative of the transformation function, which relates to the bending energy of the transformation [114]. Figure 2.11 illustrates the transformation process and the corresponding similarity calculation used in the registration of images from a dog with a nasal tumor.

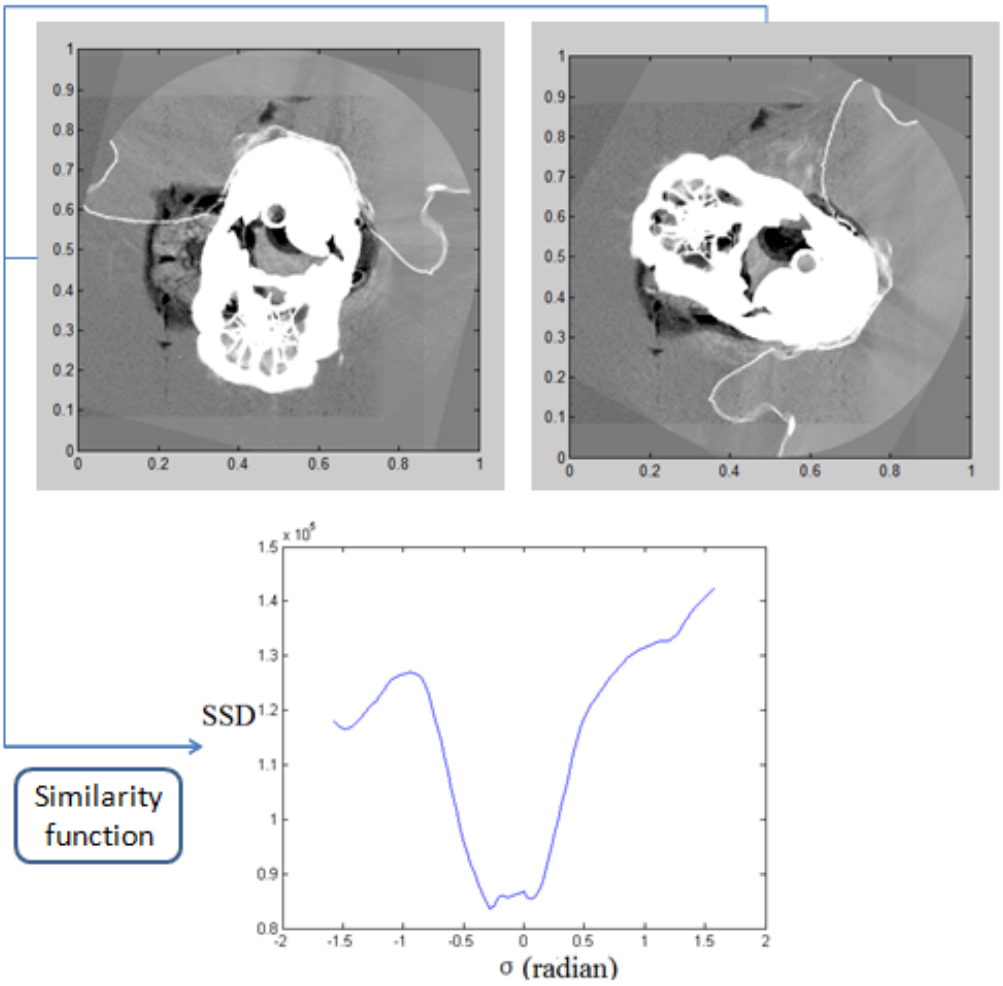

Figure 2.11: The variability in the similarity function (SSD) is shown and demonstrated in a canine nasal tumor images. The transformation function (rotation) is applied on the target image rotating it around the reference image from -90° to $+90^{\circ}$.

2.5.3 Optimization

Optimization is a strategy used to search the extremes of the space generated by the similarity function. It is crucial to a registration method as most similarity functions can have several local extremes, which will trap the search and give sub-optimal results. Several optimization algorithms have been applied in the field of medical image registration in an attempt to solve this efficiently. The most commonly used algorithms include gradient descent [104], quasi-Newton [84] methods such as L-BFGS, and stochastic algorithms [92] such as simulated annealing. An excellent comparison of eight commonly used optimization algorithms based on B-spline and MI techniques for non-rigid medical image registration methods was reported in 2007 [65].

2.5.4 Assessment

The obvious motivation for registering images from different studies is to map clinically useful information from one study onto another, for example in treatment planning prior to radiation delivery. If data can be successfully fused, radiation oncologists can then map tumor volumes such as the GTV, CTV and PTV or OAR directly onto the CT images needed for dose calculations (structure mapping) [62]. Therefore, relying on the ability of a software system to adequately register images is of utmost importance in order to adhere to current radiation guidelines — namely to appropriately outline tumor volumes to limit normal tissue toxicity. Also, it is important to realize the difficulties in accurately validating the performance of a complex registration method. In some cases, a registration algorithm can be assessed using phantom data, but this is not commonly done as performance on phantoms cannot ensure comparable performance on clinical cases [119]. Another commonly used approach is to use synthetic images on which manual definition of corresponding points such as fiducial markers can provide a straightforward assessment of a registration method [79, 109]. The Dice coefficient, which measures the overlap between clinical and registered contours, puts a numerical value on the registration accuracy [5, 123]. Within the range 0% to 100%, a Dice value of 100% indicates excellent geometric agreement while a Dice value of 0% represents poor geometric agreement. The Jaccard index and Tanimoto coefficient (both vary from 0% to 100%) which can be calculated directly from Dice are also used to measure the similarity between regions. However, they need prior knowledge (contours of the same region) on both the reference and target image.

2.5.5 Classification of registration algorithms

The basic approaches used for image registration are shown in Table 2.1.

Criteria	Classification
1. Dimensionality	a. Spatial dimensions only 2D - 2D; 2D - 3D; 3D - 3D. b. Time series (more than two images), with spatial dimensions 2D - 2D; 2D - 3D; 3D - 3D.
2. Nature of registration basis	a. Extrinsic 1. Invasive 2. Non-invasive b. Intrinsic 1. Landmark based 2. Segmentation based 3. Voxel property based c. Non-image based (calibrated coordinate systems)
3. Nature of transformation	a. Rigid; b. Affine c. Projective; d. Curved
4. Domain of transformation	a. Local; b. Global
5. Interaction	a. Interactive; b. Semi-automatic; c. Automatic
6. Optimization procedure	a. Parameters computed; b. Parameters searched
7. Modalities involved	a. Monomodal 1. Auto-radiographic; 2. CT or CTA; 3. MRI; 4. PET; 5. Portal; 6. SPECT; 7. US; 8. Video; 9. X-ray or DSA b. Multimodal 1. CT-MRI; 2. CT-PET; 3. CT-SPECT; 4. DSA-MRI; 5. PET-MRI; 6. PET-US; 7. SPECT-MRI; 8. SPECT-US; 9. TMSa-MRI; 10. US-CT; 12. X-ray-CT; 13. X-ray-MRI; 14. X-ray-portal 15. X-ray-US; 16. Video-CT; 17. Video-MRI c. Modality to model 1. CT; 2. MRI; 3. SPECT; 4. X-ray d. Patient to modality 1. CT; 2. MRI; 3. PET; 4. Portal; 5. X-ray
8. Subject	a. Intrasubject; b. Intersubject; c. Atlas
9. Object	a. Head; b. Thorax; c. Abdomen d. Pelvis and perineum; e. Limbs; f. Spine and vertebrae

Table 2.1: The classification of registration methods by Maintz and Viergever in 1998 [80].

2.6 A brief overview of medical image segmentation

Image segmentation is defined as the process of identifying regions with similar properties and their boundaries on images [129]. Properties such as intensity, gradient and texture can be used as the measurement to distinguish between regions on different imaging modalities [100]. In the medical field, image segmentation has played an important role in RT planning by assisting in the identification of anatomical structures or soft tissues [46]. Table 2.2 summarizes the commonly used segmentation techniques and their classification criteria used in the field.

Since different imaging modalities for different parts of human body have different properties, it is difficult to find a generally applicable segmentation technique [112]. Specifically, the simplest segmentation method is thresholding in which different regions are segmented using intensity information. However, setting the correct threshold is difficult and artifacts or noise will affect the performance [101]. Another commonly used method is region growing in which the initial 'seed' must be planted. Pixels connected to the 'seed' are extracted and 'grow' until meeting a stopping criteria. Edge detection methods, for example the Hough transform, are usually combined with this method to provide the stopping criteria. This method is also sensitive to noise and may required manual intervention to set the position of the initial 'seed'. In addition, because of the intensity inhomogeneity of medical images, they are affected by the weak boundaries [113]. As a result, region growing is usually only used to detect simple and small structures [59]. Instead of using intensity information from the histogram, texture-based techniques, which extract information on image texture, are used to characterize distinct image regions. There are many different methods used to extract texture features, such as co-occurrence [8], Fourier [28] and fractal methods [22]. Textures are also commonly used to generate a feature space which can be classified by classifiers such as k-nearest-neighbor classifier [127], Bayes classifier [122], support vector machine (SVM) [103] and artificial neural network (ANN) [117]. The disadvantage of feature-based methods is that the correct texture class must be defined from various training textures prior to the segmentation. Shape modeling is another statistical segmentation method which finds a probabilistic representation of the target structure. It requires registered training data to build a model. Active shape models are a special model-based method that uses continuous lines to represent the target contour. It can be divided into parametric active contour model such as Snake model [60] and geometric active contour model such as level set method [82]. These methods are very robust and can evolve the active contour based on preset criteria to find the target boundaries. A level set method can find the topology changes automatically. However, careful initialization and parameter setting limit its applications. Atlas-based method is also a commonly used and powerful approach for medical image segmentation. It provides a convenient way to identify organs or tissues based on differences in their anatomy, volume, shape, and biological features. However, it requires a lot of effort to build the atlas and its performance is highly related to the registration method used [25].

Criteria	Classification
1. Dimensionality	2D; 3D.
2. Nature of segmentation basis	a. Intensity; 1. Histogram; 2. Gray level. b. Texture; c. Color; c. Brightness.
3. Application	a. Diagnosis; b. Volume calculation; c. Identification of anatomical structures; d. Treatment planning; e. Image-guided surgery.
4. Interaction	a. Interactive; b. Semi-automatic; c. Automatic.
5. Modalities involved	a. CT or CTA; b. MRI; c. PET; d. Portal; e. SPECT; f. US; g. Video; h. X-ray or DSA.
6. Techniques	a. Thresholding; b. Region growing; c. Edge-based; d. Texture-based; e. Classifier-based; f. Model-based; g. Atlas-based.

Table 2.2: The classification of segmentation methods.

2.7 Conclusion

In this chapter, fundamental backgrounds in medical image processing and RT technologies were introduced. Also, commonly used image registration and segmentation techniques were reviewed and summarized.

Medical scans such as CT, MRI and PET are powerful methods to provide different kinds of information about the patient as well as the disease. However, making them more accurate, efficient and comprehensive automatically to improve the clinical protocol is difficult. As a result, lots of image processing techniques in the medical field were developed. Based on them, the work of this thesis was done focusing on image registration and segmentation which are the two most important branches of medical image processing. Technical details of them are introduced in the next chapter.

Chapter 3

Algorithms

3.1 Introduction

Image processing is a complex field that includes a great deal of sophisticated algorithms. In the RT process, registration provides a map between two image data sets and makes it available to use the information from the reference image on the target image. This is necessary to decide how much and what kind of information is used to generate the GTV. A significant amount of effort has gone into developing a general suitable registration method which can be used to register images from different modalities. Also, as mentioned in Chapter 2, the efficiency of the registration algorithm is important if it is to be used within the RT workflow and help clinicians. However, there is a trade-off between the registration accuracy and time cost.

Image segmentation is the process of partitioning an image into several segments. Segmentation algorithms are usually applied after registration and use the registered information as a prior for more accurate segmentation. There are many segmentation methods available for medical imaging such as methods based on thresholding, clustering, histogram, edge detection, shape model and region-growing. Although they all have their own advantages, it is important to choose a method which can use all the information from registration and combine specific knowledge from the image.

In this chapter, image conditioning methods which are important in making images suitable for further processing such as down-sampling, re-sampling, de-noising and pre-segmentation are introduced in Section 3.2. In Section 3.3, a rigid registration algorithm combining SIFT as a feature extraction method and MI as the similarity measurement is presented. A non-rigid registration method which is suitable for registering images with distortions is introduced in Section 3.4. This method used cubic B-spline as a interpolation method to generate smooth distortion. Control grids were treated as variables to generate a similarity function and were optimized by a L-BFGS method. A Gabor filter was also used in this method to extract the features required in the similarity function. A follow up segmentation algorithm based on a level set method is introduced in Section 3.5 which is applied after the registration algorithms. This method is robust and can change the topology of evolving contour automatically. In Section 3.6, the Dice coefficient which is used to measure the similarity between two contours

in this thesis is introduced.

3.2 Image conditioning

3.2.1 Re-sampling and down-sampling

Images from different modalities of the same patient usually have different thickness, dynamic range and volume size. For example, the CT data set of a test patient has 39 slices with 512×512 pixels in every slice while the corresponding MRI data set has 26 slices with 256×256 pixels in every slice. Therefore, before applying any image processing algorithm, re-sampling the test data into the same size is necessary. Down-sampling is the process of rescaling an image into a smaller size (usually the down-sampling rate is 4 in this thesis). This can save computational power and therefore make the algorithms more efficient. However, both re-sampling and down-sampling may generate non-integer coordinates. In this work, bilinear interpolation was used to provide smooth intensity values. A 2D example is shown in Figure 3.1 where the intensity of point P can be calculated as Equation 3.1.

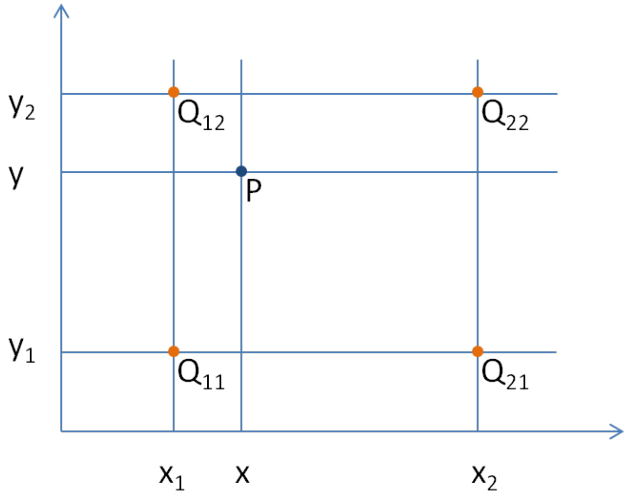

Figure 3.1: The general view of bilinear interpolation of a 2D example with P the target point.

$$G(P) = \frac{G(Q_{11})(x_2-x)(y_2-y)}{(x_2-x_1)(y_2-y_1)} + \frac{G(Q_{21})(x-x_1)(y_2-y)}{(x_2-x_1)(y_2-y_1)} + \frac{G(Q_{12})(x_2-x)(y-y_1)}{(x_2-x_1)(y_2-y_1)} + \frac{G(Q_{22})(x-x_1)(y-y_1)}{(x_2-x_1)(y_2-y_1)} \tag{3.1}$$

where G is the intensity of certain point on the image.

3.2.2 Re-sampling of contours

Unlike re-sampling of images which consists of pixels with different intensities, re-sampling of contours is more complicated. Intensities of pixels at any desired positions can be generated by appropriate interpolation methods and therefore an image can be resized or re-sampled with any wanted parameters. Resizing contours can be achieved simply by resizing the distances between contour points and the center of the image. How to decide whether a pixel is a contour point or not on the re-sampled image is however the main issue of contour re-sampling. Here, contours obtained from clinicians were firstly reconstructed into a 3D volume by using Delaunay triangulation. The intersection points between the contour volume and the re-sampled images were then calculated to generate the re-sampled contours.

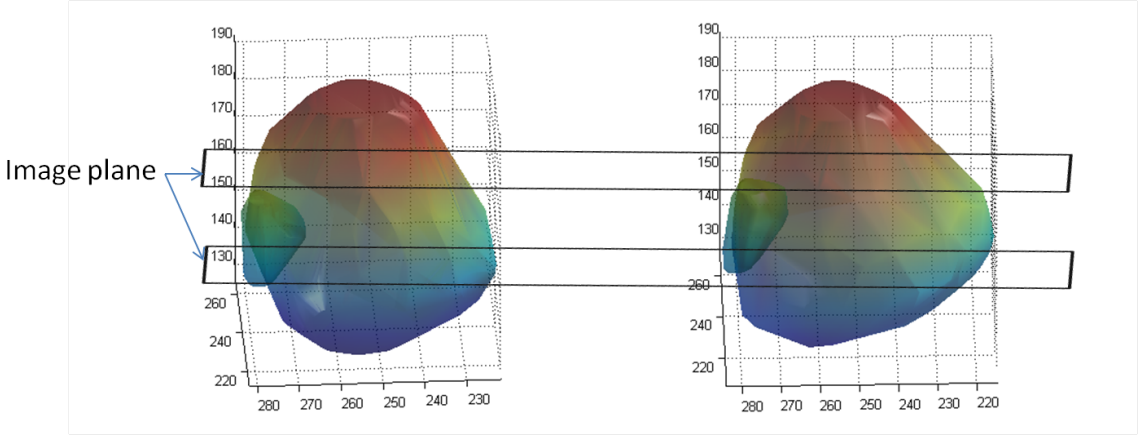

Figure 3.2: The re-sampling process of contours on medical images. 3D reconstruction shape of the clinical prostate contours on diagnostic MRI images is shown on the left (the large volume) together with the focal region (small volume) and re-sampled images (black). 3D reconstruction shape of the clinical prostate contours on the corresponding planning CT image(large volume) and the non-rigid registered focal region (small volume) are shown on the right.

2D Delaunay triangulation for a set of points P is a set of triangles $DeT(P)$ where no point in P is inside the circumcircle of any triangle in DeT. Specifically, the re-sampling of a set of 3D contour points P can be achieved by the following process:

1. Select any 3 points in P as the initial triangle.
2. Find the closet point to the initial triangle by minimizing the sum of distance to the 3 initial points.
3. Judge whether there is any point in P inside of the circumscribed sphere of the selected 4 points by calculating the distance from points in P to the center of this tetrahedron. If not, this is a Delaunay tetrahedron and use every triangle in this tetrahedron in step 2. If there is, this is not a Delaunay tetrahedron, use the second closet point until finding the Delaunay tetrahedron.
4. After including all the points in P in Delaunay tetrahedrons, remove the triangles inside of

the convex hull of P (calculated by the convex hull function in MATLAB).
5. Calculate the intersection points of remaining triangles and the re-sampled images as shown in Figure 3.2.

3.2.3 De-noising

Noise is the unwanted information that is present in the imaged object. It can be random or white noise with no coherence, or coherent noise introduced by the mechanism of devices or processing algorithms. De-noising of images here is the process of removing the noise from the original images. As medical images are acquired using electronic recording scanners, the main noise in them is caused by random electrons. In addition, raw medical image data is mapped to a matrix of gray values (intensities), therefore, noise on them involves intensity changes through mapping.

There are many types of noise and various de-noising algorithms. Two typical noises are salt and pepper noise (Figure 3.3) and Gaussian noise (Figure 3.4). In salt and pepper noise, the noisy pixels are very different from their neighboring pixels and can be easily observed by eyes. This kind of noise is unrelated to the original image information and can be treated as adding impulsive noise on the randomly generated positions. Its probability density function is defined by Equation 3.2. Gaussian noise changes image intensities very little from their original values compared with salt and pepper noise. The histogram of the noise shows a normal distribution while other distributions are also possible. However, because of central limit theorem, the sum of different noises tends to be Gaussian noise and therefore it becomes a good model for de-noising algorithms.

$$I = \begin{cases} Pe & \text{Po} \\ 0 & \text{1-Po} \end{cases} \tag{3.2}$$

where Pe is the intensity value of the impulsive noise (usually large e.g. 1000 in Figure 3.3) and Po is the probability of every pixel in an image being a noisy pixel (e.g. 0.05 in Figure 3.3).

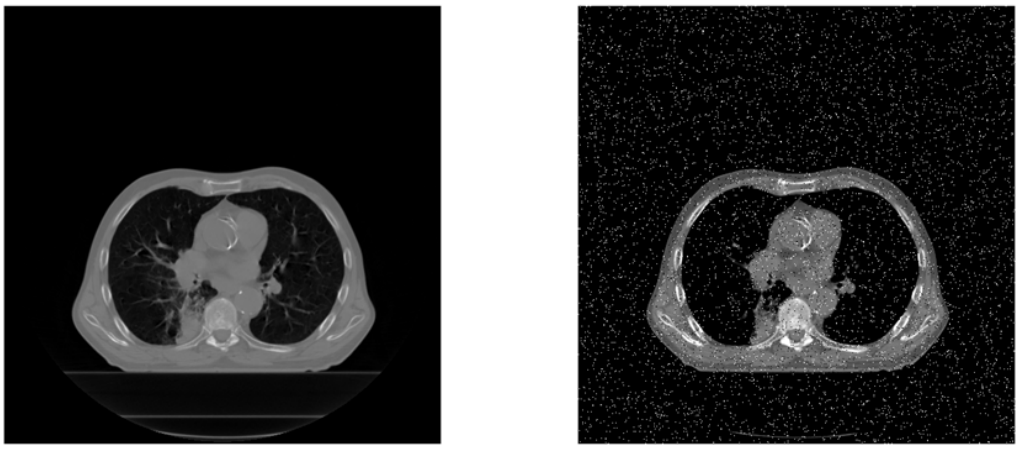

Figure 3.3: Left: the original CT image (512×512). Right: the noisy image with salt and pepper noise.

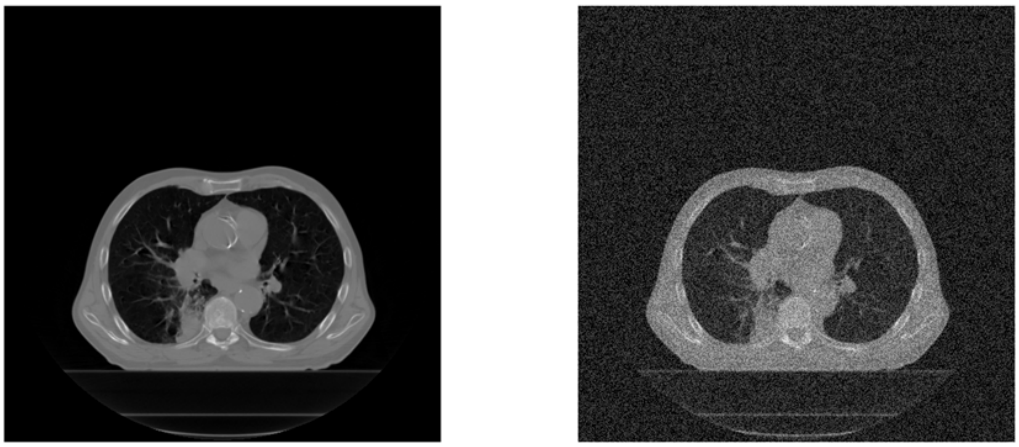

Figure 3.4: Left: the original image (512×512). Right: the noisy image with Gaussian noise which has 0 mean and 0.01 variance.

It is very difficult to remove all of the noise from an image and retain all of the useful information in it. There is always a balance between the sacrificing of real information and the noise reduction. Considering the computational cost and the quality needed for the further image processing algorithms, two simple de-noising methods were used here. Firstly, a low pass smoothing filter was used to smooth the original images by convolving the images with a smoothing mask. For every pixel, this mask contains the weights for its neighboring pixels and generates a weighted average to replace the original intensity. A typical smoothing filter is the Gaussian filter where the set of weights are normally distributed. The size and variance of Gaussian smoothing filter can be changed for different requirements. In general, the high

frequency signals in an image contains the information of variations in intensities and therefore smooth filters will blur an image. In other words, the extreme value of intensities in an image will be dispersed across its neighboring area. The smoothing filter is linear and is commonly used as the first step in de-noising. Another non-linear de-noising method is the median filter, which is more robust than smoothing filter and can preserve more real information in an image. The intensity of every pixel and its neighboring pixels are saved and sorted in a list. The median value of this list replaces the original intensity. This method is one of the rank-selection filter and can achieve different aims under different designs. Not only median, other values such as smallest, largest, closest or the most often occurs value can also be used.

3.2.4 Pre-segmentation of PET

^{18}F-FDG PET images are widely used to provide functional information which can improve the target delineation and the assessment of therapy response. The ability to use PET in radiotherapy planning was proposed in 2000 by Ling et al. PET may be used like any other anatomic imaging modality to define the GTV which has to be identified using a proper segmentation algorithm. Better definition can be obtained by combining PET with structural image modalities such as CT and MRI. Standardized uptake value (SUV) on ^{18}F-FDG PET images is an important indicator that is used to differentiate malignant from benign tumors, and has been applied in tumor volume segmentation. SUV represents the ratio of the actual radioactivity concentration found in a selected part of the body at a certain time point, and the radioactivity concentration in the hypothetical case of an even distribution of the injected radioactivity across the whole body as shown in Equation 3.3.

$$SUV(i,j) = \frac{R \times G(i,j) \times W}{IDO} \tag{3.3}$$

where R is the rescale slope, W is the total body weight, $G(i,j)$ is the gray value at point (i, j) and IDO is the injected dose after decay correction. R and W are usually recorded in the DICOM information and IDO can be calculated from the time difference between the time of injection and the scan time together with the half-life time of the isotope.

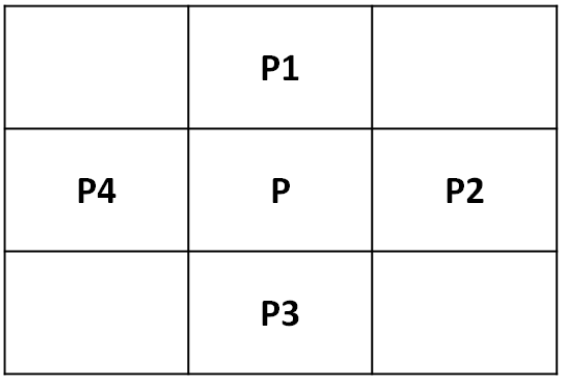

Figure 3.5: 4-connectivity scheme. P is the target pixel and P1-P4 are the neighboring pixels. Here the background pixels are marked as number 0 and target pixel is 1.

Four steps are included in the novel PET segmentation method proposed by Xin ming et al in 2012 [88]: Enhancement, coarse segmentation, label connected component and accurate segmentation. Firstly the PET images are enhanced by using Equation 3.4.

$$I_{en}(i,j) = \frac{SUV(i,j)}{SUV_{max}} \times I(i,j) \tag{3.4}$$

where I_{en} is the enhanced intensity and SUV_{max} is the maximum of SUV in the image. The enhanced image will be segmented by using a high pass filter whose threshold is set to be 40% of the highest enhanced intensity. Then the coarse segmented image is de-noised by using a 4-connectivity scheme as shown in Figure 3.5.

In the binary images, set the pixel in target as the number 1, and set the pixel in background as the number 0. The pixel $P(i,j)$ in image has 4 neighbors, P1, P2, P3, P4, as shown in Figure 3.5. If P is the target pixel, when its 4 neighbors have less than or equal to one of the target pixels, the point P is replaced by the number 0 as the background pixel. Using this way to eliminate noise provides relatively complete image segmentation components. Then the connected parts in the de-noised image will be labeled. An example of this pre-segmentation method applied on lung cancer images is shown in Figure 3.6.

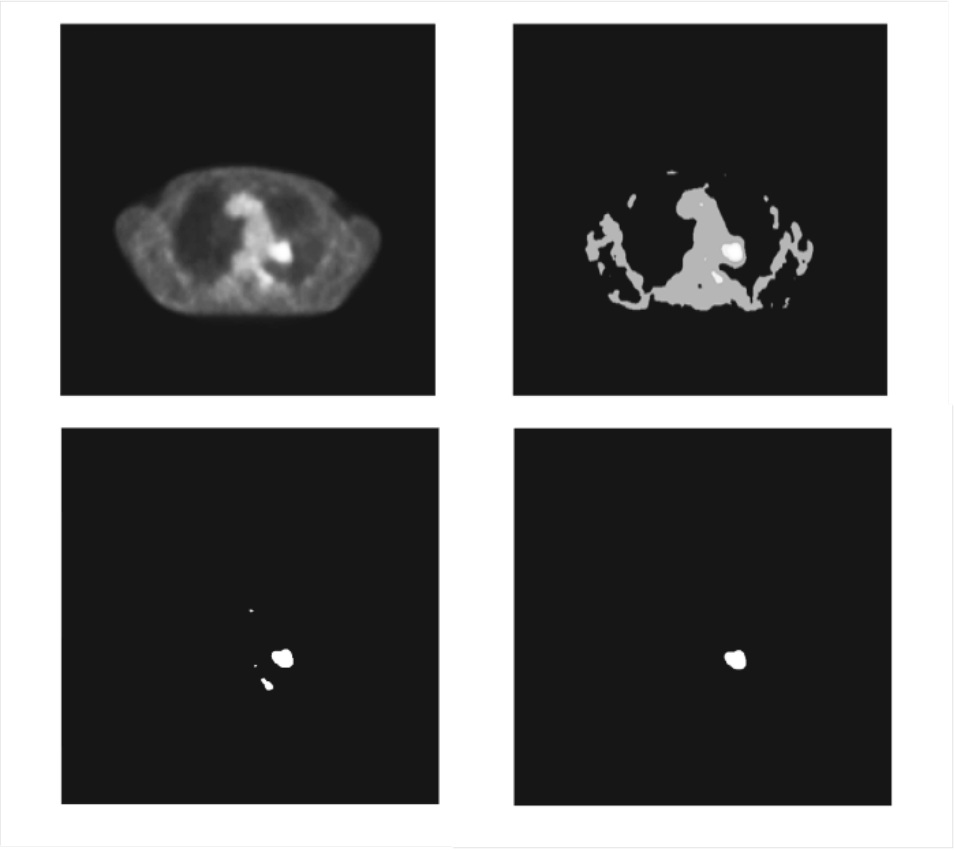

Figure 3.6: Original image (top left), SUV enhanced image (top right), coarse segmented image (bottom left), final segmented image (bottom right). Parts with high brightness can be treated as tumour volume.

3.3 Rigid registration

3.3.1 SIFT feature extraction algorithm

The SIFT algorithm is a method for mapping images based on matching features. It can find several feature descriptors which are invariant to image scaling, rotation and view point in any image. Feature matching can be done by individually comparing each feature in one image to features in another image based on the Euclidean distance [78].

The feature extracting can be divided into 4 stages:
1. Scale-space extreme value detection.
2. Keypoint localization.
3. Orientation assignment.
4. Keypoint descriptor.

In the first stage, features that are invariant to change in scale are found. The common scale-space kernel is the Gaussian function and therefore the scale-space L can be defined as:

$$L(x,y,\sigma) = G(x,y,\sigma) * I(x,y) \tag{3.5}$$

where σ indicates the scale, $*$ is the convolutional operation, I is the intensity of image and

$$G(x,y,\sigma) = \frac{1}{2\pi\sigma^2} e^{-(x^2+y^2)/2\sigma^2} \tag{3.6}$$

To efficiently find the stable points in scale-space, the extreme points in the difference-of-Gaussian (DOG) function convolved with the image as shown in Figure 3.7 can be computed by computing from:

$$D(x,y,\sigma) = L(x,y,k\sigma) - L(x,y,\sigma) \tag{3.7}$$

where k is a multiplicative constant.

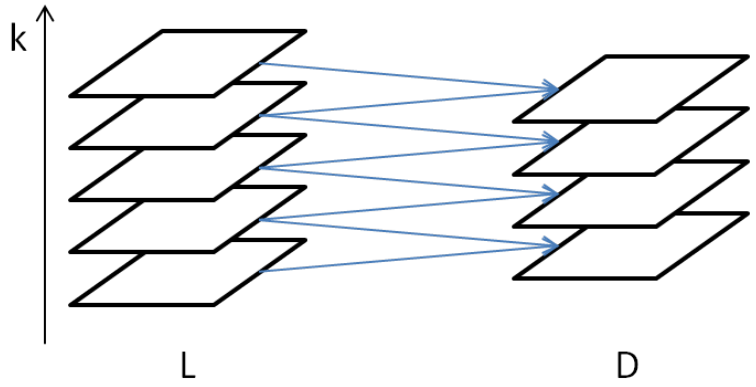

Figure 3.7: DOG calculation in scale space. The planes on the left represent scale space image with different k and on the right their difference generate the DOG images.

By finding the maximum or minimum point of D in the area including 8 neighbors and 9 pixels in the scale below and above, this can yield stable points in scale-space which is shown in Figure 3.8.

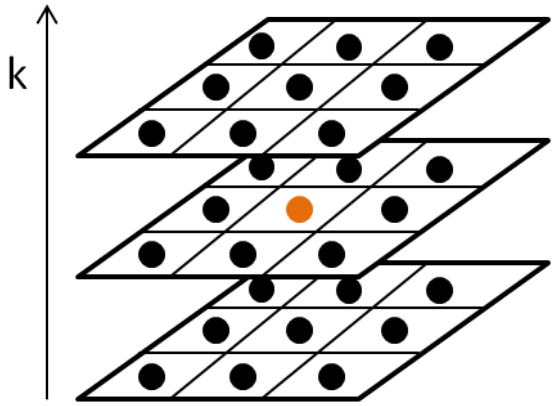

Figure 3.8: The extreme point in the scale-space. They are calculated from the maximum or minimum of 8 neighboring points of the target point (red) and corresponding 9 points above and below the target image in the scale space.

These selected points from the first stage can be treated as candidate keypoints. As these points do not include detailed information and have no restriction on contrast or edge effects, a further stage is used to fit information to them. The points with low contrast should be filtered out after information of scales, rotation and curvatures given to the keypoints. To eliminate edge responses, the Hessian matrix H is used. As studied by Harris and Stephens [48], a threshold (r) can be defined to constrain the edge responses as any poorly defined peak in the DOG will give a large principal curvature across the edge and a small one in the perpendicular direction. Function 3.8 can simply eliminate this effect.

$$\frac{Tr(H)^2}{Det(H)} < \frac{(r+1)^2}{r} \tag{3.8}$$

where the $Tr(H)$ represents the trace of H and $Det(H)$ is the determinant of H. The left side of this equation reaches its minimum value when the two eigenvalues are equal however, edge points are characterized by large variations in different directions. Therefore, the eigenvalues at edge points should have large difference and will obtain a large value at the left side of Equation 3.8 and exceed the threshold defined at the right side of Equation 3.8. In this thesis, r is usually set to be 10 [78].

The gradient is another image feature and therefore the third stage is to assign each keypoint an orientation based on the gradient as this will make the feature invariant to image rotation.

$$m = \sqrt{(L_{x+1,y} - L_{x-1,y})^2 + (L_{x,y+1} - L_{x,y-1})^2} \tag{3.9}$$

$$\theta = \tan^{-1}\left(\frac{L_{x,y+1} - L_{x,y-1}}{L_{x+1,y} - L_{x-1,y}}\right) \tag{3.10}$$

For every keypoint, a histogram can be formed by sampling and calculating the gradient of the pixels around it.

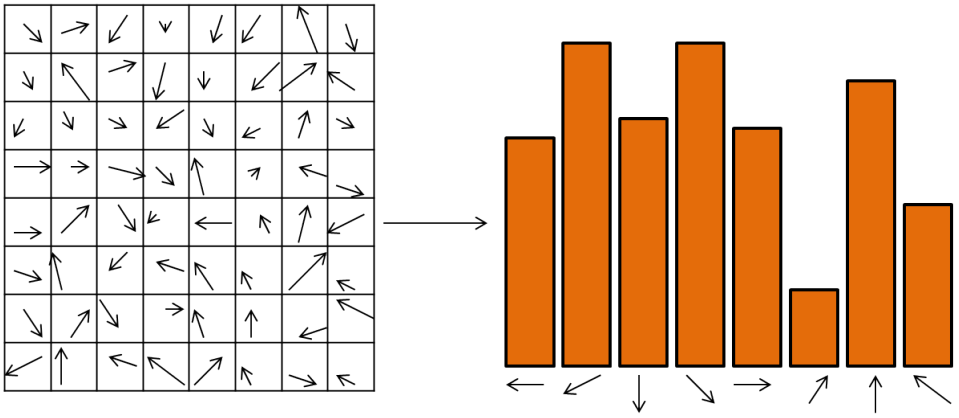

Figure 3.9: The histogram of gradient orientations. The threshold is set to be 80% of the highest peak in the histogram, any orientation represented by peaks higher than the threshold will be assigned to the keypoints.

Figure 3.9 illustrates that peaks in the histogram correspond to the main direction of the keypoint. Therefore, it is common to choose the highest peak and any peaks higher than 80% of the highest peak value. Every keypoint is assigned to one or several orientations.

In the first three stages, scale, location and orientation are assigned to the keypoints to make them invariant to these factors. Target objects in images will be made to be invariant to the viewpoint or illumination. An excellent approach based on gradient has been found by Edelman and used by David G. Lowe [78]. Firstly, the gradients and orientations over an 8×8 area around the keypoint are calculated. These data are then weighted by a Gaussian function that treats the keypoint as the center and is divided into 4 sub regions representing the gradient and orientation within it by arrows of a particular length as shown in Figure 3.10.

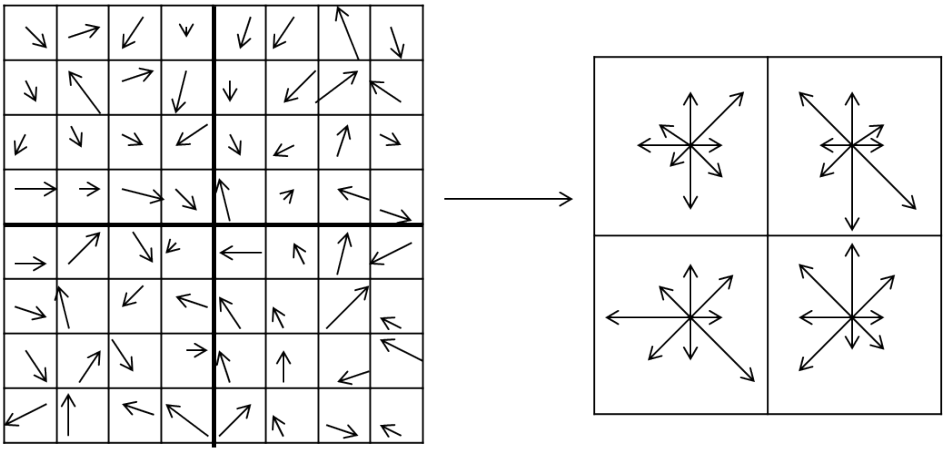

Figure 3.10: Gaussian weighted function over 8×8 region and the simplified results in 4 sub regions.

Finally, all features which include orientations and magnitudes of gradient, locations and scales are saved into descriptors of the keypoints.

3.3.2 MI similarity

Although SIFT can efficiently match images from different modalities together, there is a basic assumption that the position and shape does not change significantly. Therefore, noise, breath effects or other significant movement of patients will deteriorate the performance of this method. To make the image registration more general, the method based on MI which applies no limiting constraint on the images is proposed. Mutual information, also called relative entropy, is a general measurement of statistical dependence in information theory. In medical image registration, the images from different modalities can be treated as different variables which have intensities as function values against the pixel location. Therefore, the maximum mutual information gives a most possible related transformation function.

Assume there are two random variables A and B. Their marginal probability distributions are P_A and P_B, and their joint probability distribution is P_{AB}. Then the mutual information between A and B is defined as:

$$MI(A,B) = \sum P_{AB}(a,b) \log \frac{P_{AB}(a,b)}{P_A(a)P_B(b)} \tag{3.11}$$

MI is related to entropy by functions below:

$$MI(A,B) = H(A) + H(B) - H(A,B) \tag{3.12}$$

$$MI(A,B) = H(A) - H(A \mid B) \tag{3.13}$$

$$MI(A,B) = H(B) - H(B \mid A) \tag{3.14}$$

where $H(A)$ and $H(B)$ are the entropies which measures the uncertainty of random variables and $H(B \mid A)$ indicates the amount of uncertainty left in B when knowing A.

3.3.3 Rigid registration method

The method presented here contains four stages: image conditioning; feature extraction with SIFT; calculation of MI; and optimization. De-noising, re-sampling of the original data set and the down-sampling of the resulting images were included in the image conditioning stage where bilinear interpolation method was used. In image registration, matching common features in the reference and target image can reduce computation. However, it is often difficult to identify suitable features acquired on different imaging modalities because of differences in resolution, scale and position. The SSD between SIFT descriptors is commonly used as the cost function to find matches between feature points. However, in the proposed method, SIFT is only used to identify representative feature points with appropriate parameters.

As shown in Figure 3.11, the similarity function is calculated from the MI between the pixels in the small squares on the reference and target images. The small squares, generally set to be 3×3 pixels, are regions around reference feature point (RFP) and target feature point (TFP). The selected RFP and TFP are not necessarily matched SIFT feature points as their neighboring regions are calculated respectively. Pixels within these regions can be divided into 4 groups (Figure 3.11): regions around RFP on the reference image ($A1$), regions around RFP on the target image ($B1$), regions around TFP on the reference image ($A2$) and regions around TFP on the target image ($B2$). A rigid transform was applied to the target data set to alter the position of the features and therefore alter the values in A and B. The MI of the feature points and the neighboring points between the reference image and the target image were calculated using Equation 3.11.

Therefore the problem of physical background and reconstruction field background pixels, which can significantly affect the accuracy of the MI-based method, was removed because only feature areas are included in the calculation. The details of choosing the number of feature points and implementation are discussed in Section 6.6.

For a typical 3D case, the squares become cubes as shown in Figure 3.11. The optimization algorithm was then performed on the 7-dimensional parameter space (T_x T_y T_z α β γ scale) over a 1 pixel, 1° and 0.1 scale interval to find the global maximum representing the best match as shown in Equation 3.15. In this thesis, L-BFGS and simulated annealing optimization functions in MATLAB (statistical toolbox) were used to optimize the similarity function. As a result, the best rigid transform from the target image to the reference image can be calculated as:

$$T_{best\_rigid} = \arg \max_{T_{rigid}(\alpha,\beta,\gamma,T_x,T_y,T_z,scale)} MI(A,B)_{T_{rigid}(\alpha,\beta,\gamma,T_x,T_y,T_z,scale)} \tag{3.15}$$

where $A = (A1, A2)$, $B = (B1, B2)$, T_{best_rigid} is the calculated best rigid transformation function between the reference and target data set and $MI(A,B)$ is the MI between A and B under the current rigid transformation.

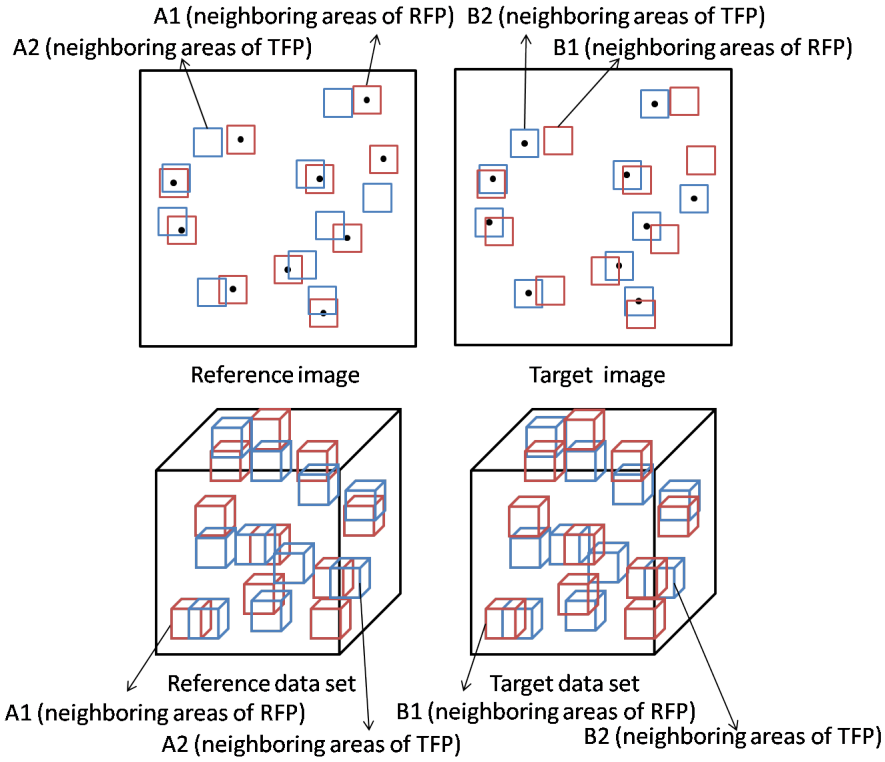

Figure 3.11: Top: SIFT feature points on both the reference and target images with neighboring areas around them (3×3) shown as small squares. Bottom: 3D example of neighboring areas of SIFT feature points on the reference and target data set shown as small cubes ($3 \times 3 \times 3$).

3.4 Non-rigid registration

3.4.1 Cubic B-spline method

A B-spline interpolation method is used to generate a smooth distribution as shown in Equation 3.16, where x, y, and z denote the coordinates of the image, B are the basis functions of the B-spline, φ is the $nx \times ny \times nz$ mesh of control points. Equation 3.17 and 3.18 define i, j, k, u, v, w and the basic functions of the B-spline.

$$T(x,y,z) = \sum_{l=0}^{3}\sum_{m=0}^{3}\sum_{n=0}^{3} B_l(u)B_m(v)B_n(w)\phi_{i+l,j+m,k+n} \tag{3.16}$$

$$\begin{aligned} i &= \lfloor x/n_x \rfloor - 1 \qquad u = x/n_x - \lfloor x/n_x \rfloor \\ j &= \lfloor y/n_y \rfloor - 1 \qquad v = y/n_y - \lfloor y/n_y \rfloor \\ k &= \lfloor z/n_z \rfloor - 1 \qquad w = z/n_z - \lfloor z/n_z \rfloor \end{aligned} \tag{3.17}$$

$$\begin{aligned} B_0(u) &= (1-u)^3/6 \\ B_1(u) &= (3u^3 - 6u^2 + 4)/6 \\ B_2(u) &= (-3u^3 + 3u^2 + 3u + 1)/6 \\ B_3(u) &= u^3/6 \end{aligned} \tag{3.18}$$

3.4.2 Gabor filter

A Gabor filter is a powerful feature extraction method which has been widely used in pattern analysis and image analysis applications. Similar to SIFT feature extraction, features extracted by Gabor filter are invariant to illumination, rotation, scale, and translation. Furthermore, they can withstand photometric disturbances, such as illumination changes and image noise [42]. Here, within a non-rigid registration method, Gabor filters can provide Gabor features for every pixel on an image and can be used to identify the correspondences between feature points instead of the SIFT method.

Equation 3.19 shows the 2D Gabor filter, where f is the frequency of the sinusoidal factor, σ is the standard deviation of the Gaussian kernel which can be calculated from f, ϕ is the phase offset (set to be 0), θ is the orientation of the normal to the stripes of the Gabor filter and ζ is the spatial aspect ratio (set to be 0.5) [66].

$$\begin{aligned} G_{x,y} &= \frac{f^2}{\pi\zeta\eta}\exp\left(-\frac{x'^2 + \zeta^2 y'^2}{2\sigma^2}\right)\exp(j2\pi f x' + \phi) \\ x' &= x\cos\theta + y\sin\theta \\ y' &= -x\sin\theta + y\cos\theta \end{aligned} \tag{3.19}$$

As shown in Figure 3.12, the corresponding feature point i on the target image for the j_{th} feature point on the reference image can be calculated as:

$$i = \arg\min_{i \in R}\left(\sum_{k=1}^{n_g}(GR_j(k) - GT_i(k))^2\right)^{1/2} \tag{3.20}$$

where R is the neighboring region on the target image shown in Figure 3.12, $GR_j(k)$ is the k_{th} Gabor feature element of the j_{th} point on the reference image and $GT_i(k)$ is the k_{th} Gabor feature element of the i_{th} point on the target image. n_g is the number of Gabor features for every pixel

and is decided by the number of selected orientations and the number of scales. Here 8 orientations (to be consistency with SIFT orientations) and 5 scales ($f = 0.1, 0.2, 0.3, 0.4$ *and* 0.5) were selected for the Gabor feature extraction. As a result, for every pixel, 40 (5×8) features were extracted [66]..

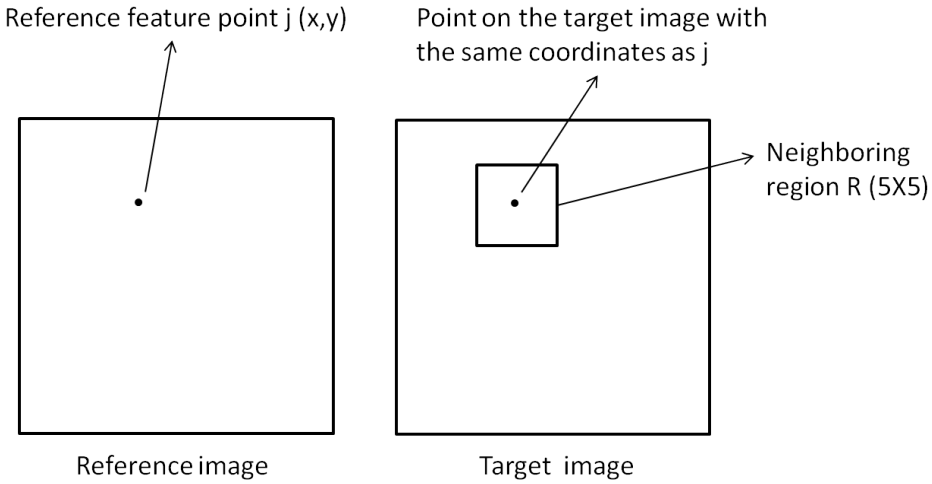

Figure 3.12: Calculation of corresponding feature point i by minimizing the SSD between point j and all points in its neighboring region on the target image.

Similarly, SIFT can be used to find the correspondence between feature points too. SIFT can find feature descriptors which are invariant to image scaling, rotation and view point for feature points on both the reference and target image as shown in Figure 3.13.

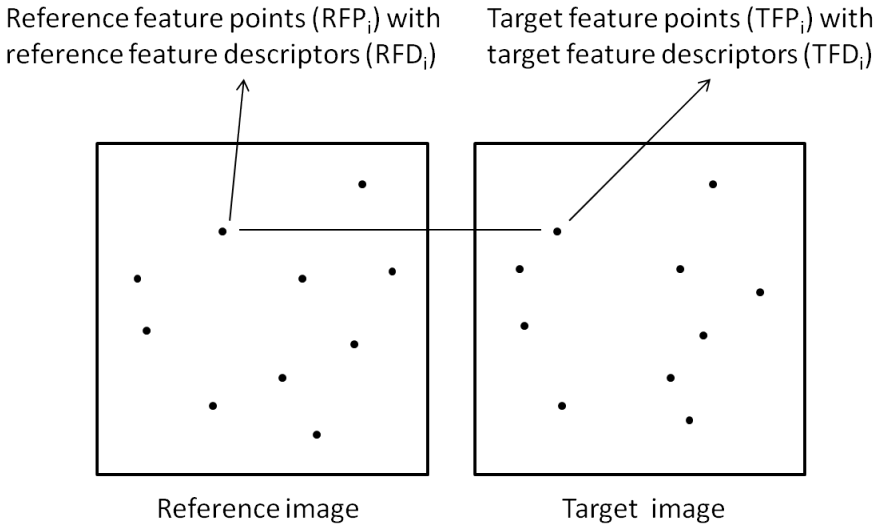

Figure 3.13: SIFT feature points on both the reference and target images with corresponding feature descriptors.

Descriptors extracted from RFP are defined as reference feature descriptors (RFD) while descriptors extracted from TFP are defined as target feature descriptors (TFD). Matching of feature points can be done by minimizing the Euclidean distance between RFD and TFD. Specifically, as shown in Equation 3.21, the corresponding feature point i on the target image for the j_{th} feature point on the reference image can be calculated as:

$$i = \arg\min_{i}(\sum_{k=1}^{n_d}(RFD_j(k) - TFD_i(k))^2)^{1/2} \tag{3.21}$$

where $RFD_j(k)$ is the k_{th} element in the j_{th} reference feature descriptor and $TFD_i(k)$ is the k_{th} element in the i_{th} target feature descriptor. n_d is the size of SIFT descriptor which can be varied based on different situations. It can be calculated from the size of the neighboring region and the number of selected orientations as mentioned in Section 3.3.1. In this thesis, a 16×16 neighboring region around feature points was considered to be the most relevant region and 8 orientations are used to summarize the direction of feature points [78]. As a result, n_d was 128 (16×8).

Gabor filters can also be used to identify the correspondence between feature points on clinical contours. For example, Gabor features are used to identify the correspondence between two prostate contours on planning CT and diagnostic MRI images which are shown in Figure 3.14. The identified corresponding contour points can then be used to guide a non-rigid registration between CT and MRI images and therefore provide the deformation map between them.

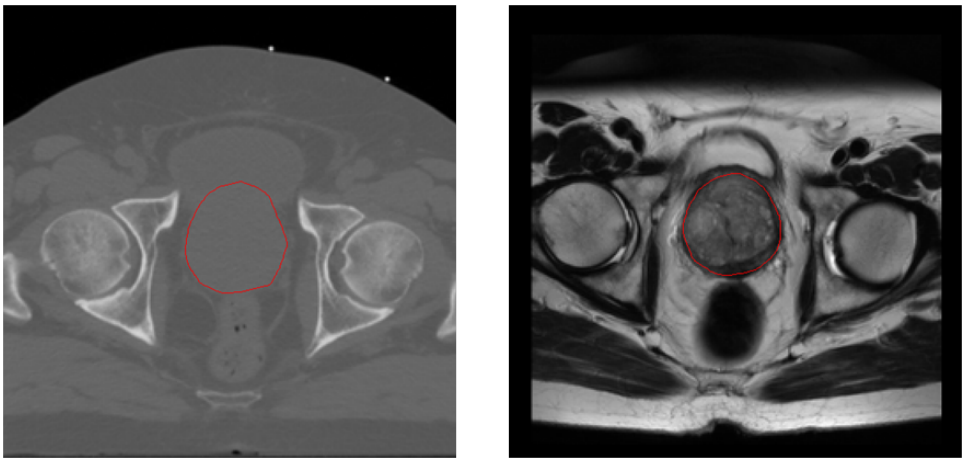

Figure 3.14: The original reference image (planning CT image on the left) and the pre-processed target image (diagnostic MRI image on the right) with clinical prostate contour in red. The contour was reconstructed and re-sampled using the method presented in Section 3.2.2.

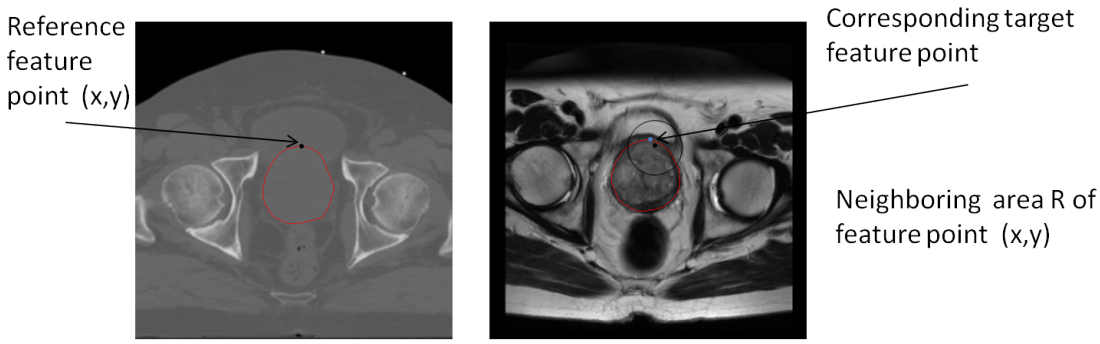

Figure 3.15: One example for the reference feature point (x,y) in black on the reference prostate contour and its corresponding target feature point in blue on the target prostate contour. Black circle on the target image shows the neighboring region of the reference point.

As shown in Figure 3.15, three conditions must be satisfied to find the corresponding feature point i on the target image for the j_{th} feature point on the reference image:
1. Point i must be on the target contour.
2. The difference between the Gabor features of point i and j must be smaller than the difference between point j and all the other feature points on the target contour.
3. Point i must fall in the neighboring region R of point j. Therefore, i can be calculated as:

$$i = \arg\min_{i \in C \cap R} \left(\sum_{k=1}^{n_g} (GR_j(k) - GT_i(k))^2\right)^{1/2} \tag{3.22}$$

where C is the set of contour points on the target image and R is the neighboring region shown in Figure 3.15.

3.4.3 Non-rigid registration method

Non-rigid registration is applied after the rigid approach for registering multi-modality images, including those with distortions such as MRI. In the method presented, SIFT and the Gabor filter are re-coded to find feature points and their correspondence only on the contours of organs defined by clinicians. A robust similarity function including the SSD between extracted feature points and MI between pathologically identified distinctive regions was used. A cubic B-spline method was applied to generate a smooth interpolation in the non-rigid transformation. As shown in Figure 3.16 (same modality) and Figure 3.17 (different modalities), feature points (criteria 1) and distinctive regions (criteria 2) are used to balance the similarity function and guide the process of non-rigid registration.

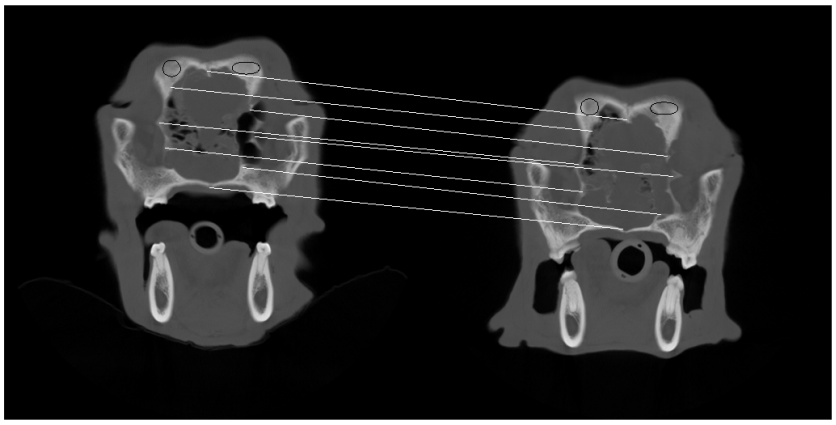

Figure 3.16: Feature points and distinctive regions on images with same modality.

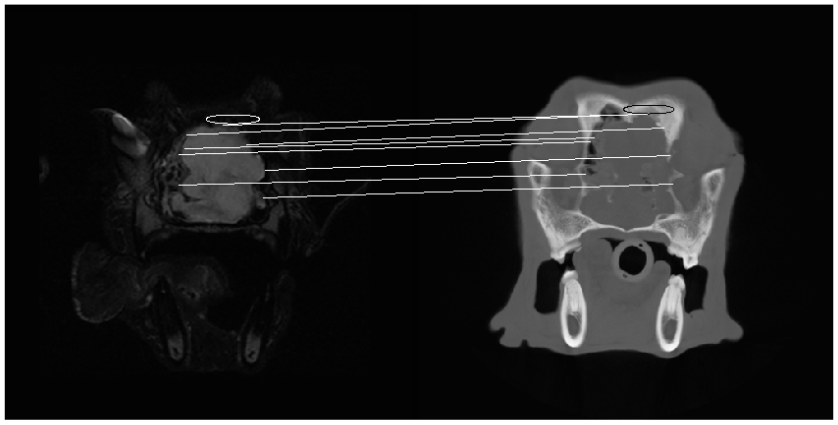

Figure 3.17: Feature points and distinctive regions on images with different modalities.

Criteria 1

The first criteria is the SSD between corresponding feature points extracted by SIFT or Gabor filter. For every slice, n_m best matches between feature points in the area of interest are selected and the SSD is optimized by changing the position of the control grid in the B-spline method as shown in Equation 3.23.

$$\begin{aligned} C_1 = \sum_{i=1}^{n_m} ((Rx_i - T_{nonrigid}(T_{best\_rigid}(Tx_i)))^2 \\ +(Ry_i - T_{nonrigid}(T_{best\_rigid}(Ty_i)))^2) \end{aligned} \tag{3.23}$$

where Rx_i and Ry_i are the coordinates of RFP_i, Tx_i and Ty_i are the coordinates of TFP_i illustrated in Figure 3.13 and n_m was set to be 10.

Feature points on the target image are transformed by the best rigid transform function T_{best_rigid} obtained from Equation 3.15 before calculation of C_1, which will remove the rigid difference between feature points. This criteria provides a point-point similarity measurement which is particularly important for contour mapping. This is because feature points always have a high gradient which makes them more likely to be a point on or around the contour. Therefore, optimizing the SSD of these feature points will minimize the difference between the key points on the contours. However, soft tissues may change their shape during the treatment, which makes it less efficient to identify just points for a registration method. Regions around the GTV with distinctive features which can hardly be changed during the radiation therapy are included in the similarity function to overcome this problem.

Criteria 2

The second criteria is the MI between manually identified corresponding distinctive regions. For example, in Figure 3.16 and Figure 3.17, bones are selected to be the distinctive regions. Similarly as in Equation 3.11, pixels within the distinctive regions on the reference image (DR) and the distinctive regions on the target image (DT) are saved in A and B respectively. Then criteria 2 can be calculated as:

$$C_2 = \sum_{A=DR, B=T_{nonrigid}(T_{best\_rigid}(DT))} P_{AB}(a,b) \log \frac{P_{AB}(a,b)}{P_A(a)P_B(b)} \tag{3.24}$$

Not only image information is included in DR and DT, histopathological information can also be included here in the same way that experience of a clinician is used as prior knowledge during the identification of these regions.

Therefore, the best non-rigid registration can be addressed by the following equation:

$$\begin{aligned} T_{best\_nonrigid} = \arg\min_T (& w_1 C_1 + w_2 C_2 \\ & + w_3 \left\| \int_x \int_y \left(\frac{\partial^2 T}{\partial x^2} + \frac{\partial^2 T}{\partial y^2} \right) \right\|^2) \end{aligned} \tag{3.25}$$

where T is non-rigid transform function, w_1, w_2 and w_3 are manually defined weights. Numerically, the second order derivative in the regularization term can be calculated as the difference between its first order derivative: $\frac{\partial^2 T}{\partial x^2} = (T(x+1,y) - T(x,y)) - (T(x,y) - T(x-1,y))$.

For the test cases in this thesis, w_1, w_2 and w_3 are manually set to be 2, -10000 and 0.01 respectively. The details of choosing parameters and implementation are discussed in Section 6.6.

3.5 Level set segmentation and further segmentation

Level set method can be used to find the shape and volume variation of the GTV on follow-up images and images acquired at time-of-treatment such as CBCT. Level set method can also work robustly on images from different modalities and are capable of identifying topological changes in target contours automatically with the appropriate initialization. Here, a level set method was re-coded to initialize with the contour provided by the registration methods (both rigid and non-rigid). As a result, both the position and the shape of the zero level set function are set to the appropriate value for further segmentation automatically.

In level set theory an evolving contour is treated as the zero level set which is a 2D interface of a 3D level set function and the plane of the image [111]. This makes it easier to deal with target shapes with sharp corners or topology changes in higher dimensions [6]. The zero level set function $c(t)$ represents the evolving contour at time t and $u(t)$ is the signed distance function of $c(t)$. Thus, for every point (x,y) on the plane, its distance to the contour $c(t)$ is calculated in $u(t)$ ($+ve$ inside and $-ve$ outside). Therefore, for every point $(x(t),y(t))$ on the contour $c(t)$ [82],

$$u(x(t),y(t)) = 0 \tag{3.26}$$

Differentiating using the chain rule, the basic level set function is [4]:

$$u_t + F\,|\bigtriangledown u| = 0 \tag{3.27}$$

where F is the speed function [111], Δt is the time interval (set to be 0.02) and the space interval is 1 pixel. It follows that Equation 3.27 can be rewritten as [82]:

$$\frac{u^{n+1}-u^n}{\Delta t} + F(\bigtriangledown u^n) = 0 \tag{3.28}$$

For every u^n, given F and Δt, u^{n+1} can be calculated. Here, the registered GTV contours from pre-treatment images were used as the initial zero level set function as shown in Equation 3.29 and parameters ($\Delta t = 0.01$ in the test cases) were set appropriately to evolve the level set towards the GTV contour on the follow-up image sets. The parameters of the level set can be adjusted for different cases to increase the efficiency and accuracy of the segmentation result. In this way the algorithm provides an automatic approach for identifying changes in the GTV over time due to soft tissue change and in response to radiotherapy.

$$c(0) = T^{-1}_{best\_nonrigid}(T^{-1}_{best\_rigid}(C_R)) \tag{3.29}$$

where C_R is the original reference contour and the automatic generated contour C_G from this framework will be compared with the original target contour C_T.

3.6 Dice coefficient

The Dice coefficient is a commonly used measurement for evaluating the similarity between two data samples. In this thesis it was used to describe the similarity between two contours. The Dice coefficient between contour a and b can be calculated as:

$$D = \frac{2 * |A \cap B|}{|A| + |B|} \tag{3.30}$$

where A and B represent the pixels inside a and b. Therefore, D varies from 0 to 1 representing a and b are totally different or completely the same.

3.7 Conclusion

In this chapter, various image processing algorithms used in this thesis were introduced. Among them, image conditioning (pre-processing) algorithms were applied on test data sets firstly to make the row image data more suitable for the follow-up algorithms. Also, the pre-processing algorithms of clinical contours including reconstruction and re-sampling based on Delaunay triangulation was presented.

The rigid registration algorithm presented was designed to find the rigid mapping between images from the same modality or different modalities. As a result, it is sufficient for the registration between images from the same modality and can be used as a pre-processing step for the non-rigid algorithm. SIFT was used as a feature extraction method in it which makes the rigid algorithm invariant to scale changes to find corresponding feature points on the reference and target images. The MI between corresponding feature points were optimized to find the best rigid transformation parameters.

In the non-rigid registration algorithm, both the Gabor filter and SIFT can be used to extract feature points and their descriptors. The similarity function of this method includes a SSD measurement between feature points and a MI measurement between distinctive regions. This method is capable to find the distortion field based on B-spline interpolation method and is able to find the variation between organs (eg. prostate) on different images.

Level set method is a widely used active shape method which is robust on medical images. It can find the topology changes of the contours automatically and is sensitive to intensity changes on CT images under appropriate parameter setting. The only problem is that it needs careful initialization. As a result, both rigid and non-rigid registration algorithms were used to provide this initialization for level set method. These algorithms form a registration-segmentation framework which can provide automatic tumor segmentation on the target image.

Chapter 4

Performance of rigid registration method

4.1 Introduction

PET is a functional imaging technique that focuses on detecting physiological activities. It has very poor resolution and the contrast of PET images is highly related to the standardized uptake value (SUV) of the tracer used. In Section 4.3, algorithms based on SUV of PET imaging introduced in Section 3.2.4 were tested on PET images from lung cancer patients. Segmented PET images can then be used for further registration.

Rigid registration is widely used to map images with the same modality and can be treated as a pre-processing method before non-rigid approach. Rigid methods usually involve a simple transformation model and similarity function. The accuracy of conventional rigid methods can be heavily affected by noise or scale changes. In this chapter, rigid registration methods developed for images with little distortion was tested. Here, SIFT was used as a feature extraction method and MI between the neighboring areas of feature points was optimized as a similarity measurement. In Section 4.4, a Radionics Phantom 2 (Radionics, Inc., Burlington, MA), geometric verification phantom, was used to test the rigid registration approach as there are fewer distortions between CT and MRI images in phantom data than real data of patients.

CBCT images are obtained during the time of treatment and can illustrate the position of patients in the view of the radiation beam. As a result, the registration between them and planning CT images can provide guidance on radiation delivery. In Section 4.5, CBCT images from lung cancer patients were used to validate this approach. CBCT data taken at different fractions were registered with planning CT images. It is particularly difficult for clinicians to identify soft tissue boundaries on CBCT images because of their movement artifacts and low signal-to-noise ratio. As a result, the Dice coefficient cannot be used to assess the performance of the registration approach. Here the performance was assessed using the transformation matrix calculated by the method introduced in Section 4.5.1. The transformation applied at time-of-treatment to align the CBCT images of the patient with the RT planning CT images was saved in this matrix and used as the gold standard for assessing registration performance. The

registration between planning CT images and EPID images is also a commonly used method to ensure that the patient is positioned in the correct location for treatment. In Section 4.6, rigid registration approach was tested on them.

4.2 Test data

In this chapter, various data sets from different modalities including CR, MRI, PET, EPID and CBCT were used to test and validate the rigid registration algorithm and the PET pre-segmentation algorithm. 135 re-sampled PET images acquired on a lung cancer patient were selected on which slices (containing clear tumor volumes) were used for testing the segmentation algorithm. The PET images were re-seized to 512×512 and the pixel size is 1.0371 mm$\times$1.0371 mm. Figure 4.1 shows a typical PET slice and its corresponding histogram in which the intensity of the PET image was re-scaled to 0-100.

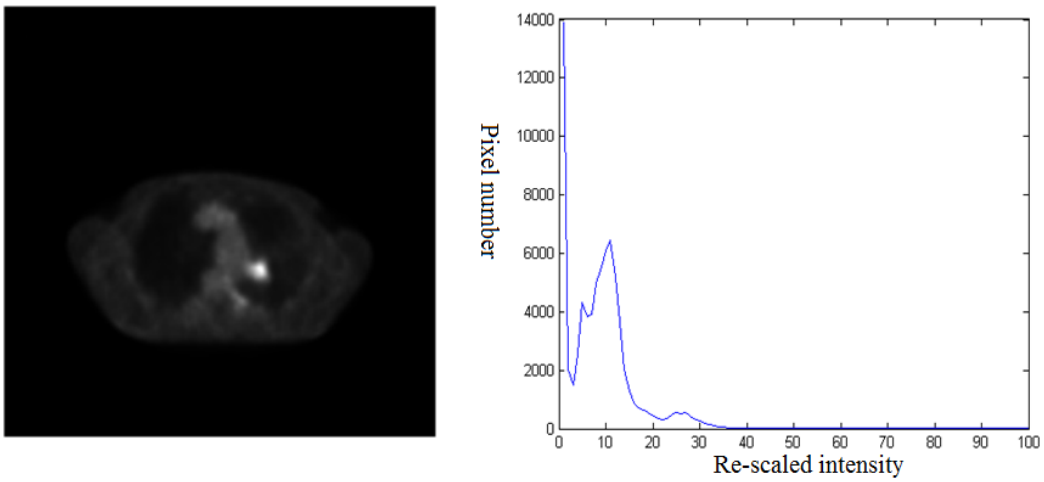

Figure 4.1: Original PET image (left), histogram with re-scaled intensity(right).

To test the SIFT-MI based rigid registration method, 3 different data sets were used here. Firstly, a Radionics Phantom 2 (Radionics, Inc., Burlington, MA), geometric verification phantom routinely used for quality assurance in stereotactic radiotherapy, was used. In this case, CT and MRI images have the same resolution, same pixel size and same contents including squares, circles and triangles. The aim of using this phantom data was to test how the registration algorithm works between different modalities which have simple background and little noise. Another phantom data set with soft tissues inside include both CT and MRI data was also used to test this algorithm. Here, the variation of intensities on images of both modalities was more complex. The size of MRI image is 230×230 and the the size of CT image is 512×512 as shown in Figure 4.2. The aim of using this data set was to test how the registration algorithm works after the re-sampling and down-sampling pre-processing.

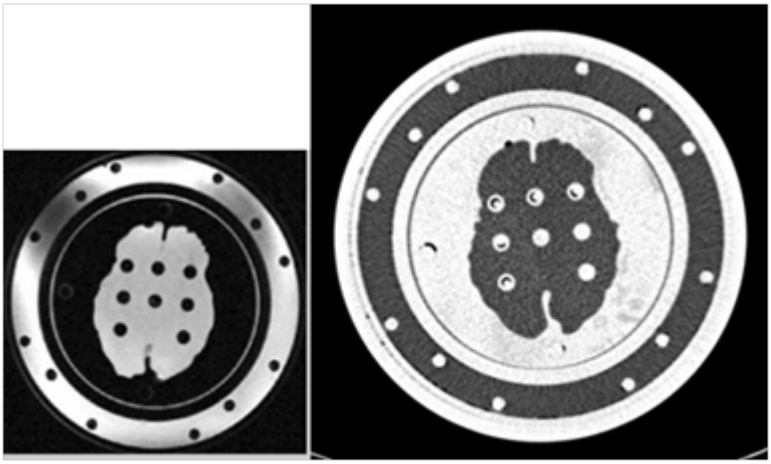

Figure 4.2: The original practical data with soft tissues inside (Left: MRI, Right: CT).

Secondly, DRR and EPID images which are commonly used to verify the position of patients in RT were used to test the performance of the registration algorithm on images with different scales and from different modalities. 512×512 DRR images and 244×244 EPID images were included in this practical data set.

Lastly, 5 data sets of CBCT images from lung cancer patients previously treated at the Edinburgh Cancer Center were used to validate the performance of this algorithm. CBCT images from different fractions of treatment which were taken at different time points and planning CT images are available for registration in this data set (details of CBCT images are shown in Table 4.1). A transformation matrix manually generated by radiographers when they shifted the patient on the treatment couch was used as the gold standard. The final performance was therefore objectively assessed by comparing the automatically generated transformation parameters and the parameters extracted from transformation matrix. Figure 4.3 shows an example of this data set from patient 5. On the left is the planning CT image which was taken before the treatment with the image size of 512×512, the pixel size of 0.9766 mm$\times$0.9766 mm and slice thickness of 3 mm. On the right is the CBCT image taken at fraction 10 with the image size 384×384, the pixel size 1.1719 mm$\times$1.1719 mm and the slice thickness 3 mm. The aim of using this data set was to assess how well this algorithm works in 2D and 3D cases and how well it works with images with poor resolution and complex background (CBCT).

Case Number	Fraction Acquired	Slice Number	Date of CBCT
Case 1	fraction 10 of patient 1	53	2010\04\30
Case 2	fraction 10 of patient 2	53	2010\05\05
Case 3	fraction 1 of patient 3	53	2010\05\10
Case 4	fraction 10 of patient 3	53	2010\05\21
Case 5	fraction 1 of patient 4	53	2010\06\08
Case 6	fraction 10 of patient 4	53	2010\06\22
Case 7	fraction 1 of patient 5	53	2010\06\21
Case 8	fraction 6 of patient 5	53	2010\06\28
Case 9	fraction 11 of patient 5	53	2010\07\05

Table 4.1: The details of the CBCT data for 5 lung cancer patients.

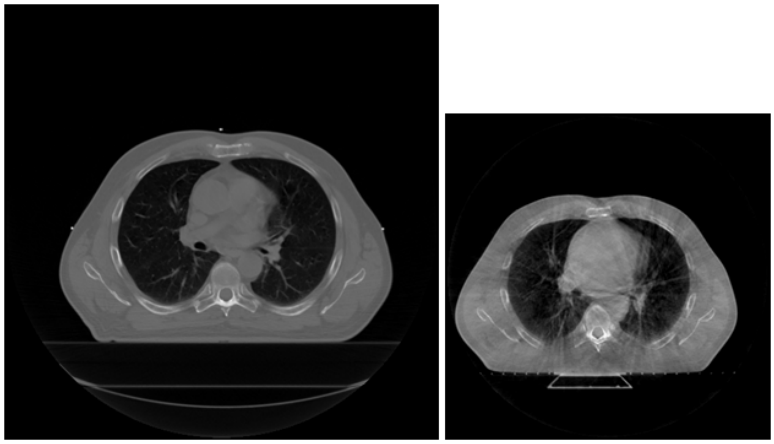

Figure 4.3: Left: the original planning CT image (512×512) which is the reference image. Right: the original fraction 10 CBCT image (384×384) which is the target image.

4.3 Results of PET segmentation

The decay corrected total dose for this case is 368.348 MBq, the body weight is 64.6 kg and the rescale slope is 1. According to Equation 3.3, the SUV is $1.7538 \times 10^{-4} \times G(i, j)$, where $G(i, j)$ is the gray level (intensity) at (i, j). Here, obviously the SUV and the intensity of the same image are linearly correlated. The SUV distribution is shown in Figure 4.4.

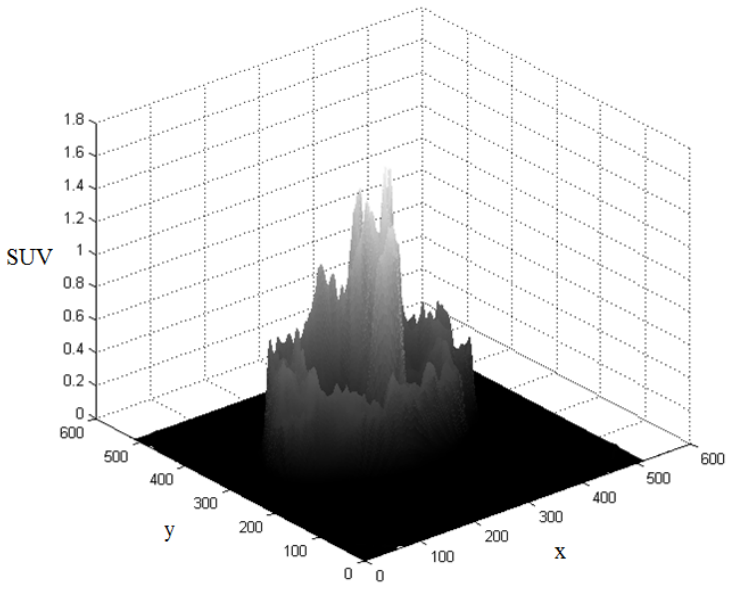

Figure 4.4: The SUV distribution of selected PET image where the heights represent the SUV for every pixel.

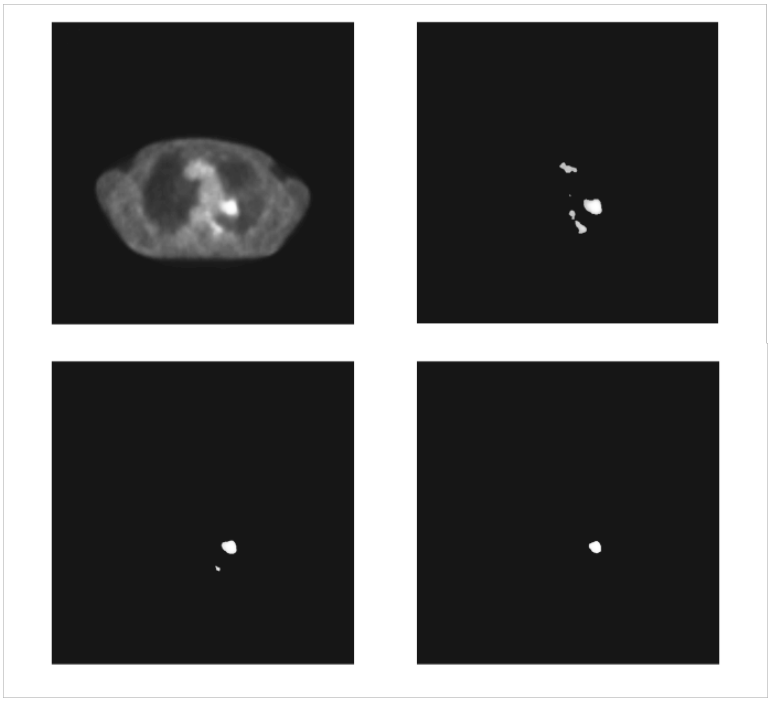

Figure 4.5: Original image (top left), 30% of the SUV_{max} filtered image (top right), 40% of the SUV_{max} filtered image (bottom left), 50% of the SUV_{max} filtered image (bottom right).

Figure 4.5 shows segmentation results with different thresholds. Thresholds of 30%, 40%, 50%

of the SUV_{max} were applied on the original image. Smaller thresholds may treat the organ with high metabolism as a tumor volume and give misleading results. Although a high threshold gives a single part of tumor volume, without histopathological correlation the results cannot be measured objectively. This is the biggest disadvantage of the thresholding method: it is very hard to find a general threshold good enough for every case.

Here an automatic and adaptive method was used in this paper (Section 3.2). The segmented results are shown in Figure 4.6.

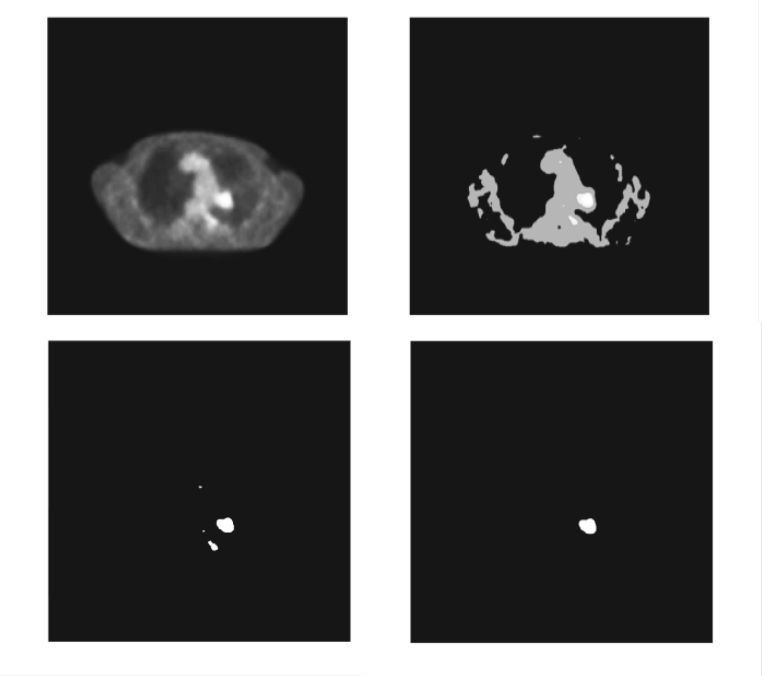

Figure 4.6: Original image (top left), SUV enhanced image (top right), coarse segmented image (bottom left), final segmented image (bottom right).

4.4 Performance on phantom data

The rigid registration method has been tested on regular phantom data and clinical data. The CT and MRI data were mapped with an average error rate of 1.5% on the phantom data shown in Figure 4.7.

	T_x	T_y	T_z	α	γ	β
Actual	0	0	0	90	-90	0
Calculated	0	0	9	90	-90	0
Shift Range	100	100	100	/	/	/
Rotation Range	/	/	/	180	180	180
Error Rate	0	0	9%	0	0	0
Average Error Rate	1.5%					

Figure 4.7: The performance of the rigid algorithm on phantom data by using best parameters.

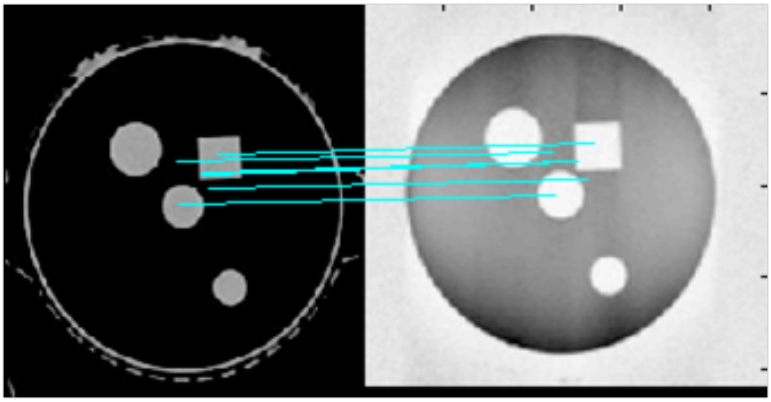

Figure 4.8: The matches between 2D example of phantom data sets (Left: CT, Right: MRI).

Figure 4.8 is an example of the registration on phantom data. It shows 5 matches between a CT image (left) and a MRI image (right). Although these two images have totally different histograms, the lines on them show clear matches between the feature points which are the endpoints of lines. The best features can be represented by the feature points and their neighboring pixels. The calculation of mutual information between neighboring areas of these points can provide more accurate results than the calculation between all pixels in images.

Figure 4.2 gives a more complex example used to test the algorithm. The left image is a 230×230 MRI image and the right one is a 512×512 CT image. Clearly they are of the same object

but have different resolutions, different orientations and different contrast.

Figure 4.9 shows the registered MRI image. It is a 512×512 MRI image which includes the spatial information of the original CT image. The registered image is generated from the original MRI image with a scale parameter of 1.89, a rotation parameter of 15° and a translation parameter of 2 and 3 in x and y direction respectively. Bilinear interpolation was used to generate the registered image.

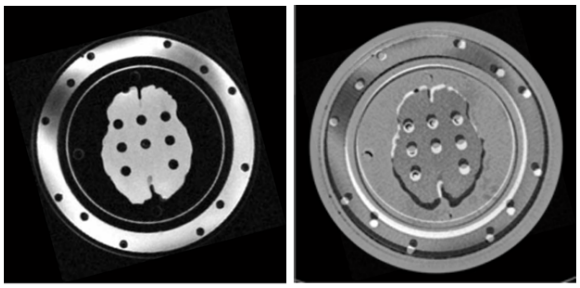

Figure 4.9: Left: the registered image (MRI, 512×512) with spatial information from the original CT image, high resolution and the clarity of MRI image. Right: the registered MRI image overlaid with the CT image.

4.5 Performance on CBCT data

4.5.1 Validation

The test results on CBCT images were validated by using the transformation matrix generated by the radiographers as a gold standard for this rigid registration method. The transformation matrix gives the transformation parameters (translation and rotation) for a 3D volume and can be calculated from the DICOM information discussed in Chapter 2.

As shown in Figure 4.10, three transformation matrices T_1, T_2 and T_3 (all of them are 4×4) are the key parts to calculate the mapping between the reference and target images. T_1 and T_2 can be calculated using Equation 4.1 using DICOM information from the reference and target images respectively.

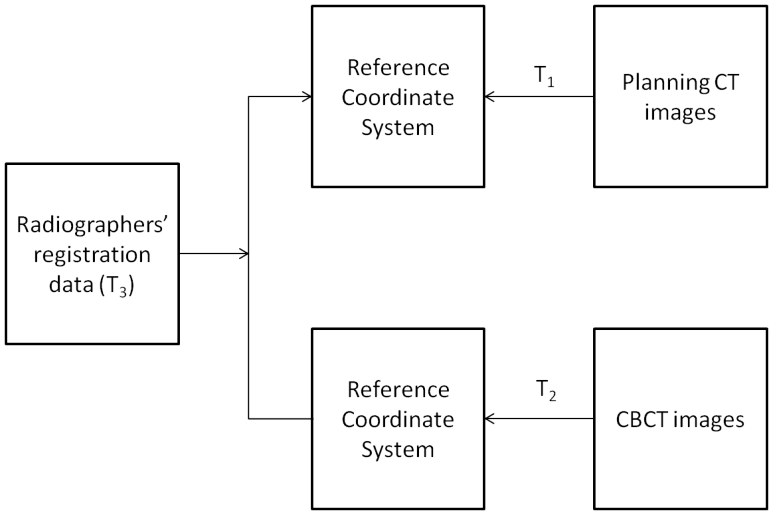

Figure 4.10: The relationship between the reference image (planning CT), the target image (CBCT) and their RCS. Here T_1 is the transformation matrix from the planning CT image to the RCS, T_2 is the transformation matrix from CBCT image to the RCS and T_3 is the transformation matrix from the RCS of the target image to the RCS of the reference image.

$$T_1 = \begin{bmatrix} X_x\Delta i & Y_x\Delta j & 0 & S_x \\ X_y\Delta i & Y_y\Delta j & 0 & S_y \\ X_z\Delta i & Y_z\Delta j & 0 & S_z \\ 0 & 0 & 0 & 1 \end{bmatrix} \tag{4.1}$$

where S_{xyz} are the three values of the Image Position Patient (DICOM tag) which indicates the location from the origin of the RCS in mm. X_{xyz} are the first three values of the Image Orientation Patient (DICOM tag) and Y_{xyz} are the last three values of the Image Orientation Patient (DICOM tag). Δi and Δj are the pixel size which can be extracted from Pixel Spacing (DICOM tag). Image Position Patient, Image Orientation Patient and Pixel Spacing are medical information which can be read directly from the DICOM images.

After reading T_3 from a RT registration file generated by the radiographers, the transformation matrix T which represents the gold standard rigid registration can be calculated using Equation 4.2.

$$T = T_1^{-1} T_3 T_2 \tag{4.2}$$

4.5.2 Results and discussion

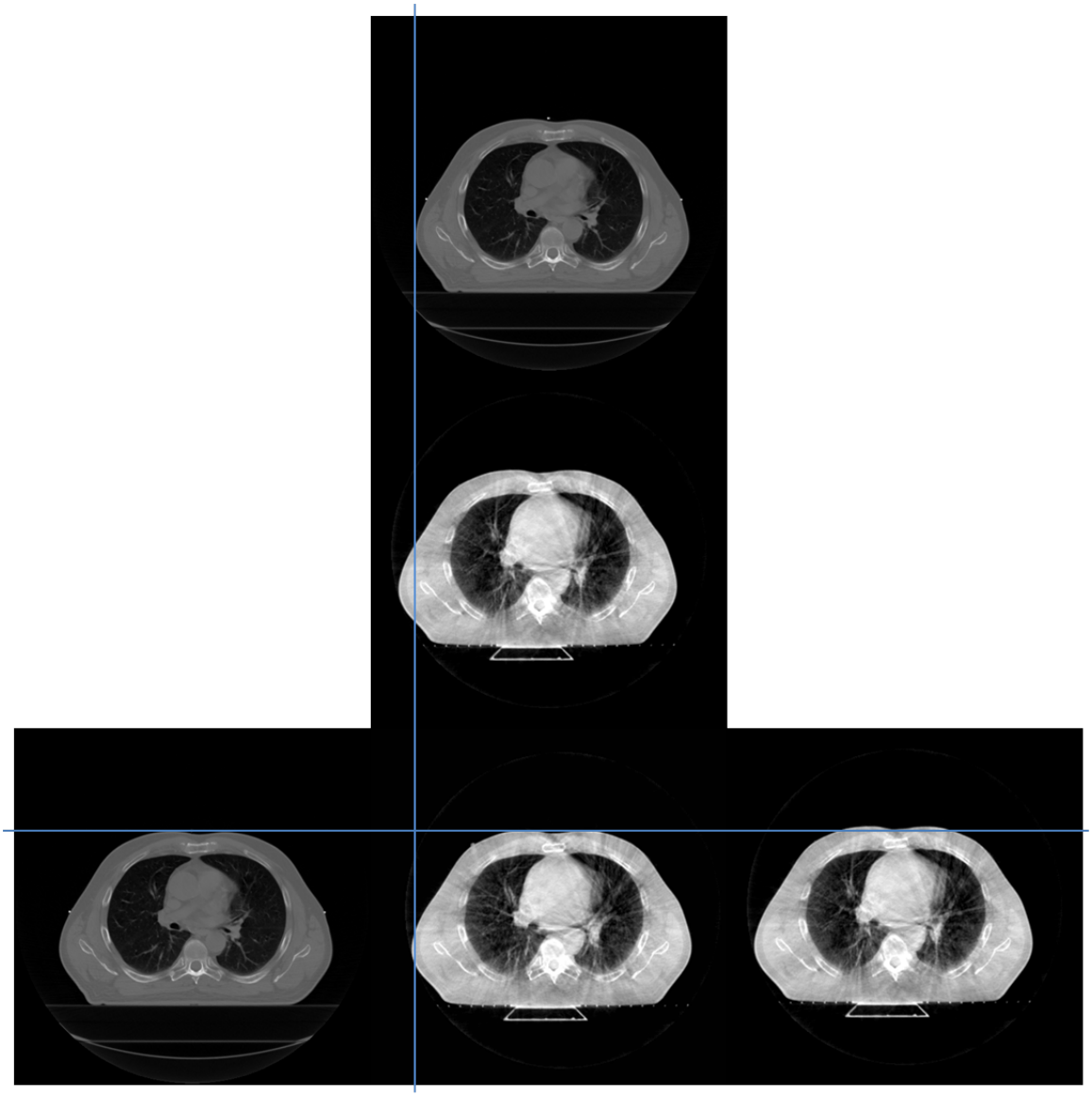

Figure 4.11: Top: the original reference image. Middle: the resized CBCT image (512×512) where bilinear interpolation was used. Bottom left: the original reference image. Bottom middle: the registered CBCT image (512×512) Bottom right: the resized CBCT image. The blue lines are used to illustrate the translation.

Figure 4.3 gives an example of the CBCT data used to test the rigid registration algorithm in which the 512×512 planning CT image from patient 5 was used as the reference image and the 384×384 CBCT image from the 10^{th} fraction of the same patient was used as the target image. CBCT images of this case before and after registration are shown in Figure 4.11. The medical images used in RT usually have the same orientation because they are acquired from patients laid on a flat couch which makes the orientation of patients relatively stable between different

time points. As a result, rotation parameters of the rigid registration defined by radiographers or generated by the presented algorithm were both 0 for CBCT data sets.

Before applying the registration method, the CBCT image was resized to have the same pixel size as the reference image (planning CT) using the bilinear interpolation method presented in Section 3.2.1 . In Figure 4.11, the reference image is shown at the top row and bottom left, the resized CBCT image is shown in the middle row and bottom right and the registered CBCT image is shown in bottom middle. Comparing images vertically in the middle column, the blue line illustrates the reference left boundary of the patient body. It can be observed clearly that the resized target image has much more volume outside the boundary than the registered target image. Similarly, comparing images in the bottom row horizontally, the blue line illustrates the reference top boundary of the patient body and an improvement can be observed from the registration process.

The performance of this method for registering CBCT and CT images was assessed by using the transformation matrix calculated from manual registration data, which was introduced in the previous subsection. The registration method was tested on both 2D (slice by slice) and 3D data. The relative errors of the translation parameters (no orientation difference between them) are shown in Figure 4.12-4.15 (patient 1-5) and Figure 4.16 (x, y, z) respectively. In the 2D case, more than 90% of cases have a relative error of less than 5%. This means that the rigid registration method resulted in a translation of 19-21 pixels of the target image automatically in x direction if the manual registration process moved the target image by 20 pixels along x direction. The average calculated over relative errors of all the cases was 2.41% and 2.64% for x and y direction. In the 3D case, the average of relative errors was 4.05%, 3.87% and 3.78% for x, y and z direction respectively. There are three possible reasons for the errors generated:
1. The accuracy of automatically generated registration parameters was limited by a step size which was set to be 0.25 pixels in this case but manually generated parameters have no such limit. As a result, irreversible errors exist between them, which could be reduced by decreasing the step size in the future.
2. There may be slight shape variations between the reference and target image because they were acquired at different time points even though they are from the same modality.
3. There may still be errors in the manual registration process although the manually generated parameters were treated as the gold standard. Considering that an error in registration is unavoidable in practice, the accuracy of the method presented is acceptable in clinical.

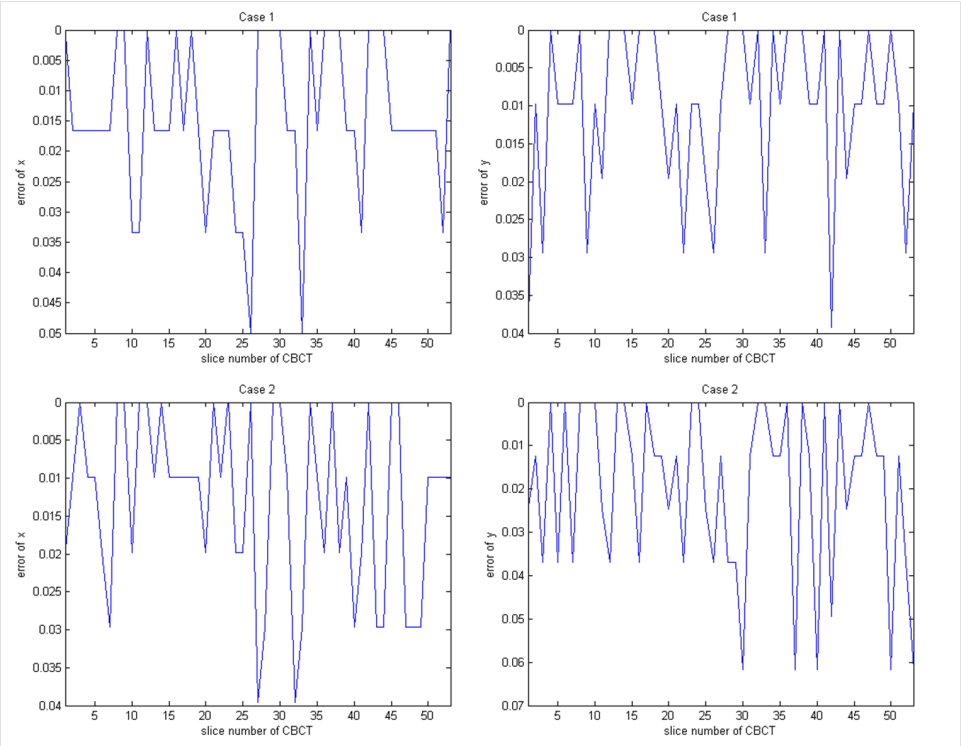

Figure 4.12: 2D relative errors (x and y directions) for case 1 and 2.

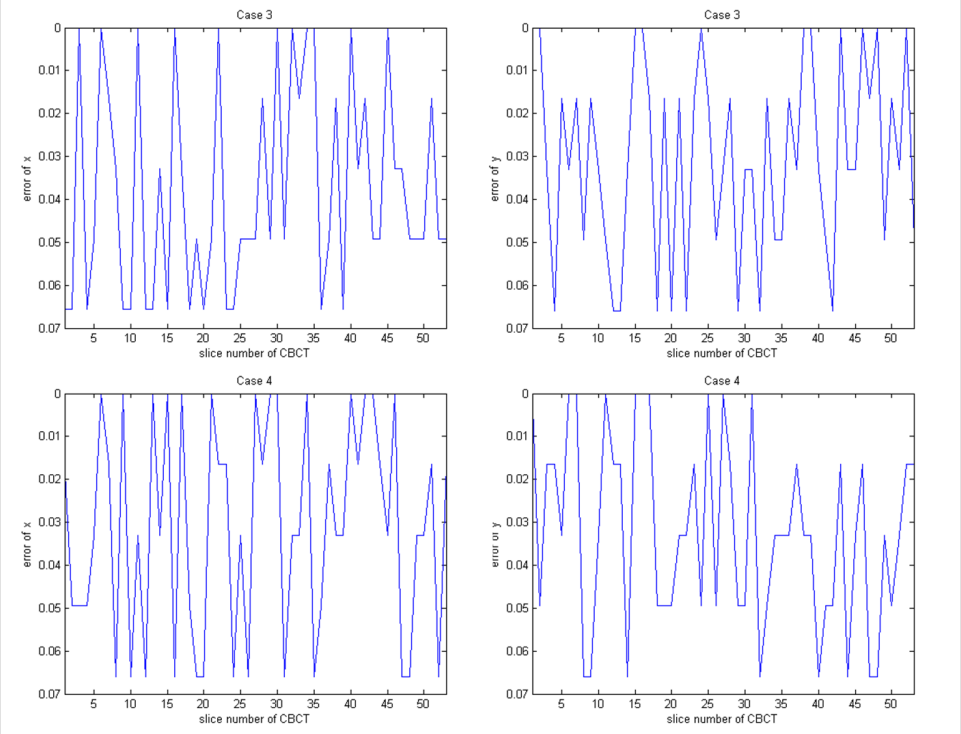

Figure 4.13: 2D relative errors (x and y directions) for case 3 and 4.

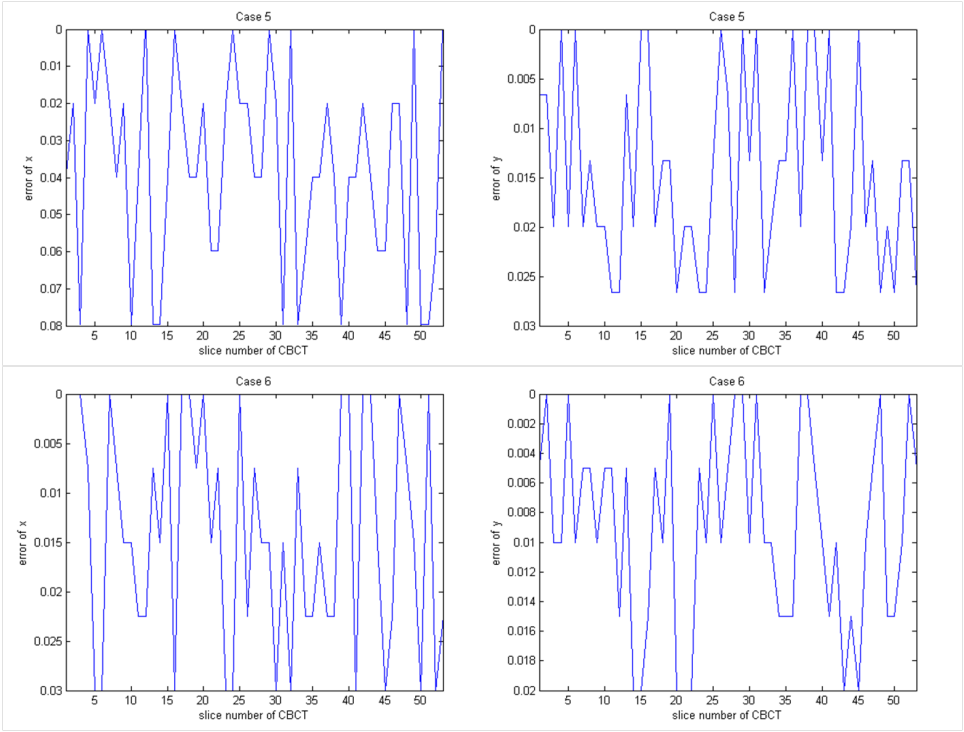

Figure 4.14: 2D relative errors (x and y directions) for case 5 and 6.

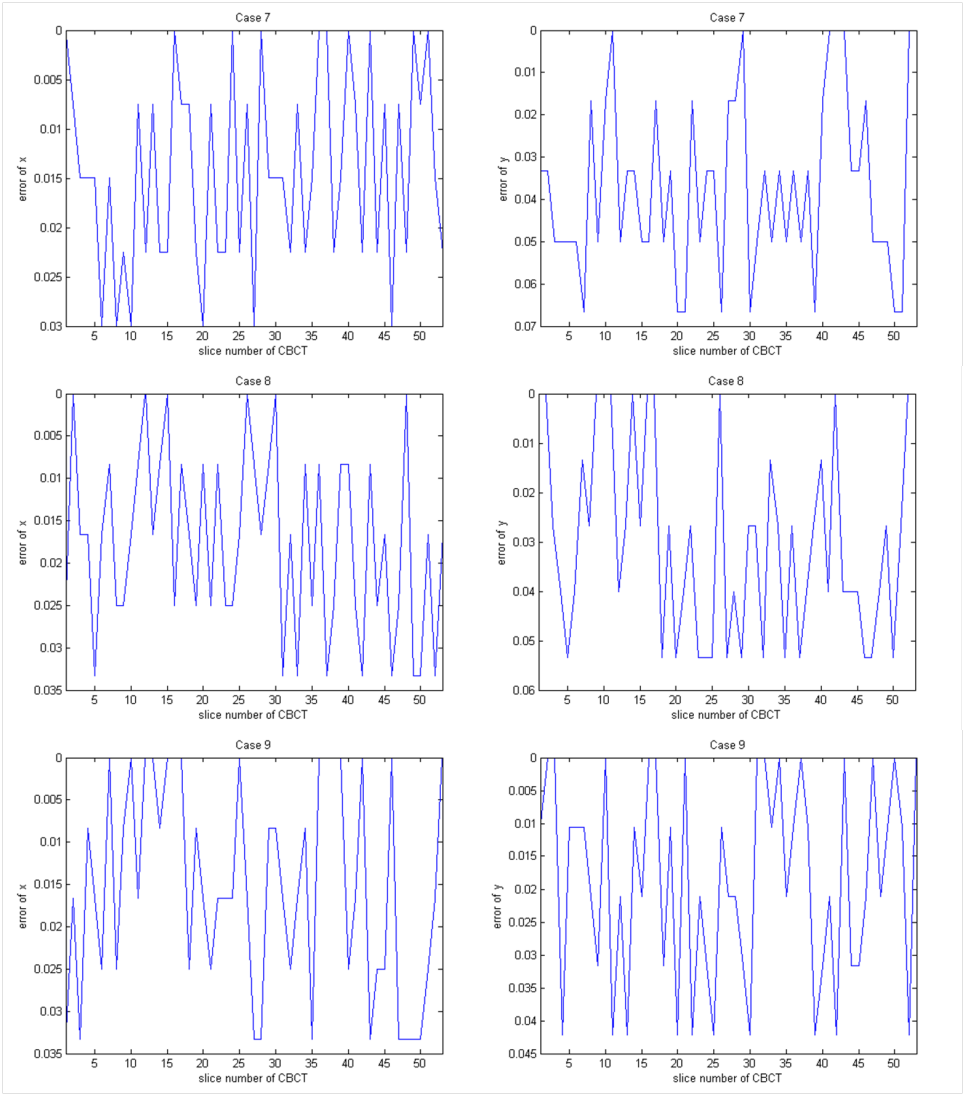

Figure 4.15: 2D relative errors (x and y directions) for case 7, 8 and 9.

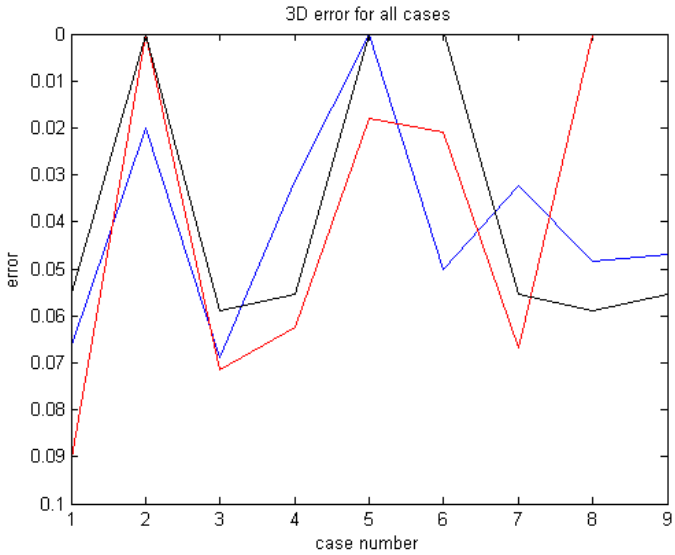

Figure 4.16: 3D relative errors in x, y and z directions (blue, red and black respectively) for all 9 cases.

4.6 Performance on EPID data

In RT, planning CT images can be reconstructed into DRR images which are a direct representation of planned treatment position. The registration between the DRR and EPID images which provide a view of the patient at treatment time is always used to ensure that the patient is positioned in the correct location for treatment. Figure 4.17 shows the example of registration between them.

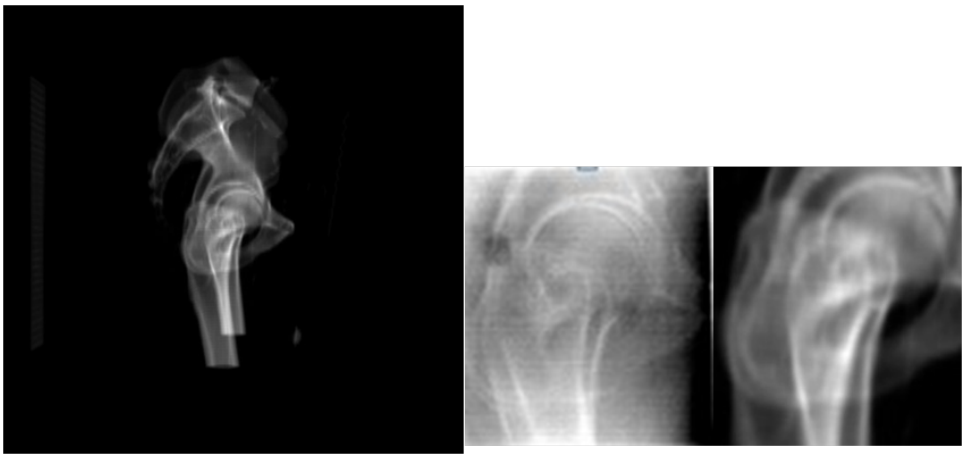

Figure 4.17: Left: the 512×512 DRR reference image from a prostate cancer patient. Middle:the 244×244 EPID target image. Right: the 244×244 registered image (showing the part of interest).

4.7 Conclusion

In this chapter, the pre-segmentation method for PET images was tested on PET images from lung cancer patients. It has demonstrated that this method can provide clear and single segmented tumor volume on PET images based on the SUV values of corresponding data sets.

The SIFT-based rigid registration method presented in Section 3.3 was tested on both phantom data sets and CBCT data sets from lung cancer patients. This method was proved to be capable to find the rigid (rotation and translation) registration parameters between images from different modalities and is much faster than conventional MI-based algorithms. CBCT images which have poor image quality and heavy noise were used to test how this algorithm works between images from the same modality. The transformation matrix which can be calculated from the manually registration parameters generated by radiographers was used to provide an objective assessment for this method. Both 2D and 3D method were applied on the CBCT data sets and the average of relative errors recorded for all the cases was under 5%. This has proved that the SIFT-based rigid registration method has the potential ability to provide accurate and automatic registration during the time of treatment.

Chapter 5

Performance of non-rigid registration method

5.1 Introduction

Non-rigid registration methods are commonly used to find the distortions between images from different modalities such as between CT and MRI/PET. Non-rigid warping usually leads to interpolation problems that affect the result. The non-rigid registration approach developed here depends on a cubic B-spline interpolation method, which can generate smooth distortions. There are several control points in the B-spline approach distributed as a grid over the whole image and distortions can be generated by varying the positions of them. Optimization algorithms such as simulated annealing and L-BFGS are then applied to find the minimum of a similarity function that indicates the best control grid positions. Both SIFT and Gabor filters can provide stable features which are invariant to illumination, rotation, scale, and translation to calculate the similarity function. Manually identified distinctive regions, which may contain biological and pathological information, are then used in the non-rigid method and the MI between them are used to evaluate the similarity.

In this chapter the non-rigid registration method introduced in Section 3.4 was tested on various data sets which are summarized in Section 5.2. In Section 5.3, results of applying this approach on manually warped test images, including histological images of prostate cancer patients, are presented. Here, the Euler distance of manually defined corresponding feature points was used and an improvement that the mean distance was remarkable reduced after registration was observed. Optimization using the L-BFGS method was also carried out. Section 5.4 presents results of applying the non-rigid approach between RT planning CT and diagnostic MRI images of prostate cancer patients where in all cases prostate contours on both CT and MRI images and focal regions within the prostate on MRI images were generated by an oncologist. It is shown that conventional rigid registration approaches are not sufficient to register these data because the registered focal regions may be outside the prostate on CT images. To find the distortions between them, Gabor filters were used to extract feature points on prostate contours and find the correspondence between them. Registration performance was assessed by the Dice coefficient between prostate contours and registered focal contours. An assessment by an oncologist on

the efficiency of the contour produced is also presented.

5.2 Test data

Two test data sets were used to test the B-spline based non-rigid registration algorithm. Test data set 1 contains manually warped images including simple logical images (two gray levels: black and white), histological and MRI images of the prostate. The performance was assessed by using the SSD between corresponding feature points on the reference and target image. Test data set 2 includes 16 cases of prostate cancer patients. Diagnostic MRI images and planning CT images were available for every case in this data set (Details of planning CT images are shown in Table 5.1 and details of diagnostic MRI images are shown in Table 5.2). Clinical contours including OARs on both MRI and CT images and focal regions on MRI images were provided by a clinician as shown in Figure 5.1 (contrast in this figure was adjusted to make the interested region clearer and may looks different on screen than printed).

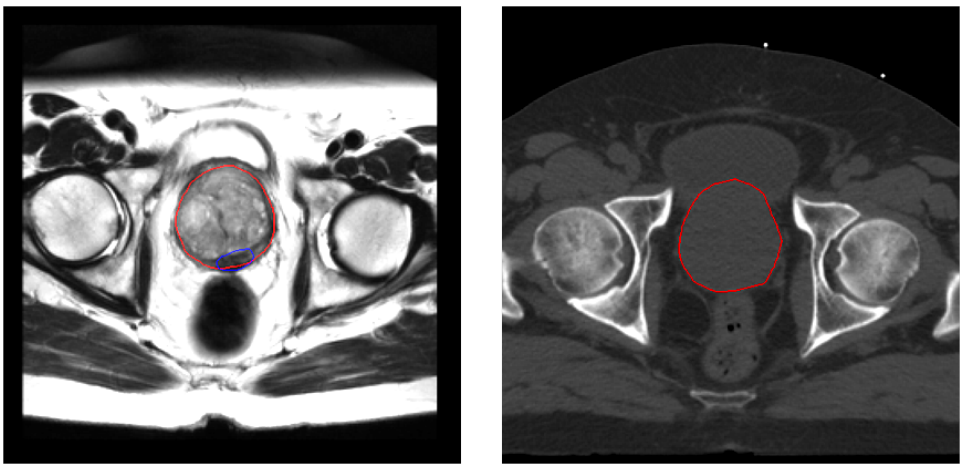

Figure 5.1: Left: Pre-processed diagnostic MRI image (512×512) with the prostate contour (red) and the focal disease contour (blue) generated by a clinician. Right: Planning CT image (512×512) with the prostate contour (red).

In test data set 2, prostate contours on two different image modalities can be used as prior knowledge and therefore the corresponding feature points on the reference and target image can be identified using the Gabor filter based method introduced in Section 3.4.2. Under the assumption that focal regions on MRI and CT images have the same distortion as the prostate, the distortion map identified by prostate feature points was then applied to focal contours. Non-rigidly registered focal contours on the planning CT images were assessed by a clinician.

The other important point is that both test data sets used in this chapter were pre-processed to have the same resolution and geometry. Also, the SIFT-MI based rigid registration method was

Case Number	Pixel Size (mm)	Slice Thickness (mm)	Slice Number
Case 1	1.0371 ×1.0371	4.5	127
Case 2	0.9648 ×0.9648	3	74
Case 4	0.9258 ×0.9258	4	118
Case 5	1.252 ×1.252	4	89
Case 6	0.9551 ×0.9551	4	124
Case 7	1.0332 ×1.0332	4	106
Case 8	0.9258 ×0.9258	3.5	102
Case 9	0.9082 ×0.9082	3.5	97
Case 11	1.1875 ×1.1875	4	104
Case 12	0.9375 × 0.9375	4	130
Case 13	0.9395 ×0.9395	4	106
Case 14	0.9375 ×0.9375	3	119
Case 15	0.8398 ×0.8398	3	122
Case 16	0.998 ×0.998	3.5	109
Case 18	0.9258 ×0.9258	3	103

Table 5.1: The details of the CT data for the 16 prostate cancer patients used in this study. The image size for all CT images was 512×512.

Case Number	Image Size	Pixel Size (mm)	Slice Thickness (mm)
Case 1	512×512	0.4688 ×0.4688	4.5
Case 2	256×256	0.7031 ×0.7031	3
Case 4	448×448	0.558 ×0.558	4
Case 5	448×448	0.558 ×0.558	4
Case 6	512×512	0.4688 ×0.4688	4
Case 7	512×512	0.4492 ×0.4492	4
Case 8	512×512	0.4297 ×0.4297	3.5
Case 9	512×512	0.3906 ×0.3906	3.5
Case 11	512×512	0.4297 ×0.4297	4
Case 12	512×512	0.4102 ×0.4102	4
Case 13	512×512	0.4688 ×0.4688	4
Case 14	256×256	0.7031 ×0.7031	3
Case 15	256×256	0.7031 ×0.7031	3
Case 16	512×512	0.3906 ×0.3906	3.5
Case 18	320×320	0.625 ×0.625 mm	3

Table 5.2: The details of the MRI data for 16 prostate cancer patients (part 1).

applied before the non-rigid method as a pre-processing step to make sure that the reference and target image had acceptable rigid differences.

5.3 Performance on manually warped test images

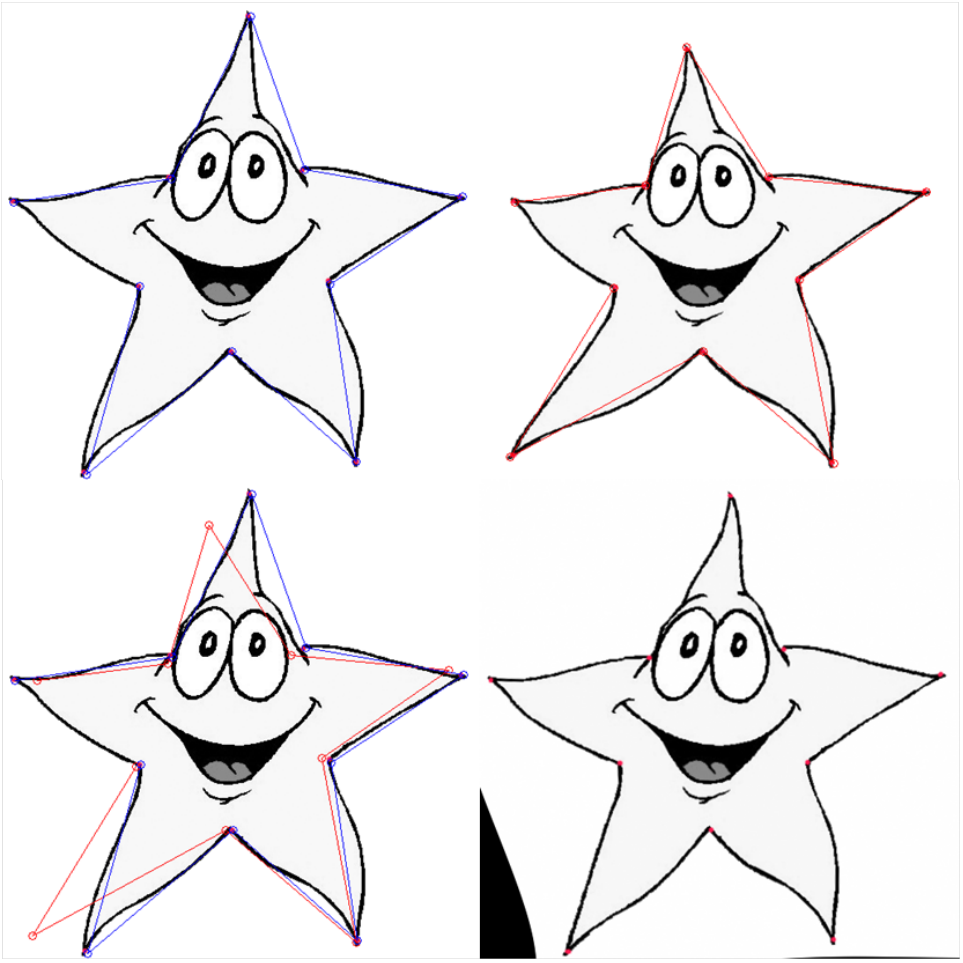

Figure 5.2: The reference image with selected feature points (top left), the target image with selected feature points (top right), the reference image with feature points of both images (bottom left), the registered target image (bottom right).

Figure 5.2 shows the star images with 10 feature points selected manually for each image. In Figure 5.3, control points were initialized to be uniformly distributed over the image, after finding the distortions by optimizing the SSD of feature points, the distortion field shows how the image was warped from the target to the reference image.

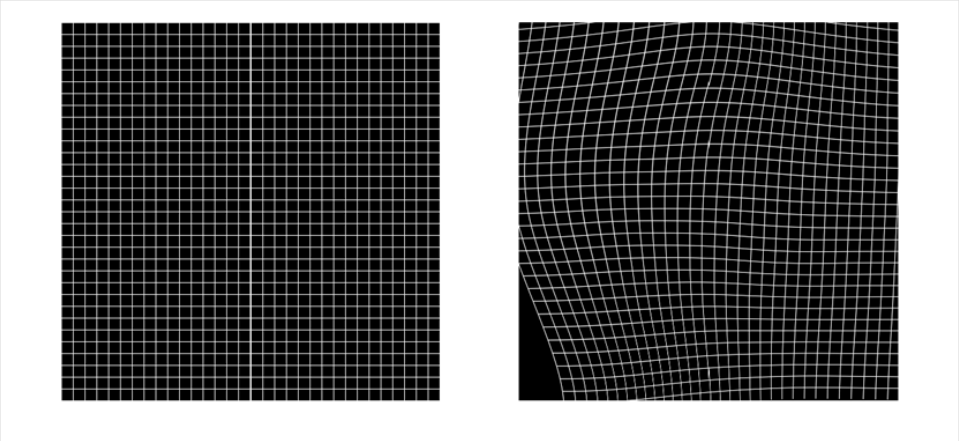

Figure 5.3: Initial 32×32 evenly spaced control points (left), the distortion field (control grid) after registration of the target images (right).

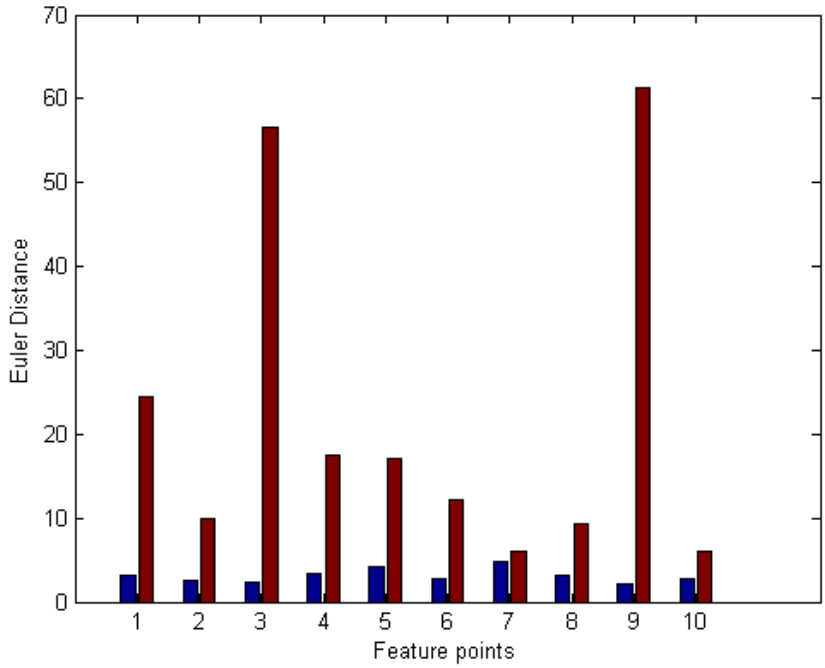

Figure 5.4: The Euler distance of 10 feature points before (red) and after (blue) registration.

Figure 5.4 shows the Euler distance of feature points between the reference and target image. The overall mean distance before and after registration are 29.03 and 2.55 respectively. The mean distance was reduced by 91.2% after registration and Figure 5.5 shows the convergence of optimization process which was simulated annealing.

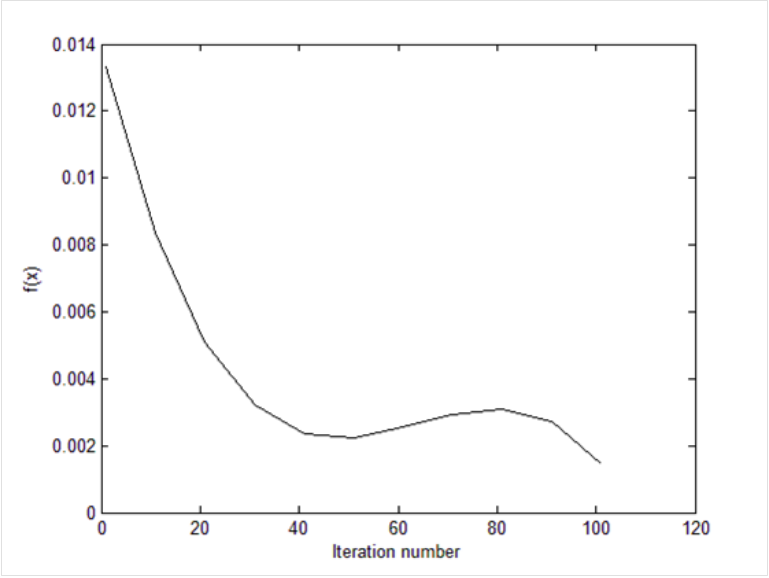

Figure 5.5: The optimization process. Simulated annealing was used to avoid the optimization being trapped by local minimum which can be seen in this figure: the line reached a local minimum and continued to optimize.

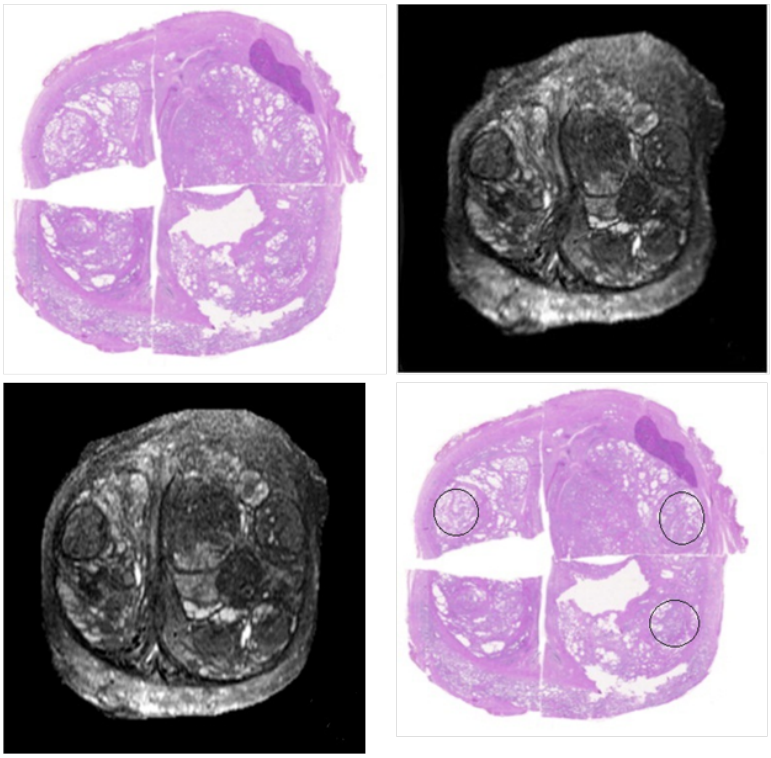

Figure 5.6: Histological test images (top left), test MRI image (top right), registered image (bottom left), the selected regions (bottom right).

As Figure 5.6 shows, practical images including diagnostic MRI (512×512) and histological

images (512×512) which have much more distortion and noise than the simple star images shown in Figure 5.2 were used to test the non-rigid registration algorithm. The original MRI image was warped manually. The non-rigid registration algorithm was applied to restore the MRI image based on the histological image using manually defined features extracted on the three distinctive regions shown in Figure 5.6. 8 feature points on/within the contour of the prostate were also extracted for registration.

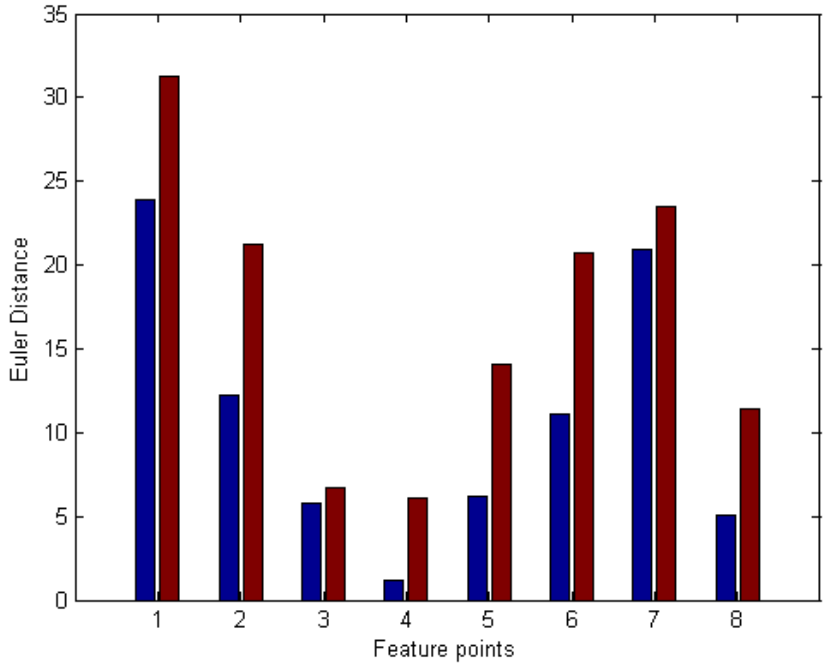

Figure 5.7: The Euler distance of 8 feature points before (red) and after (blue) registration.

The overall mean distance of these feature points before and after registration are 18.83 and 13.08 respectively as shown in Figure 5.7 where the mean distance was reduced by 30.5%.

5.4 Performance on prostate data

It is widely reported that in a third of prostate cancer patients the significant cancer cells are confined to a single focus [27]. As a result, accurately identifying this focus and treating it with a high dose, and the remainder of the prostate to a reduced dose would help preserve prostate function. However, it is very difficult to determine the location of the focus using CT images. The focus is best identified on MRI images, however, CT images are necessary for RT planning. Here, the non-rigid registration method presented in Section 3.4 was used to map the focal contour from MRI to CT.

Case Number	T_x	T_y	T_z	Direction
Case 1	6	14	51	LP
Case 2	6	6	20	LP
Case 4	25	12	38	LA
Case 5	37	4	1	LP
Case 6	5	5	53	LP
Case 7	5	3	51	LA
Case 8	15	17	32	LP
Case 9	20	25	34	RA
Case 11	16	2	27	RA
Case 12	5	12	58	RP
Case 13	17	12	44	RA
Case 14	29	7	57	LP
Case 15	26	7	48	LP
Case 16	29	25	35	LP
Case 18	24	2	47	LA

Table 5.3: The rigid registration result (parameters) where T_x, T_y and T_z represent the translation parameters in x, y and z directions, the rotation parameters are all 0. LP, LA, RP and RA represent left posterior, left anterior, right posterior and right anterior which are the moving directions of MRI images.

The MRI data set for every case was re-sampled and re-sized to have the same slice thickness, pixel size and image size as the CT data set. Also, the original prostate and focal contours defined on MRI images were pre-processed using the method presented in Section 3.2.2. The rigid registration method presented in Section 3.3 was applied before the non-rigid step as a pre-processing method to limit the spatial difference between different data sets. The rigid registration parameters for all 15 cases are shown in Table 5.3.

An example from case 6 is shown in Figure 5.8 in which the rigidly registered focal contour is partly outside the prostate on the CT image while the original focal contour on the MRI image is inside the prostate. This is because the rigid registration method only found the match between SIFT feature points which usually have notable gradient values (eg. bones). However, the pixels around soft tissues which are relatively far away from bones were not considered. Also the variation in the shape of soft tissues (eg. prostate) cannot be identified by this method. This demonstrates that the rigid method is not good enough for mapping focal contours between images from different modalities. Because MRI and CT images were acquired at different time points and cohort neo-adjuvant hormones were given between MR and CT which shrunk the prostate, the shapes of the prostate and focal region were likely to be different. As a result, the non-rigid registration method was applied to find the distortions and soft tissue variations between CT and MRI images under the assumption that changes of focal regions between CT and MRI images were the same as changes of corresponding prostates. To find the distortion between them, the corresponding Gabor feature points on the reference and target images were

selected from clinical prostate contours. As this method is designed for focal prostate cancer cases where the tumor volume was larger than the prostate volume (case 3, 10 and 17) were ignored.

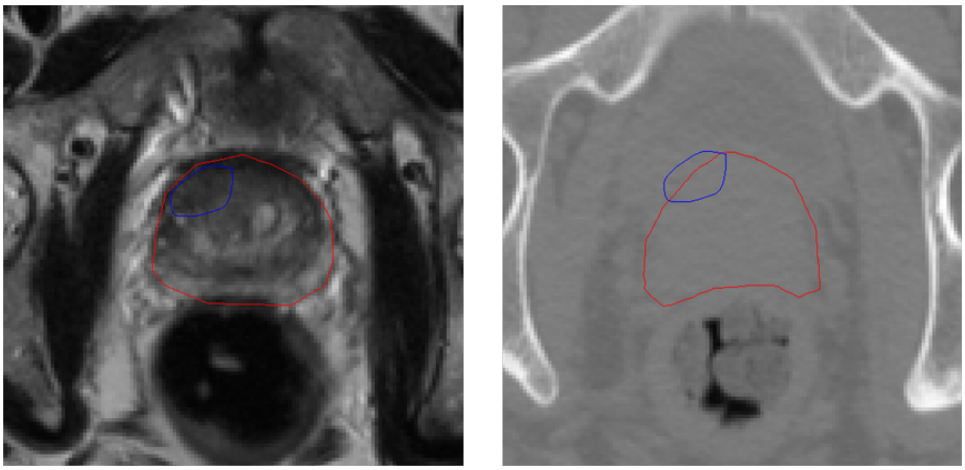

Figure 5.8: Left: The pre-processed T2-weighted MRI image with the prostate contour (red) and the focal contour (blue). Right: The original planning CT image with the prostate contour (red) and the rigidly registered focal contour (blue).

To show the improvement from rigidly registered results by the non-rigid registration method, it was tested on the same slice shown in Figure 5.8. As shown in Figure 5.9, the non-rigidly registered focal contour is completely inside the prostate on the CT image. The shape of the original focal contour was also changed by the non-rigid method to fit the prostate shape.

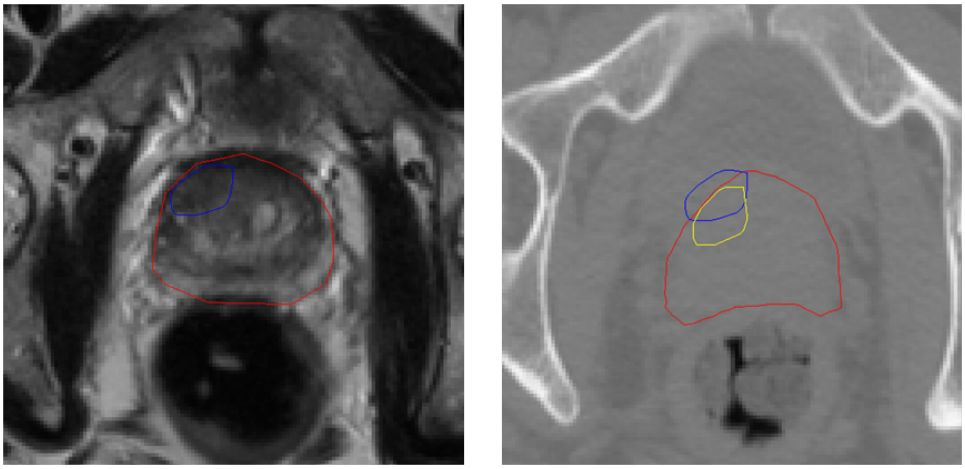

Figure 5.9: Left: The pre-processed T2-weighted MRI image with the prostate contour (red) and the focal contour (blue). Right: The original planning CT image with the prostate contour (red), the rigidly registered focal contour (blue) and the non-rigidly registered focal contour (yellow).

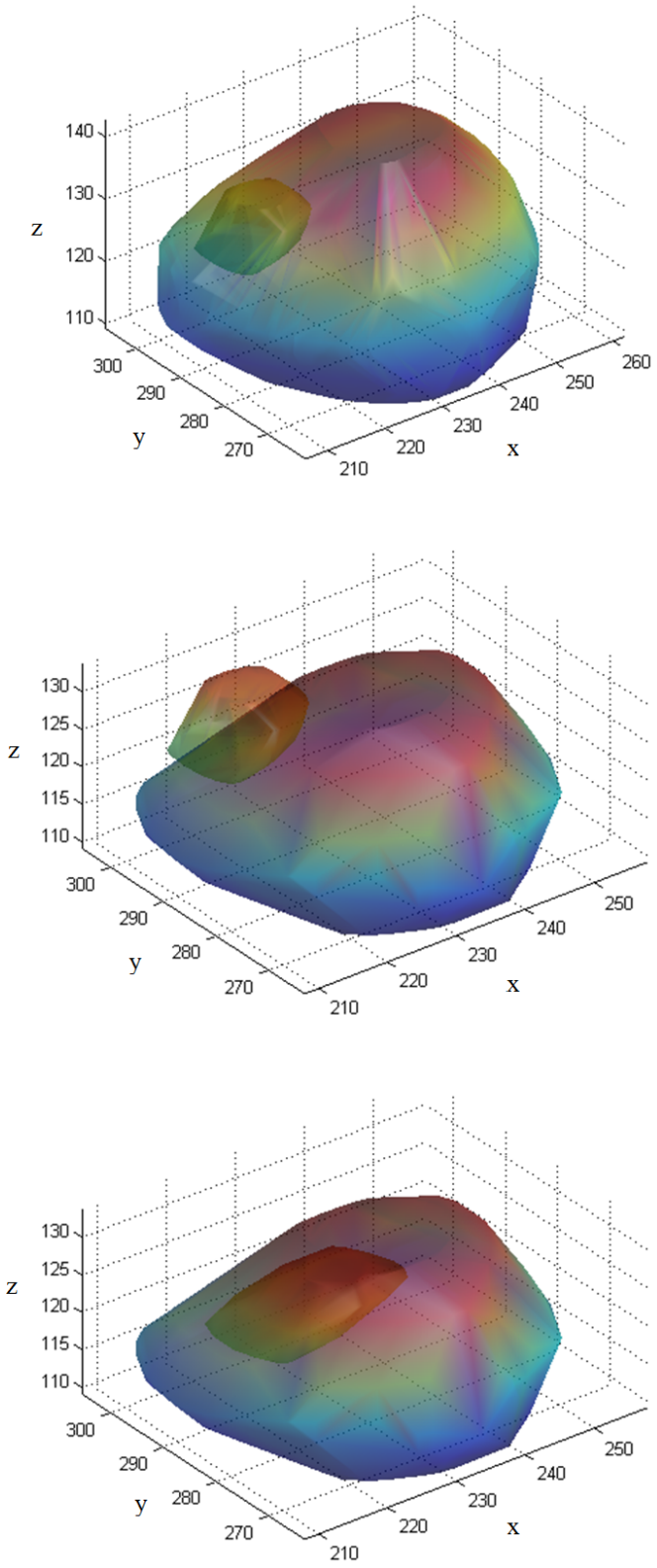

Figure 5.10: Top: The reconstructed prostate and focal shape on the MRI data set. Middle: The reconstructed prostate and rigidly registered focal shape on the CT data set. Bottom: The reconstructed prostate and non-rigidly registered focal shape on the CT data set

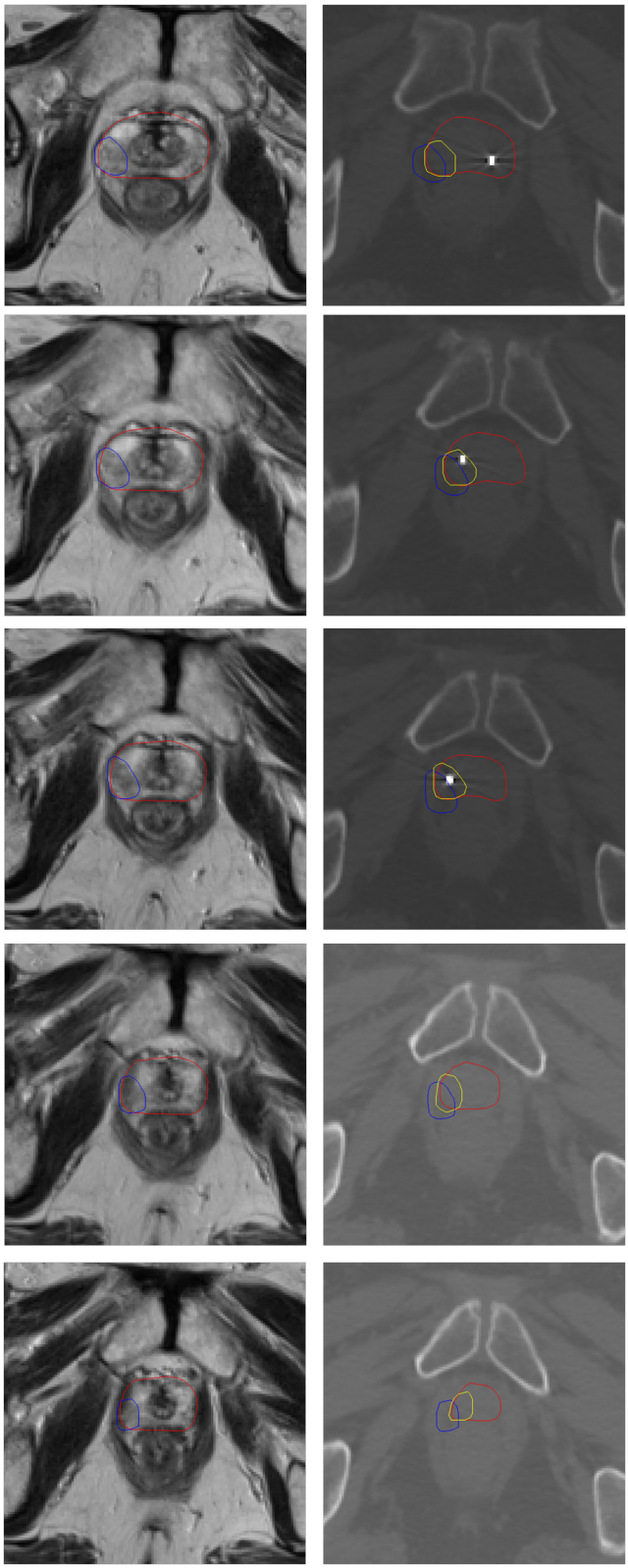

Figure 5.11: The result of application of the non-rigid registration algorithm to case 11 which has 5 slices containing tumor volume (slice 76-80 from top to bottom). On all of the images, prostate contours are shown in red, rigidly registered contours are shown in blue and non-rigidly registered contours are shown in yellow.

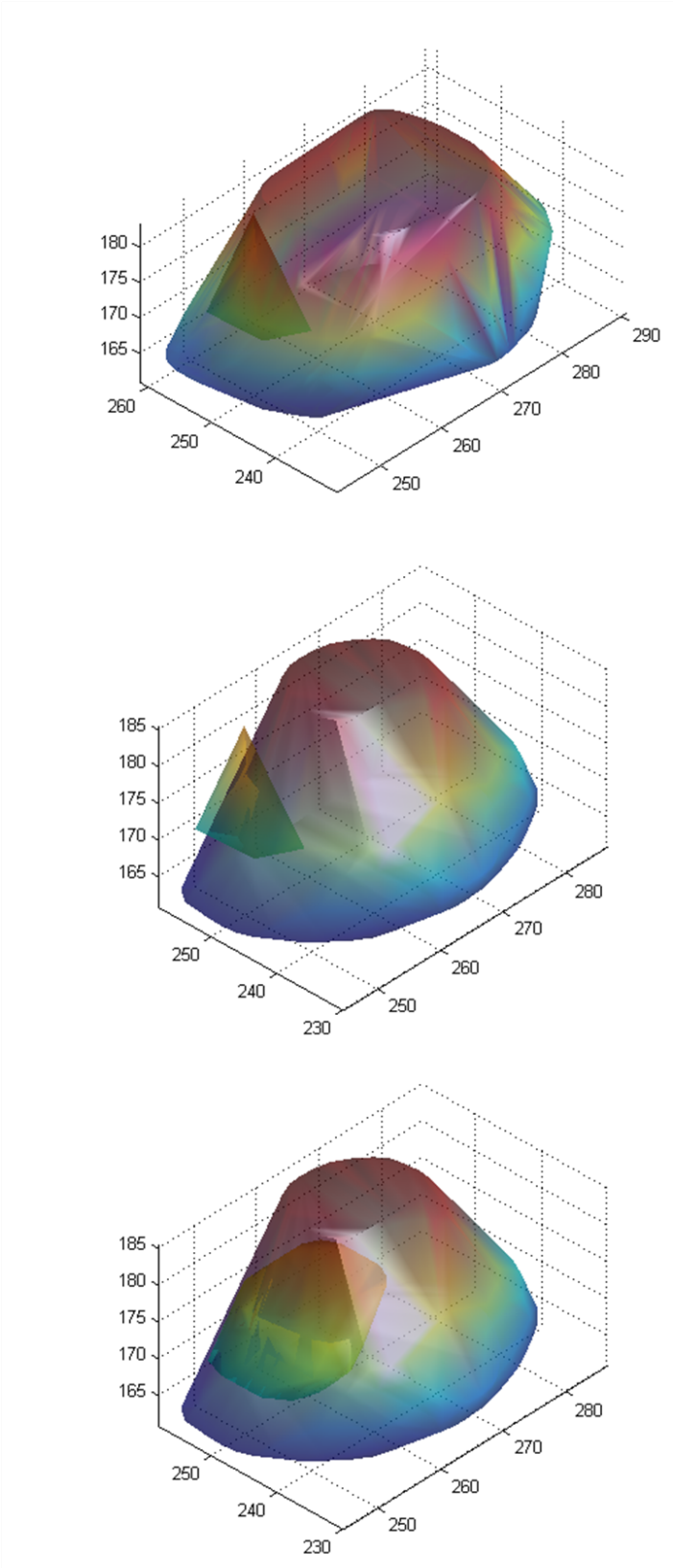

Figure 5.12: Top: The reconstructed prostate and focal shape on the MRI data set. Middle: The reconstructed prostate and rigidly registered focal shape on the CT data set. Bottom: The reconstructed prostate and non-rigidly registered focal shape on the CT data set

In this case, the first criteria (SSD) of the presented non-rigid registration method contributed in finding the variation between prostates on MRI and CT images and the second criteria contributed in limiting the spatial error of the focal shape and correcting the focal position. A 3D reconstruction example is shown in Figure 5.10 where the shape variation of the prostate and focal region is compared.

To compare the shape variation of the prostate and focal region before and after registration, the reconstructed 3D images in Figure 5.10 are shown at the same point of view using the same scale. The top image shows the original prostate and focal shape on the MRI data set, the middle image shows the rigidly registered focal shape and the prostate shape on the CT data set and the bottom image shows the non-rigidly registered focal shape and prostate shape on the CT data set. Comparing the top and middle images, it is clear that the focal shape has not changed when the rigid method is applied, which only changed the position of the focal region. Also, the shape variation of the prostate between CT and MRI images resulted in the focal region being placed partly outside the prostate based on the translation parameters shown in Table 5.3. This is because, by using these rigid parameters, the SIFT feature points which are usually selected around the regions of bones were best matched but the prostate was not supposed to have the same rigid position variation and it is unlikely to change its shape rigidly. Comparing the middle and bottom image, because they were both reconstructed from CT data set, the prostate shape is the same and it can be easily observed that the non-rigid method varied the shape of the focal region. The non-rigid method attempted to fit the original focal region to the target prostate by varying its shape and position based on the Gabor features and distinctive regions. The bottom image shows that after registration, the focal shape is placed almost completely inside the prostate based on the shape variation of prostates between CT and MRI images.

To find how the proposed method works on a series of 2D images, as shown in Figure 5.11, a range of rigidly and non-rigidly registered results from case 11 are shown. There are 5 MRI slices (slice 76-80) containing the focal tumor volume in this case with the reconstructed 3D shape of the prostate and focal region shown in Figure 5.12. In every slice the rigid registration method translated the focal region to a position partly outside the prostate on the CT image while the original focal region was almost completely inside the prostate on the MRI image. The rigid method treated the whole CT and MRI data sets as 3D volumes and therefore gave every slice the same translation parameters. As a result, rigidly registered focal contours were continuously placed at a wrong position in the prostate (Figure 5.11). Here, the non-rigid method was used to find the 2D distortion and generate a correction for every slice. Non-rigidly registered focal contours show clear improvements from rigidly registered results. Also, this demonstrates that for a range of 2D images, the non-rigid method can find different distortion fields between prostates on different CT and MRI slices and apply them on rigidly registered focal contours to generate new focal segmentations on CT images.

Also, focal regions for case 6 (Figure 5.9) and 11 (Figure 5.11) were at different positions within the prostate. This suggests that both rigid and non-rigid registration methods are invariant to focal position variations and may be generally applied to track the shape variation of the target organ. Theoretically, for the rigid method, feature points were selected around pixels with notable gradient values which were unlikely to be inside soft tissues. As a result, the shape and position variations of the prostate and focal region can hardly effect the rigid registration result. For the non-rigid registration method, distinctive regions were also selected from bones. Therefore, criteria 2 would not be changed by variations of the focal region. For criteria 1, depending on the size and position of the focal region, feature points located nearer to the focal contour can contribute more to the non-rigid result. However, as long as there are enough corresponding feature points near to the focal region on the prostate contour, the non-rigid registration method can work correctly. As an advantage of image processing methods, the rigid and non-rigid registration method worked only based on image information extracted directly from medical data. As a result, clinical information such as age and weight of patients and pathological information such as prostate volume and focal position are unlikely to perturb the result. However, further testing and a much larger data set is required.

To evaluate the performance of the non-rigid registration result objectively, four ratios (R1-R4), calculated form Equation 5.1, were used. These were defined based on the assumption that focal lesions were unlikely to be outside the prostate.

$$\begin{aligned} R1 &= V_{In\_1}/V_{MRI\_Focal} \\ R2 &= V_{In\_2}/V_{CT\_Original\_Focal} \\ R3 &= V_{In\_3}/V_{CT\_Rigid\_Focal} \\ R4 &= V_{In\_4}/V_{CT\_Nrigid\_Focal} \end{aligned} \tag{5.1}$$

where V_{MRI_Focal} represents the original focal volume on MRI images, $V_{CT\_Original\_Focal}$ represents the original focal volume on CT images, $V_{CT\_Rigid\_Focal}$ represents the rigidly registered focal volume on CT images, $V_{CT\_Nrigid\_Focal}$ represents the non-rigidly registered focal volume on CT images. V_{In_1}, V_{In_2}, V_{In_3} and V_{In_4} are the overlap volume between V_{MRI_Focal}, $V_{CT\_Original\_Focal}$, $V_{CT\_Rigid\_Focal}$, $V_{CT\_Nrigid\_Focal}$ and their corresponding prostate respectively. Therefore, R1-R4 represent the ratios of the focal volume inside the prostate volume. R1-R4 for all 15 test cases are shown in Table 5.4.

Based on Equation 5.1, R1 illustrates the original inside tumor volume of the prostate comparing with the GTV. 12 cases of all the 15 test cases have R1 larger than 90% and the overall mean value of R1 reaches 94.54%. This is because the tumor volume of focal prostate cancer is unlikely to be located outside the prostate. However, depending on the position and size of the focal region, the tumor volume can still be slightly outside the prostate to varying degrees. Basically, R2 provides the overlap rate between the original focal contour and the prostate contour on CT images. The overall mean value of R2 is only 39.72% which means that more

Case Number	R1	R2	R3	R4
Case 1	89.13%	16.55%	53.26%	88.43%
Case 2	98.79%	76.35%	86.24%	95.01%
Case 4	100%	54.26%	80.45%	95.69%
Case 5	96.07%	34.35%	93.22%	97.53%
Case 6	99.60%	80.50%	82.84%	99.47%
Case 7	76.41%	36.55%	66.32%	69.57%
Case 8	100%	13.67%	49.95%	94.62%
Case 9	94.37%	22.50%	51.28%	89.79%
Case 11	92.11%	19.52%	48.27%	91.66%
Case 12	83.20%	40.15%	77.64%	81.19%
Case 13	98.31%	32.60%	59.73%	89.26%
Case 14	90.07%	60.25%	78.36%	86.73%
Case 15	100%	79.24%	100%	100%
Case 16	100%	0%	39.36%	100%
Case 18	100%	29.25%	44.49%	98.67%

Table 5.4: R1-R4 of the 15 test cases used in this study which represent the ratios of the focal volume inside the prostate volume.

than 60% of the treating area would be outside the prostate if the original focal contour was used for RT planning directly. In practice, a large margin around the GTV is used when the tumor volume cannot be identified accurately to make sure all the tumor volume is treated and may result in adverse effects on normal tissues. To improve this, the rigid registration method was applied to limit the spatial error and was evaluated by R3. As shown in Table 5.4, the overall mean value of R3 is 67.43% and R3 is always larger than R2 for every case. The inside focal volume was increased by 27.71% after rigid registration. This is because the focal volume was translated to a relatively correct position based on the match of SIFT feature points which were well defined around bones. The non-rigid registration result was evaluated by R4 which is supposed to gain an improvement from R3 by simulating the distortion between prostates. The overall mean value of R4 is 91.84% and the error between R1 and R4 is only 2.7%. The mean improvement from R3 to R4 is 24.41%. This demonstrates that non-rigid registration method is sensitive to the variation between prostate contours and it can change the focal contours based on this. As shown in Figure 5.13 (R1-R4 for the 15 test cases), the non-rigidly registered focal volume (R4) has the most similar values to the original focal volume on MRI images (R1) comparing with the corresponding prostate.

For most of the test cases, R1 and R4 reached almost 100% but in case 7, numbers for R1 and R4 are only 76.41% and 69.57%. This is because the tumor volume in this case is large and it exceeds the prostate boundary. Although this case cannot be treated as focal prostate cancer, the tumor contour is near enough to the prostate contour. As a result, the approach presented could still find the best rigid match and the variation of the tumor volume between CT and MRI images. R4 of this case was proven to be close to R1 (error: 6.84%) and larger than R2

Case Number	Acceptable	Non-rigid Better Than Rigid
Case 1	Yes	Yes
Case 2	Yes	Yes
Case 4	Yes	Yes
Case 5	Yes	No
Case 6	Yes	Yes
Case 7	-	-
Case 8	Yes	Yes
Case 9	No	Yes
Case 11	Yes	Yes
Case 12	Yes	Yes
Case 13	No	Yes
Case 14	Yes	Yes
Case 15	Yes	Yes
Case 16	Yes	Yes
Case 18	Yes	Yes

Table 5.5: Clinician's opinion on both the rigid and the non-rigid registration result. The clinician focused on two aspects: 1. The non-rigidly registered focal contour on CT images is acceptable for RT planning or not. 2. The non-rigidly registered focal contour is better than the rigidly registered focal contour or not.

(improvement: 33.02%) and R3 (improvement: 3.25%).

The result produced by the non-rigid method was also assessed manually by a clinician and the comments are summarized in Table 5.5. In almost all cases the clinician observed improvements using the rigidly registered focal contour compared to the non-rigidly registered focal contour. Also, non-rigidly registered contours were found to be acceptable for most of the cases except in case 9 and 13. As previously mentioned, the rigid method worked in 3D while the non-rigid method worked in 2D. As a result, the distortion between prostates in z direction cannot be identified during the registration process. For most of the test cases, prostates do not have heavy distortions in z direction. However, in case 9 and 13, prostates were heavily moved along z direction. As a result the original focal contour was mismatched to the wrong CT slice by the rigid method and therefore the non-rigid method cannot find the correct distortion between the reference and target image. In the future a 3D non-rigid registration algorithm, which can find the 3D distortion field, should be used instead of a 2D method to find a solution to this issue.

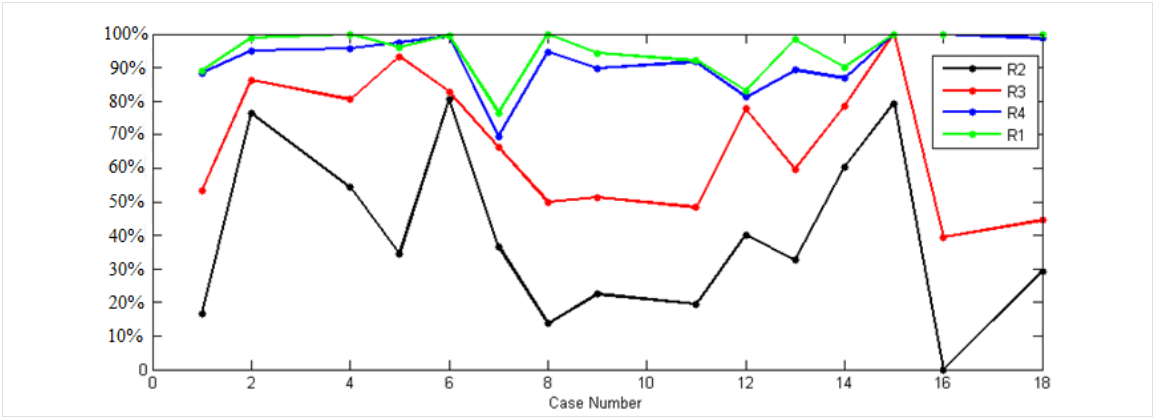

Figure 5.13: R1-R4 shown in green, black, red and blue and the overall mean values of them are 94.54%, 39.72%, 67.43% and 91.84% respectively. In a general point of view, from R2-R4, it is getting more and more similar to R1.

5.5 Conclusion

In this chapter, the non-rigid registration method was applied on manually warped test images and a selection of medical images. This proved that the cubic B-spline based non-rigid registration method is capable of generating smooth interpolation to simulate the distortions between the target and reference image. The distortions were identified by minimizing the SSD or other similarity function between corresponding feature points which were defined manually.

Secondly, the method was tested on prostate data sets of 16 patients previously treated with RT where the clinical identified focal contours were available. A Gabor filter was used to select the corresponding feature points from the prostate contours on the reference and target images automatically. The focal contours were then varied based on the distortions between prostates. As shown in Figure 5.14, the non-rigid method did not make a big variation based on the rigid result because it is not sensitive to the tumor contour outside the prostate which is far from the feature points. As a result, the cases with non-focal tumor volumes were ignored. For the other cases, based on the clinician's experiences and judgments, the non-rigid registration method made an considerable improvement from the rigidly registered focal contour and could find the variation between prostates correctly.

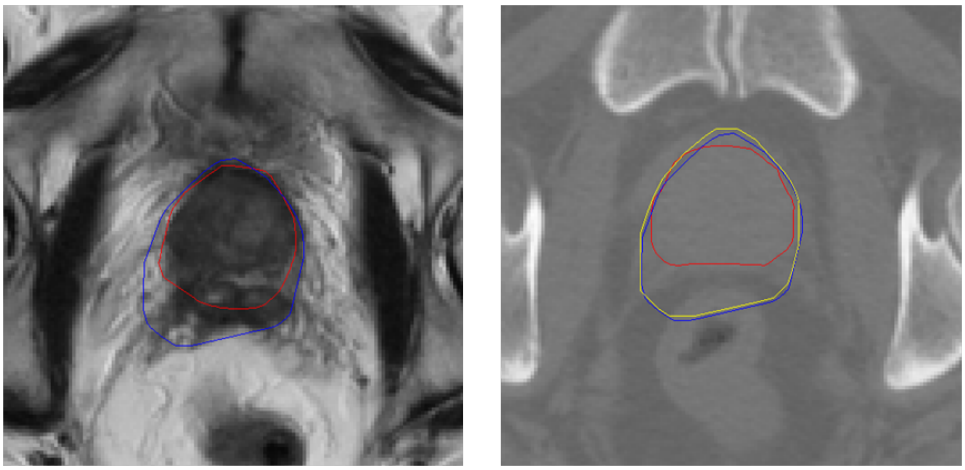

Figure 5.14: The example of the test case with large tumor volume. It showing that the non-rigid registration method is not sensitive to vary the tumor volume outside the prostate.

Chapter 6

The registration-segmentation framework

6.1 Introduction

As mentioned in Chapter 1, the aim of image registration is to provide comprehensive information for clinicians or as a pre-processing step for further image processing algorithms. Efficient registration and segmentation methods can assist in adaptive radiation planning in RT and therefore lead to IGART. In IGART, the treatment plan changes either within or between fractions. Therefore, more accurate treatment is delivered to tumor regions and less dose is delivered to healthy tissues. However, it is not sufficient to generate adaptive radiation planning using only CT images. Information from MRI, PET, CBCT and SPECT images are required for adaptive planning. Also, a robust and automatic segmentation approach that can use all of the registered information as prior knowledge and generate accurate GTV contours is needed. However, there is still no generally applicable pipeline for ART in clinical practice.

In this chapter, a registration-segmentation framework including the rigid registration algorithm introduced in Section 3.3, the non-rigid registration algorithm introduced in Section 3.4 and the level set segmentation algorithm introduced in Section 3.5 is presented. Section 6.3 provides a general introduction to this framework and illustrates its main components. Two data sets were used to test this framework: the target and reference image. They contain the same volume on different patients taken at different time points (the reference image is usually acquired before treatment with planning contours on it while the target image is usually obtained after treatment where new segmentation must be done automatically for IGART). The mapping between the target and reference image was identified firstly so that the reference contour could be used as prior knowledge on the target image. Finally an automatic segmentation method was applied to generate a new GTV contour based on the registered reference information. In this framework, four Dice coefficients are used to evaluate the step by step improvement. In Section 6.4 and 6.5, test data from veterinary patients treated at the University of Wisconsin for a range of different types of cancers were used to evaluate this framework. Performance was assessed by comparison with clinical contours and with conventional approaches.

Dog Number	Pre-treatment Data (slices)	Post-treatment Data (slices)
P1	CT (39), MR (26)	CT 6 weeks (43), CT 12 weeks (37)
P2	CT (54), MR (20)	CT 12 weeks (51)
P3	CT (42), MR (20)	CT 6 weeks (64)
P4	CT (33)	CT 6 weeks (48)
P5	CT (48), MR (22)	CT 6 weeks (38), CT 12 weeks (41) CT 24 weeks (38), CT 36 weeks (37) CT 48 weeks (46), MR 24 weeks (20) MR 48 weeks (26)

Table 6.1: Details of data sets used to test the novel registration framework in 5 dogs with nasal tumors.

6.2 Test data

In this chapter, a SIFT-MI based rigid registration algorithm, a B-spline based non rigid registration algorithm and a level set based segmentation algorithm formed a registration-segmentation framework that could be used for ART. Veterinary test data including planning CT and follow up MRI and CT images taken at different fractions of the treatment were used to test the performance of this framework (Table 6.1). Clinical contours of the GTV on the planning CT images (and/or pre-treatment MRI images) and follow up images were available as shown in Figure 6.1. The Dice coefficient was calculated between the clinical target contour and the automatically generated contour to provide an objective assessment.

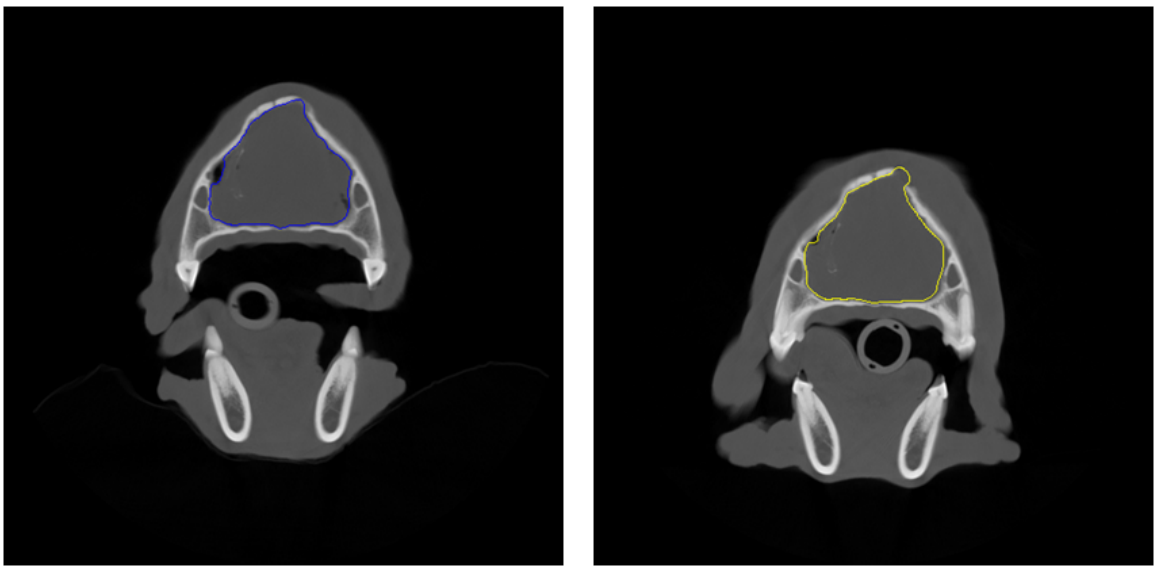

Figure 6.1: Left: the planning CT image of veterinary patient 5 with the clinical GTV contour shown in blue. Right: the CT image of the same patient 6 weeks after treatment with the clinical GTV contour shown in yellow.

Images were obtained from five dogs (P1-P5) with sino-nasal tumors treated with helical

Tomotherapy. CT imaging was performed using a single detector row unit (GE HiLight Advantage, GE Medical Systems, Milwaukee, WI, USA) with dogs in sternal recumbency while MRI was performed at 1.0T (GE Signa Advantage) with dogs in dorsal recumbency. All CT images were acquired with 512×512 pixels and a pixel size of 0.39 mm$\times$0.39 mm. All MRI images were acquired with 256×256 pixels and a pixel size of 0.62 mm$\times$0.62 mm. The number of CT and MRI image slices containing the tumor volume varied between dogs and data sets (Table 6.1). A board-certified radiation oncologist involved in the canine trial retrospectively evaluated all images and the contoured GTV, CTV, PTV and OAR for evaluation (JL).

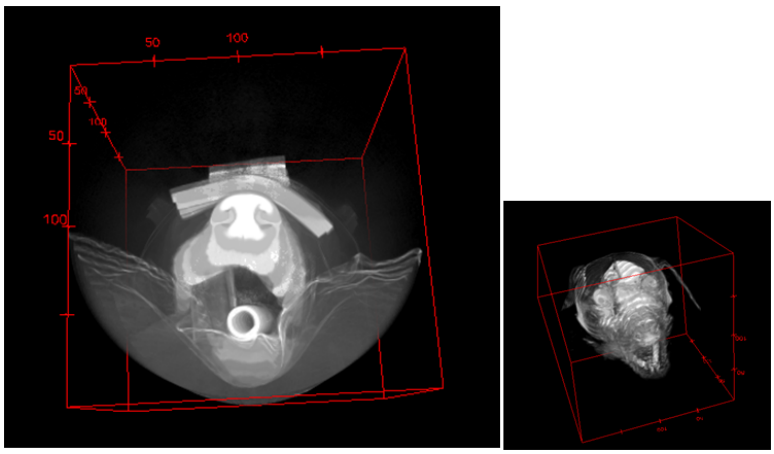

Figure 6.2: 3D examples of pre-treatment CT image (left) and pre-treatment MRI image(right).

Figure 6.2 shows a 3D example of the pre-treatment CT and MRI images in the test data set.

6.3 The registration-segmentation framework

To develop an efficient and practical IGART approach, an automatic and robust method for registration of images acquired at different time points with different modalities is required. In addition, an accurate segmentation method for non-rigidly tracking the GTV on follow-up is also required. The main achievement of this work is the development of an automatic registration-segmentation framework, which has the potential to achieve these aims. In this framework the planning contour of the GTV from the pre-treatment reference image is first registered to the post-treatment target image (both rigidly and non-rigidly). A segmentation method, which uses the registered data and planning contour as an initial zero level set function, is applied to find the new contour on the target image.

Level set methods offer an approach for automatically finding the GTV based on careful initialization and parameter settings. In this framework, a gradient-based level set method was initialized using the GTV defined by a registration approach using SIFT-based feature extraction. SIFT is a method that can find key points and their descriptors in scale space

and extract robust image features. MI is commonly used in intensity-based registration. The maximum MI between SIFT features on corresponding images was used here to determine the best image match. Rigid registration is sufficient when there is limited distortion between the target and reference images. However, in the presence of distortion a non-rigid transform is required. The proposed algorithm has non-rigid capability by minimizing a cost function based on the SSD between feature points and the MI between clinical regions of interest. The veterinary patients described in Table 6.1 were used to test the proposed framework because there are many similarities between human and animal cancers. As mentioned in Chapter 1, this also presents a unique opportunity to improve radiotherapy for both patient groups as data of veterinary patients are easier to access while technologies for human patients are better developed.

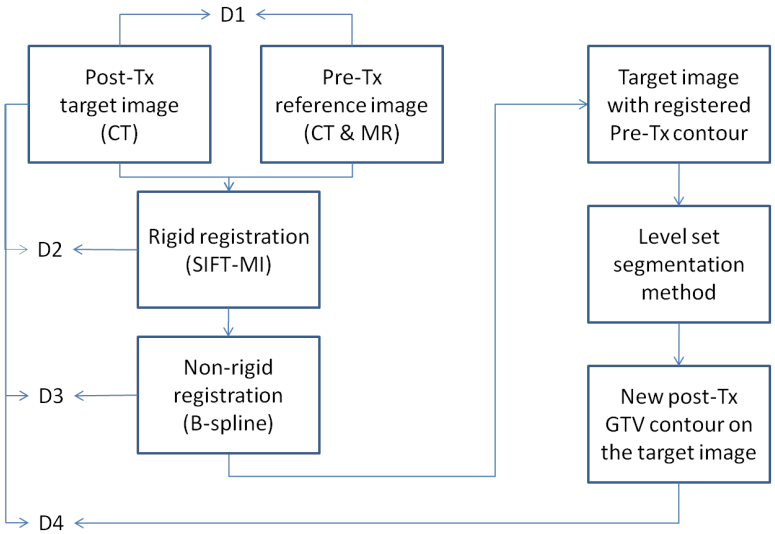

Figure 6.3: Flow chart of the proposed registration-segmentation framework: rigid registration, non-rigid registration (optional) and level set segmentation.

Four Dice coefficients (D1: between the original reference contour and target contour; D2: between the rigid registered reference contour and target contour; D3: between the non-rigid registered reference contour and target contour; D4: between the final segmented result and target contour) are used here to assess the improvement step by step in this framework as shown in Figure 6.3.

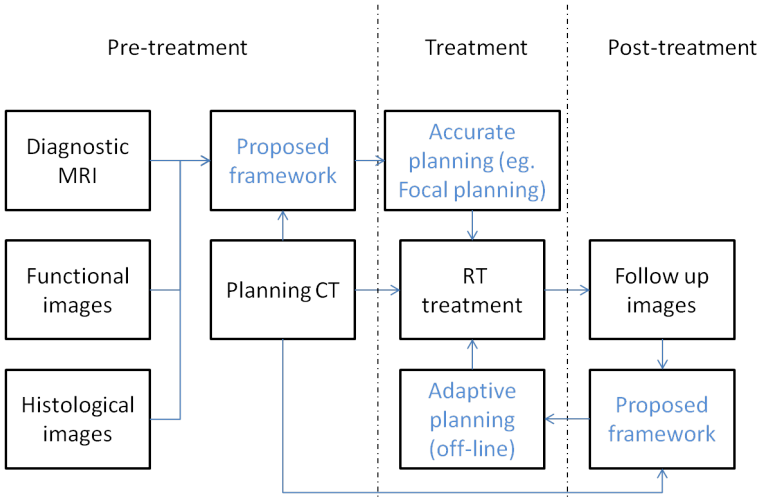

Figure 6.4: The proposed framework in a typical RT process. It can be used to generate images with more comprehensive information by finding the mapping between pre-treatment images from different modalities. Also it can be used to identify changes to the tumor volume on follow-up images for off-line ART

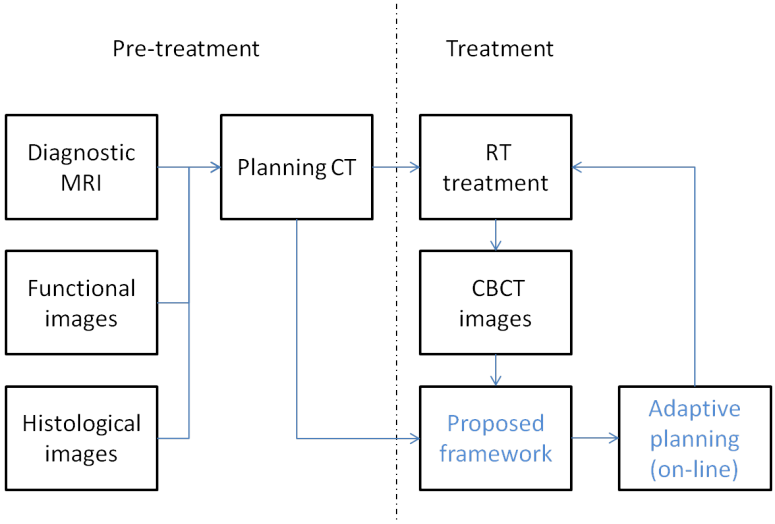

Figure 6.5: The proposed framework in an on-line IGART process. Images acquired during the time of treatment (CBCT) and planning CT images are registered by the framework and new segmentation results can be provided in real time to adapt the RT planning.

In practice, the proposed framework can be used in the RT process for three different applications as shown in Figure 6.4 and 6.5. Firstly, it can be used to register pre-treatment images from different modalities and provide more comprehensive information for RT planning. This is because CT is the most commonly used modality for RT planning but complementary information can be provided by images from other modalities. By using combined information from multi-modality images, more accurate tumor segmentation results can be generated and

therefore the side effect of radiation treatment is minimized. In this case, the input reference data set is planning CT images and the target data sets can be MRI, PET (or other functional images) and histological images. The output of the framework is the registered GTV contour on the reference data set (eg. cases with focal prostate cancer presented in Chapter 5).

Secondly, the proposed framework can be used for off-line IGART which adapts the dose planning between fractions. In this application, the input reference data set is planning CT images and the target data sets are follow-up images obtained after treatment (usually CT or MRI). The aim of this application is to generate adaptive segmentation for every fraction in RT based on the registered clinical contours from the reference data set. It can track the variation of the tumor volume between fractions and help to evaluate the response of the GTV to radiation. Different and more accurate RT planning can be generated based on the adaptive segmentation on follow-up images. This approach was tested on the veterinary data sets previously introduced.

Thirdly, the framework has the potential to achieve on-line IGART which adapts the dose planning during the time of treatment. CBCT images obtained during the process of treatment can be sent to the framework as the target data set. After combining with planning CT images (the reference data set), the new GTV segmentation can be generated on CBCT images and therefore provide real time guidance for RT. However, this still requires further work to overcome the computational difficulties and image reconstruction algorithms required for the framework.

6.4 Comparison of performance with conventional algorithms

Figure 6.6 shows the similarity measurements for SSD, SSD of SIFT feature points, MI and MI of SIFT feature points between CT and MRI images. Although SSD and SSD of SIFT feature points give acceptable results there are several local minima. It would therefore be difficult to establish a global minimum in more complex multi-modality cases using these conventional measurements. The MI measure calculated on the image gave a large error (Figure 6.6 bottom left). However, in the proposed framework, using the MI of SIFT feature points (Figure 6.6 bottom right) gave a very distinct global minimum

Similarly in Figure 6.7, where the results for translation are shown, SSD shows a good response over the complete parameter range. However, comparing with MI of SIFT features, the global minimum of SSD has small differences in local minimums which makes it looks ‘flat’ at a larger scale (Figure 6.7 top left). It is also shown that the SSD of feature points and MI do not give any clear minimum (Figure 6.7 top right, bottom left) and that as before the proposed approach based on MI of SIFT feature points gives a clear global minimum.

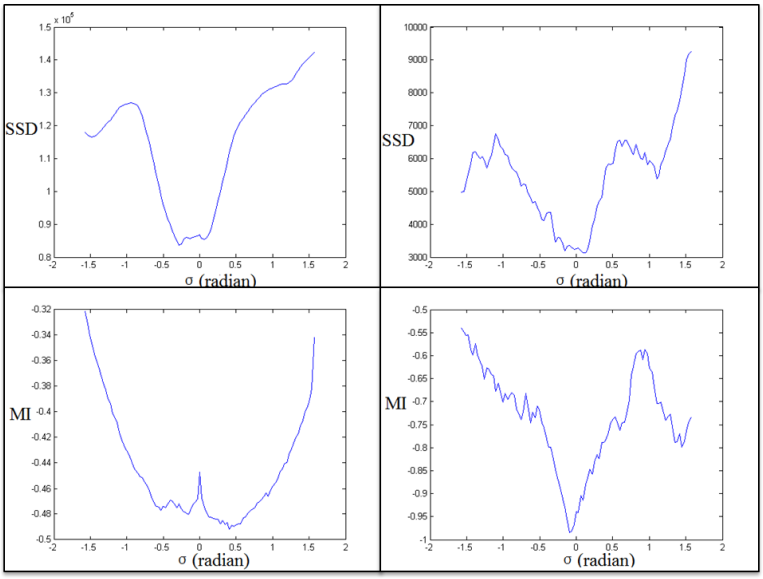

Figure 6.6: Different similarity measurement for rotation (-90° to $+90^\circ$): SSD between the target and reference image (top left), SSD between feature points on the target and reference image (top right), MI (negative) between the target and reference image (bottom left) and MI (negative) between feature points on the target and reference image (bottom right).

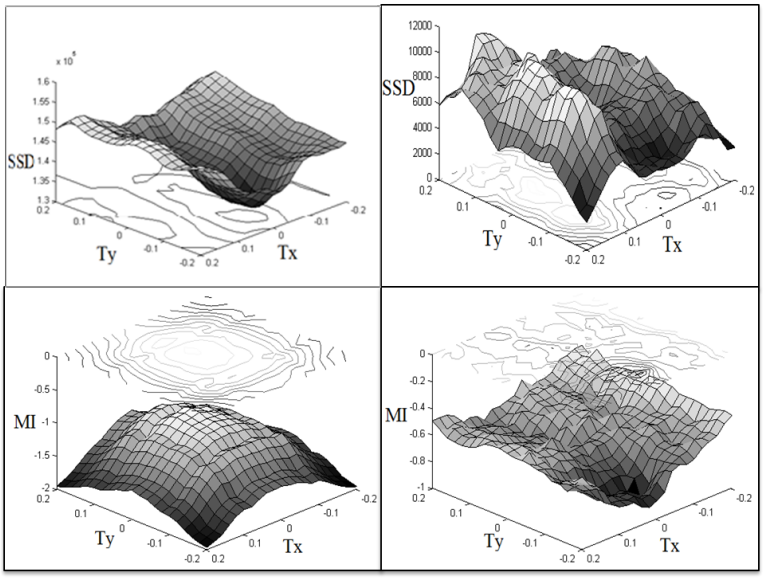

Figure 6.7: Different similarity measurement for translation (-40% to 40% of total image): SSD between the target and reference image (top left), SSD between feature points on the target and reference image (top right), MI (negative) between the target and reference image (bottom left) and MI (negative) between feature points on the target and reference image (bottom right).

6.5 Results and discussion

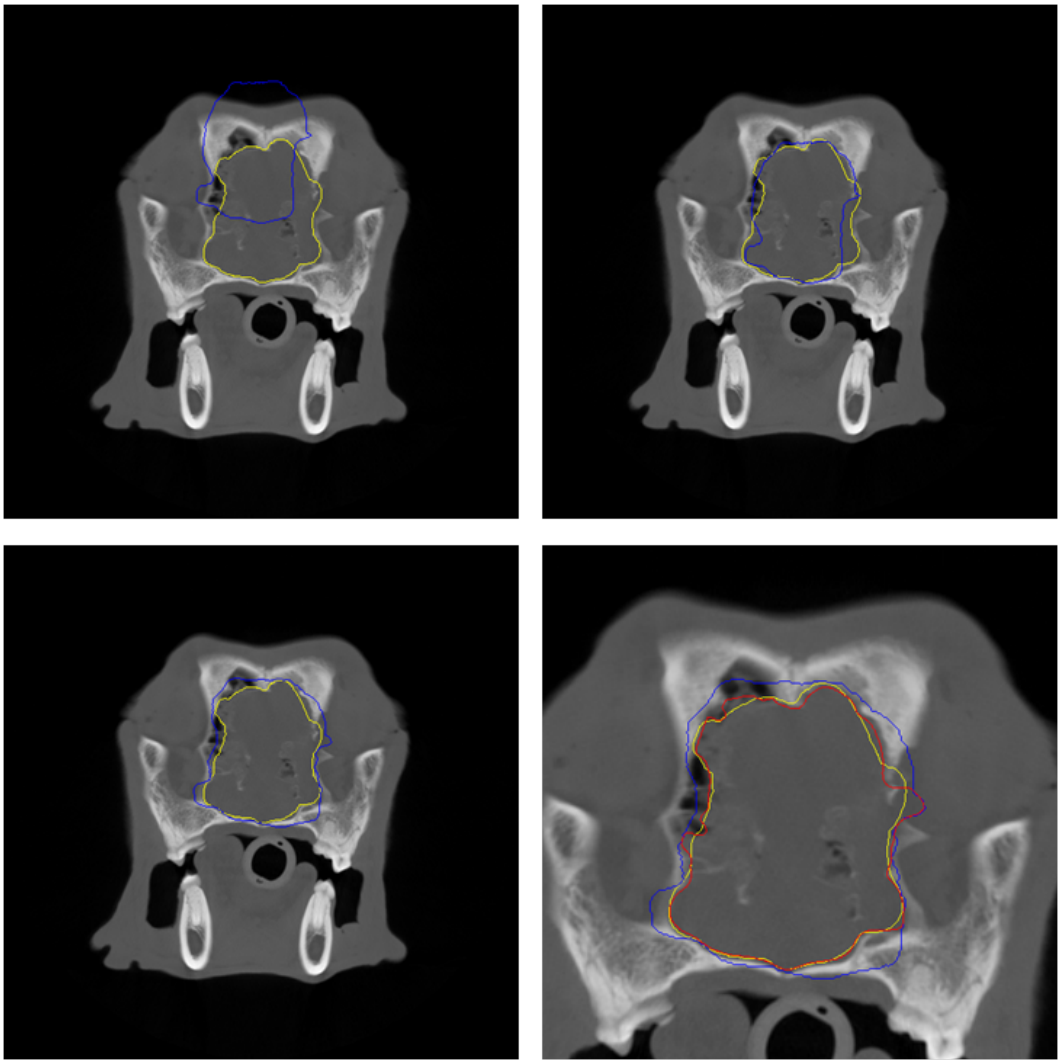

Figure 6.8: Target image with the pre-treatment GTV contour (C_R: blue), the the target GTV contour (C_T: yellow) and the automatically generated contour (C_G: red). D1 = 42.65 % (top left), D2 = 85.57% (top right), D3 = 90.81% (bottom left), D4 = 96.73% (bottom right).

The framework was initially tested on pre-treatment and 6-week post-treatment images from P5, where the images were from the same modality (CT) which are shown in Figure 6.8. The registration result of C_R is shown in blue, the target contour C_T generated by clinicians is shown in yellow and the automatically segmented GTV contour C_G produced by the proposed algorithm is shown by the red contour on the right bottom image. The Dice coefficient between the clinical contour C_T and C_G for this case is 96.73%.

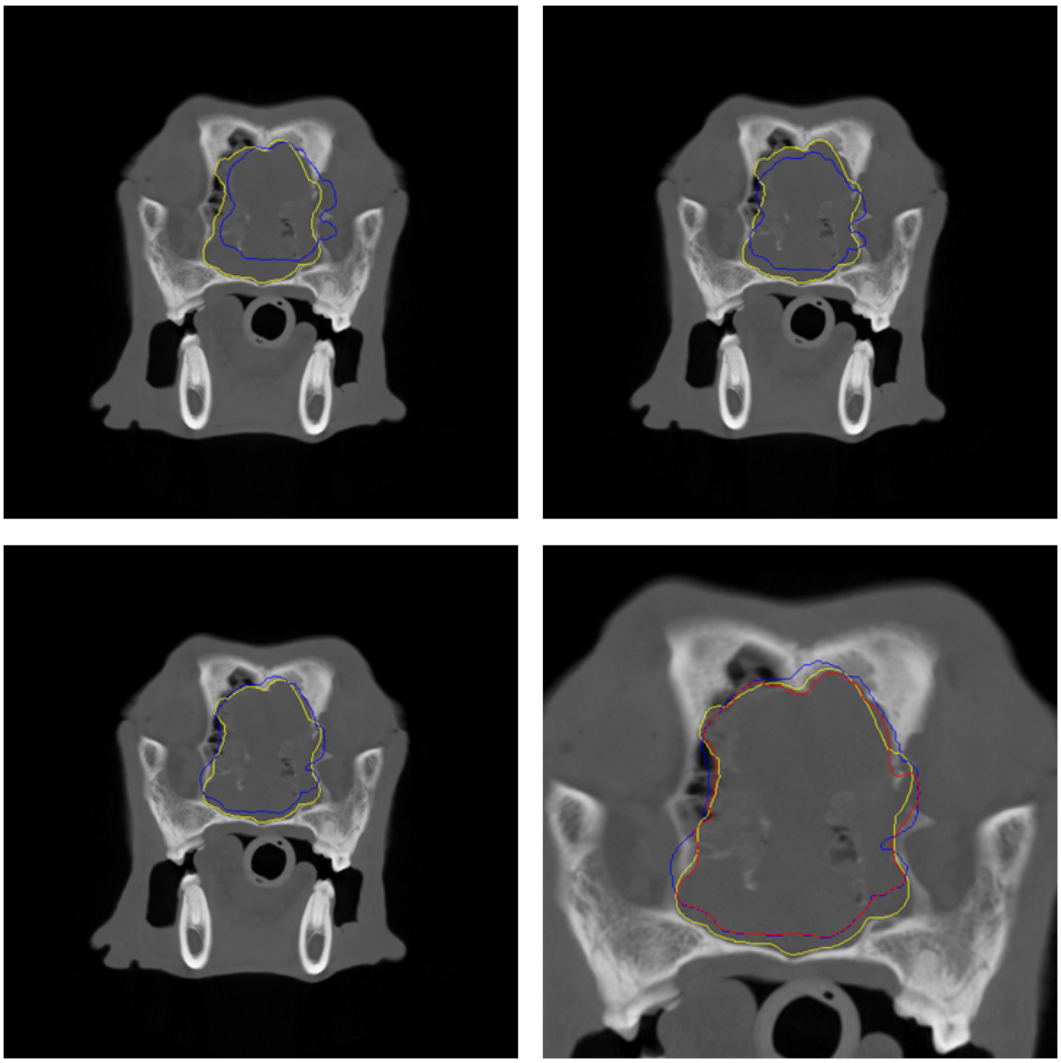

Figure 6.9: Target image with the pre-treatment GTV contour (C_R: blue), the target GTV contour (C_T: yellow) and the automatically generated contour (C_G: red). D1 = 79.76 % (top left), D2 = 86.78% (top right), D3 = 90.07% (bottom left), D4 = 93.7% (bottom right).

As shown in Figure 6.9, the framework was next tested on multi-modality data from P5 comprising of pre-treatment MRI and CT images acquired 6 weeks after treatment. In this case the reference contour from the MRI image shown in blue was pre-processed by scaling and rotating prior to SIFT-based matching. This is because there are different pixel sizes and orientations between CT and MRI images. The Dice coefficient between the clinical contour C_T and C_G for this case is 93.7%.

In Figure 6.8 and 6.9, the top left, top right, bottom left and bottom right images show the contours used in the calculation of D1-D4 on the target image respectively (D3 was calculated from the non-rigidly registered contour but the contour shown in bottom left image was after adding a 3 pixels margin). They have the same target data set (6-weeks post treatment) but

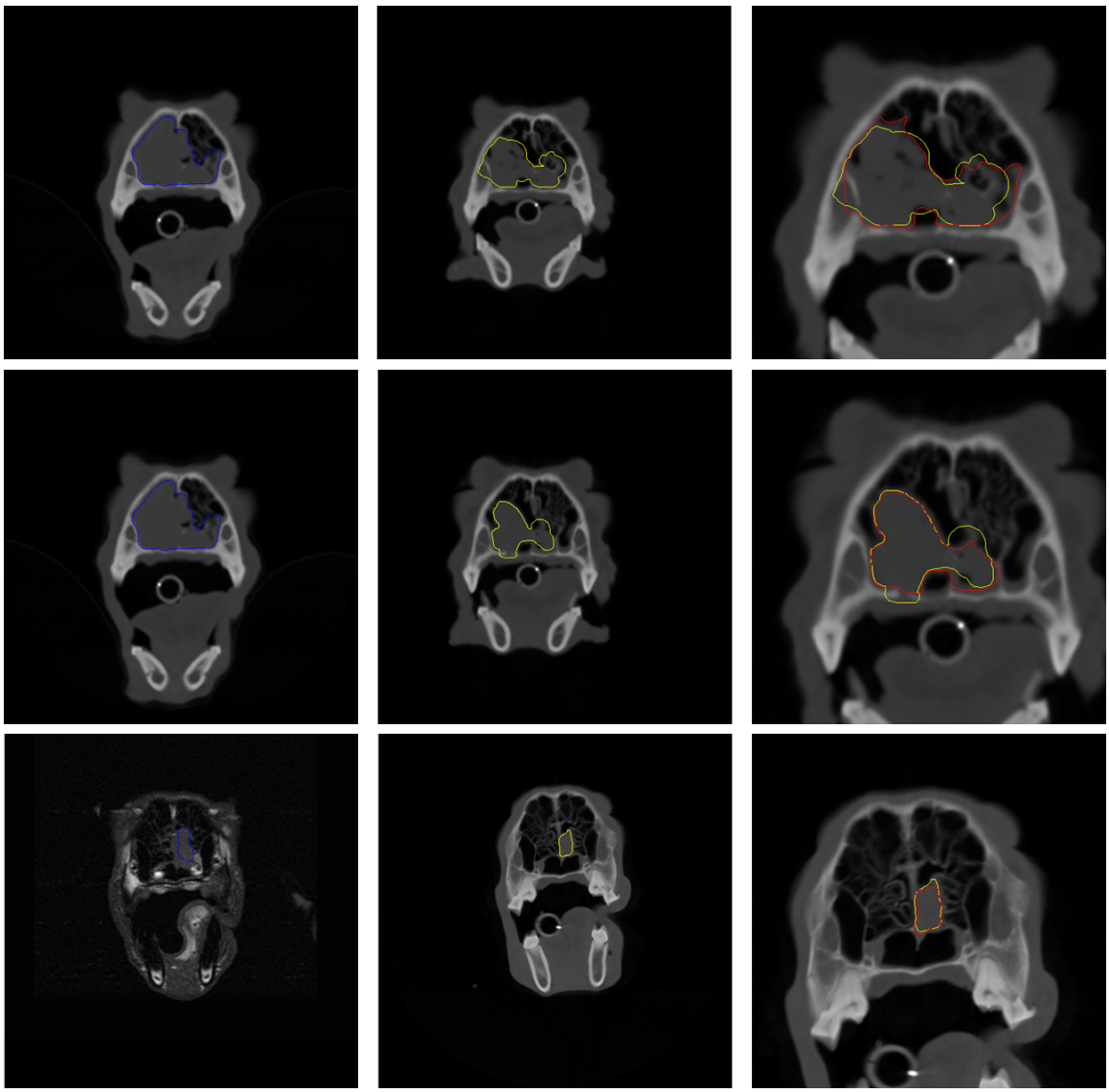

Figure 6.10: Left: the pre-treatment reference image with C_R in blue. Middle: the post-treatment target image with C_T in yellow. Right: the area of interest with C_T in yellow and C_G in red. Results on the target image 6 weeks after treatment of P1, 12 weeks after treatment of P1 and 6 weeks after treatment of P4 are shown from top to bottom respectively.

different reference target data sets from different modalities (Pre-treatment CT and MRI). However, D1 for both cases (42.65% and 79.76%) illustrates that there are relatively large spatial differences between the original reference and target contour. By using the proposed rigid registration method, an benefit can be observed in D2 (85.57% and D2 = 86.78%). As a result the rigid method proved to be suitable for registering images from same modality or different modalities. This is because SIFT feature points are usually selected around bones and invariant to gradient variations. This is different in focal prostate cancer data in Chapter 5 where the tumor volume is near to bones and therefore SIFT feature points can also be used for the non-rigid registration. The non-rigid registration process can be treated as a track of the shape variation of the GTV. Based on the rigid registration result D3 showed a notable improvement (5.24% and 3.29%) from D2 for both of the cases. As shown in the bottom right image in Figure 6.8 and 6.9, the level set method was used to evolve the non-rigidly registered contour (with margin) to find a more appropriate shape for the tumor volume on the target image. Level set methods can evolve for different directions (inside or outside) based on the tumor volume variation between the reference and target image. Comparing with the target contour (C_T), the automatically segmented GTV contour (C_G) demonstrates strong clinical agreement and achieves the Dice coefficient of over 90%.

In Figure 6.10, the result from different patients, acquired at different time points and from different modalities are compared. Comparing the top and middle row, they have the same reference data set (pre-treatment CT of P1) and target data set from the same modality (CT) but were acquired at different time points (6 and 12 post-treatment). It shows that the reference contour is the same and the target contour is heavily deformed due to disease progression/regression or change in anatomy. Also, it can be easily observed that the bone structures for them are very similar. As a result, the non-rigidly registered contours between them do not have an obvious difference. However, the presented framework can still provide acceptable results for both of them (86.22% and 89.7%). This is because the level set method evolved the non-rigidly registered contour differently based on the local image information on the target image. The images in the bottom row in Figure 6.10 are from P4 and the reference data set is from pre-treatment MRI. Comparing the first two rows with it, the GTV in them has huge differences in volume and size while the final segmented Dice coefficient for this case is 87.69%. The reason for this is that the framework uses clinical pre-treatment contours as a reference, which can always put the initial level set contour at the correct position. These results demonstrate that as long as the GTV changes its size, shape and position within a reasonable range, the framework can track its variation by using pre-treatment prior information.

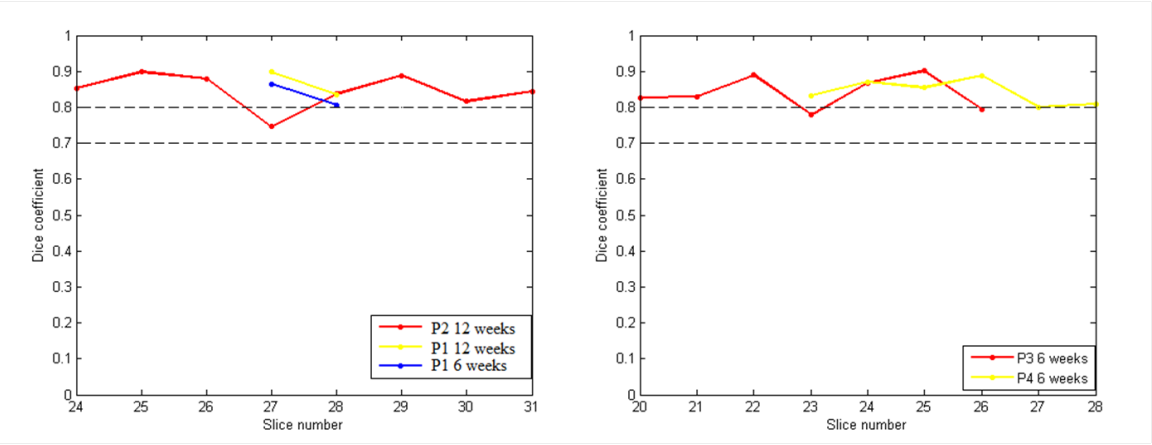

Figure 6.11: The Dice coefficient calculated by comparing C_T to C_G on all images acquired on P1 to P4. The overall Dice is 84.44%.

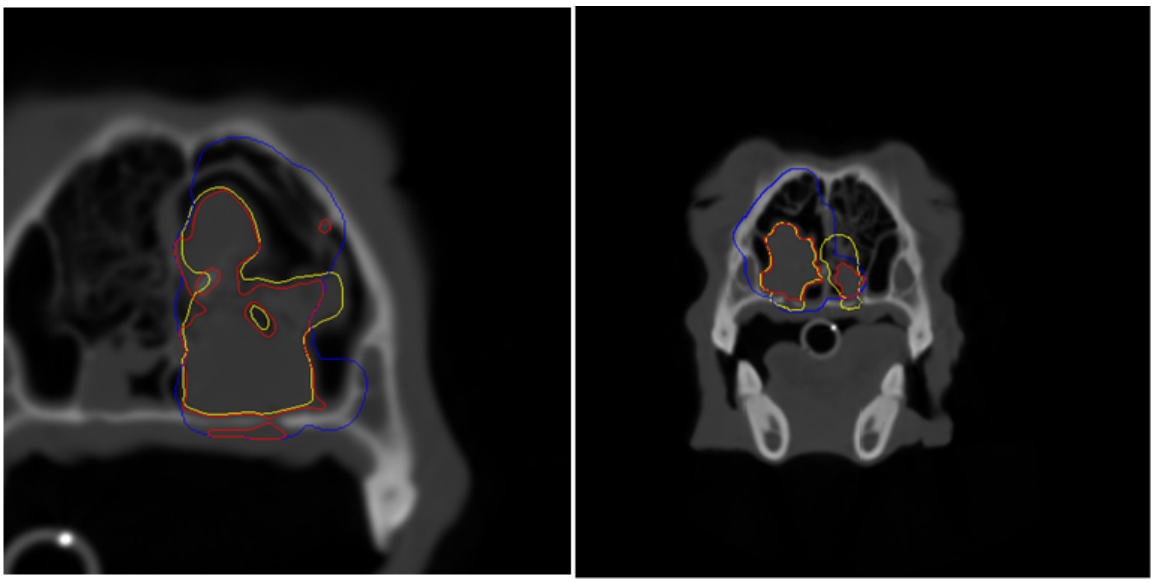

Figure 6.12: Examples of automatic topology changes based on level set method (Left: P3; Right: P1).Target image with the pre-treatment GTV contour (blue), the target GTV contour (yellow) and the automatically generated contour (red).

Figure 6.11 shows the slice-by-slice Dice coefficient calculated on the first 4 patients used in the study. Overall performance was found to be $> 80\%$, however, further work is required to assess the performance of the approach on estimating the position of the GTV for different cancers and over a longer time course.

Figure 6.12 shows another advantage of this framework: it can find the topology changes automatically. In practice, the GTV usually appears as a volume in 3D case but does not have to be continuous on 2D image. On the left example from P3 in Figure 6.12, the target contour (yellow) has a little circle inside the large contour which was accurately identified by C_G (red).

This is because level set method worked in a higher dimensional space where the tumor volume is continuous. Also, parameters for level set method were set to be 'strict' to define small circles accurately, the framework unavoidably provided some noise circles around or inside the target contour. This problem can be solved by changing smooth filter or the speed function model of level set method. Similarly, on the right image from P1 in Figure 6.12, C_G (red) can find the separate parts of the target contour correctly.

Overall, the approach has the potential to be used as part of an adaptive radiotherapy strategy for personalized radiotherapy that is tailored to time-of-treatment variations of the GTV.

6.6 Implementation and optimization

All the algorithms in this thesis were coded and tested using MATLAB 2012b (Mathwork, Sep. 2012). Specifically, implementation details of three main parts (rigid registration, non-rigid registration and segmentation) in the proposed framework are introduced in this section.

6.6.1 The rigid registration method

In the proposed rigid method, SIFT is used to extract feature points and MI of neighboring areas is used as the similarity measurement. As shown in Figure 6.13, taking the test data shown in Figure 4.2 as an example, there are 378 ($A2$,$B2$) features in the target image and 3056 ($A1$, $A2$) features in the reference image after applying SIFT algorithm. The arrows in the image represent the orientation of the gradient at the feature point and the length of them gives the magnitude of the gradient. It shows that the features focus on distinct areas which have relatively large gradient. Therefore, they concentrate on nearly every small hole and the edge of the large circle. This means the feature extraction method can choose the landmarks automatically to some extent. As mentioned in Section 3.3, at most 3434 ($378 + 3056$) neighboring areas can be extracted to form the feature image. However, not all of them can be used because: 1. some of them focus on irrelevant background; 2. increasing number of matches used will increase computation time of MI; 3 the neighboring areas of them may include the same pixel.

To select an appropriate number of feature points (n_f) used for registration, Figure 6.14 shows the relationship between the number of extracted feature points and the average number of effective pixels (exclude repetitive and background pixels) over 124 CT slices (512×512) from a prostate cancer patient. Although increasing the number of extracted feature points will provide more information (pixels), it is less efficient because the number of effective pixels increases at a lower and lower rate.The optimal performance with reasonable number of effective pixels and high efficiency for computation was found when n_f was approximately 10.

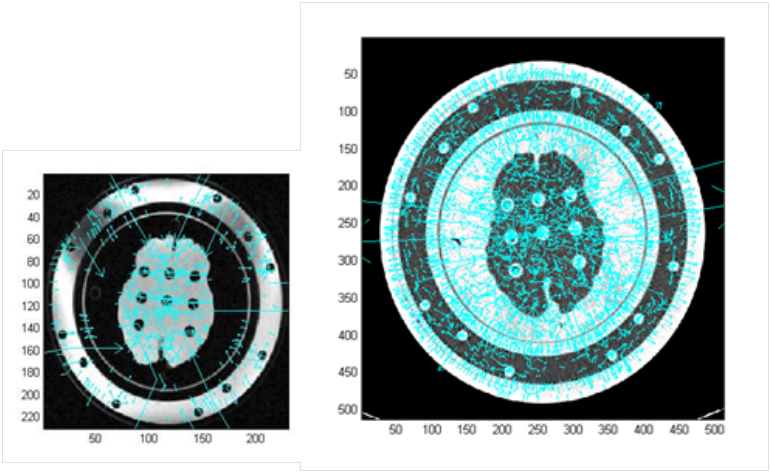

Figure 6.13: The features of image A. The arrows stand at the keypoints and point to the directions of the gradients of the keypoints. The lengths represent the magnitudes of the gradients.

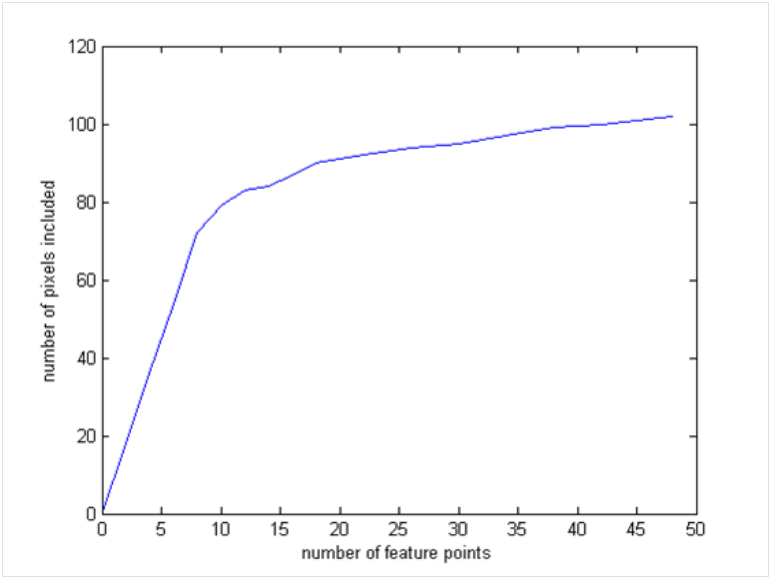

Figure 6.14: The relationship between the number of extracted feature points and the average number of effective pixels over 124 CT slices from a prostate cancer patient.

After selecting (with largest gradients) 10 feature points on the reference and target image respectively, the 3×3 neighboring areas of them are extracted (Figure 6.15) and formed into two feature images (A and B, Figure 6.16). For different transformation parameters, the contents in A and B are varied. As a result, MI can be calculated and optimized between A and B to find the best registration parameters.

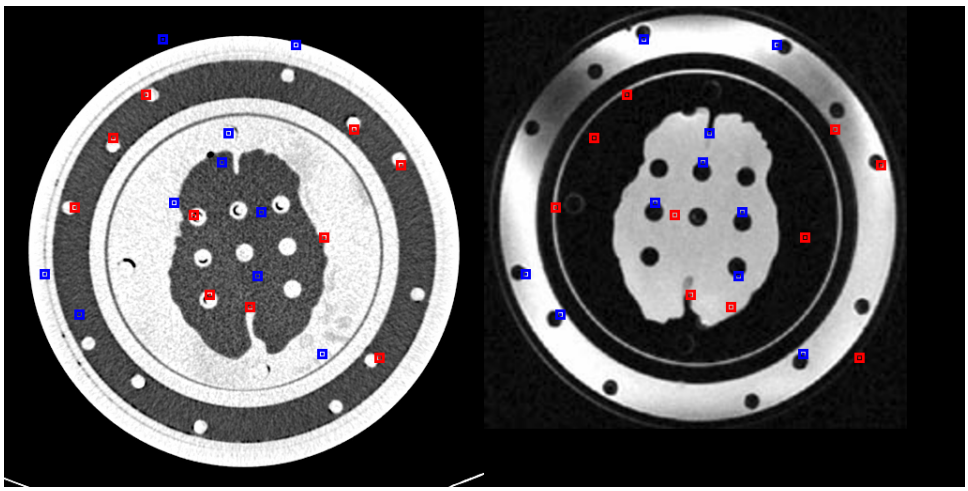

Figure 6.15: Left: the original reference image with A1 in red and A2 in blue. Right: the original target image with B1 in red and B2 in blue.

Figure 6.16: From top to Bottom: A1, A2, B1, B2, A and B

Also, because the proposed method only considers feature images, it runs much faster than conventional MI-based methods. For example, it cost 0.49s to register the test data while the MATLAB function *imregister* cost 7.32s on the same machine.

6.6.2 The non-rigid registration method

The proposed non-rigid method mainly includes two similarity measurements: SSD between corresponding feature points and MI between distinctive regions. As shown in Figure 6.17, taking the test data shown in Figure 5.8 as an example, the correspondences of feature points were defined by the Gabor filter as mentioned in Section 3.4.2 and the distinctive regions on bones were defined manually.

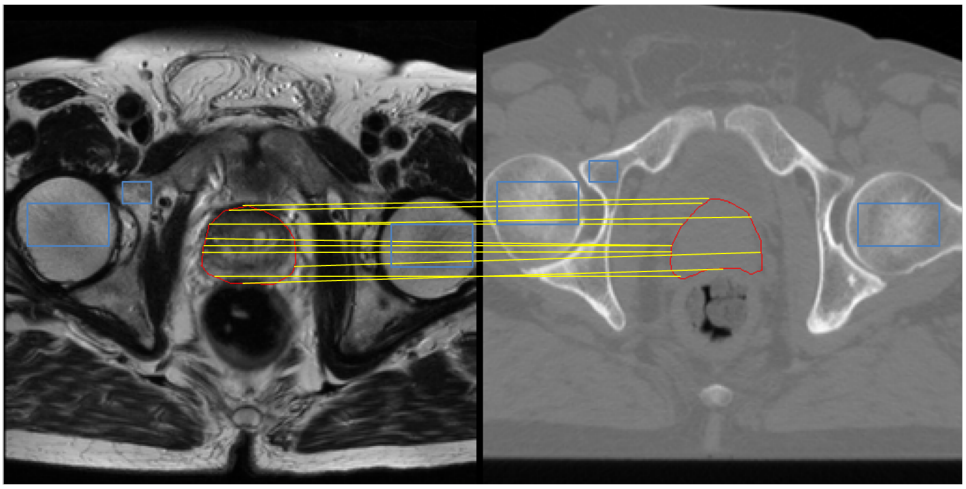

Figure 6.17: The test reference and target image with 10 corresponding feature points on prostate contours identified by Gabor features and 3 manually defined distinctive regions.

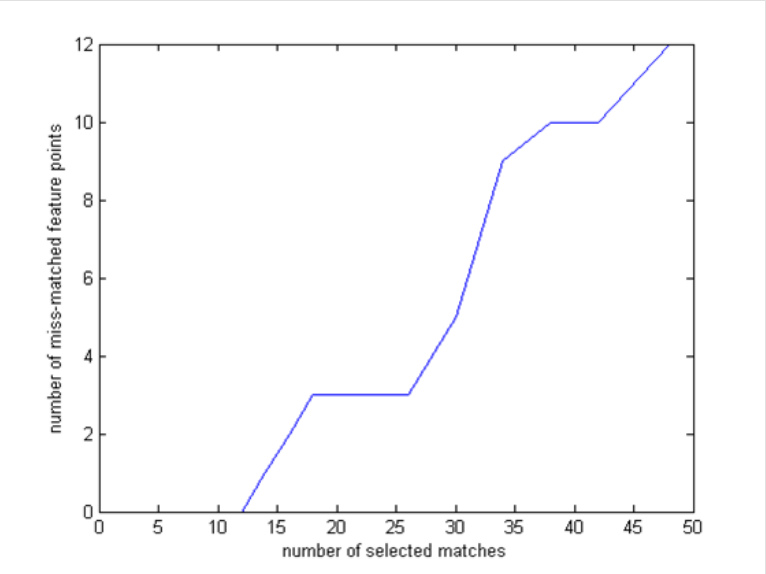

Figure 6.18: The relationship between the number of selected matches (n_m) and the number of miss matched feature points between typical CT and MRI images.

The relationship between the number of selected matches (n_m) and the number of miss matched

feature points between typical CT and MRI images (Figure 5.8) is shown in Figure 6.18. Clearly, the more matches selected, the more miss-matches are included. The optimal value with enough matches to find the distortion between prostates and 0 miss-match was found when n_m was approximately 10. The 10 best matches were identified by finding the 10 pairs of feature points with smallest SSD of Gabor features. Then the cubic B-spline method was used to simulate the distortion between prostates. The registered result was shown in Figure 5.9. In Figure 6.19, typical poor performances of the approach caused by setting relatively large w_1 and large w_2 are shown. When w_1 is too large, the non-rigidly registered result is affected mostly by feature points and as a result, once feature points are miss matched, the result will have unpredictable deformation and provide an irrelevant mapping. When w_2 is too large, the result is dominated by the distinctive region and therefore adds very little distortion on the original contour.

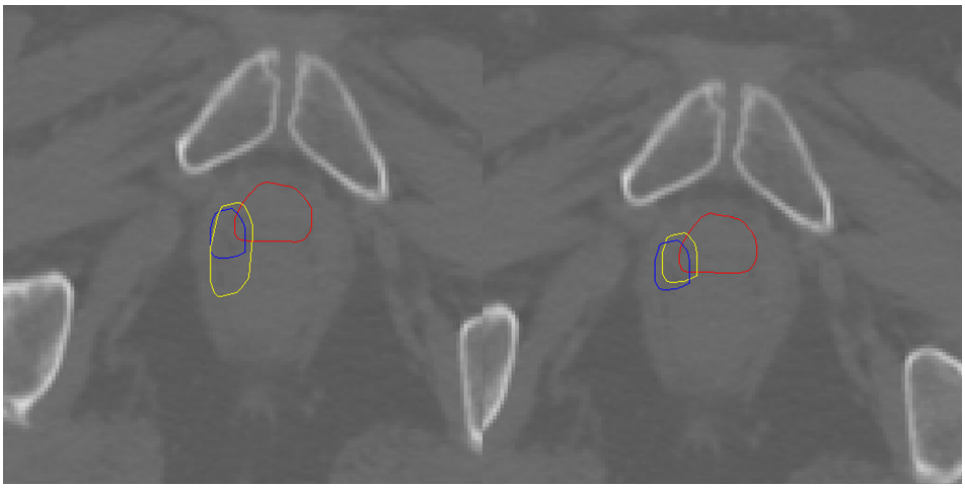

Figure 6.19: Left: rigidly registered focal region (blue) and non-rigidly register focal region (yellow) with relatively large w_1 (w_1 = 0.2 and w_2 = -10000). Right: rigidly registered focal region (blue) and non-rigidly register focal region (yellow) with relatively large w_2 (w_1 = 20 and w_2 = -10000).

6.6.3 The level set segmentation method

Instead of using a regular shape, the registered (both rigidly and non-rigidly) clinical contour was used for the initial zero level set function in the proposed framework. Taking the test data shown in Figure 6.8 as an example, Figure 6.20 and 6.21 show the segmentation results using Chunming Li's level set method initialized with a square located on the interested area (manually defined). These results were generated using the same parameters as the results in Figure 6.8. Clearly, results of the conventional method highly depend on the size and position of the initial contour and they can be easily affected by irrelevant edges. As a result, comparing with the conventional method, the proposed framework provides fully automatic and much more accurate segmentation results.

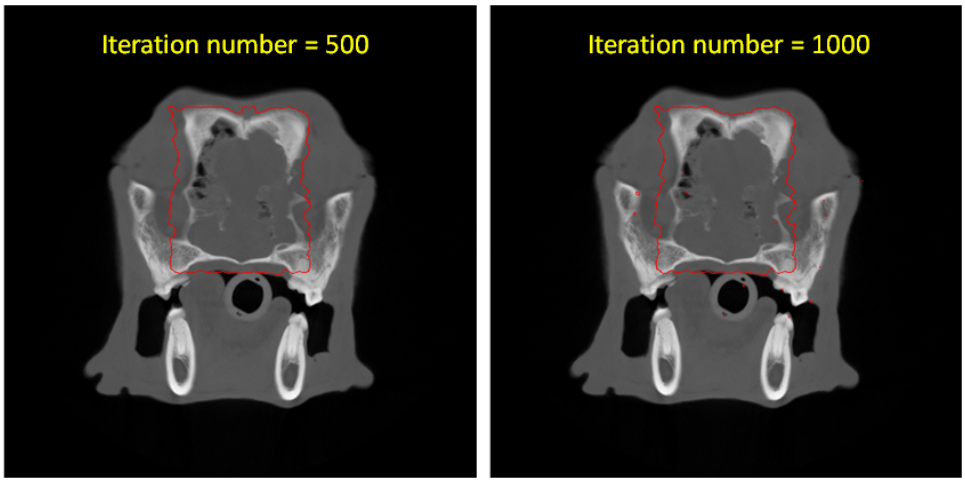

Figure 6.20: The segmentation result using Chunming Li's method with a large square-shaped initialization iterated by 500 times (left) and 1000 times (right).

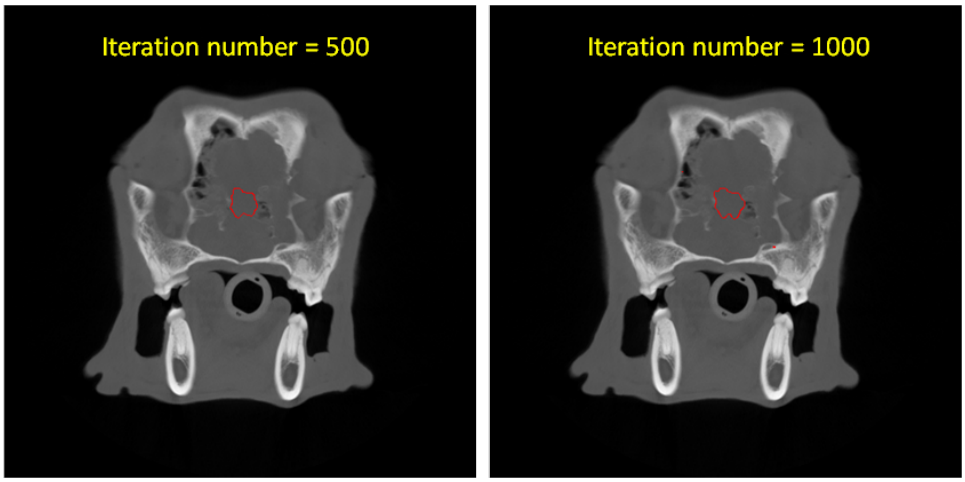

Figure 6.21: The segmentation result using Chunming Li's method with a small square-shaped initialization iterated by 500 times (left) and 1000 times (right).

6.7 Conclusion

The proposed registration-segmentation framework demonstrates that by using prior information from pre-treatment images it is possible to automatically segment the GTV on post-radiotherapy images with acceptable clinical accuracy (mean Dice, 84.44%). Further work is required to assess the performance on a larger data set and using other imaging modalities such as PET.

Here, image registration simply refers to the comparison of one dataset to another. The complexity behind making quantitative use of this imaging data has been reviewed here, illustrating

that it is necessary to determine the transformations needed to relate coordinates of one dataset to another. The impact of image registration on RT from treatment-planning to image-guided delivery to post-treatment follow-up is enormous and has already impacted veterinary patients. Novel registration frameworks may be ideally tested on companion animals undergoing RT given similarities between human and veterinary radiation oncology. Ultimately optimized image registration and data fusion techniques should aid in targeting tumor volumes and organs-at-risk, improve response assessment and increase the availability and utility of a rapid ART approach.

Chapter 7

Conclusion

7.1 Summary

In this thesis, an image analysis-based framework for IGART was presented using novel rigid image registration, non-rigid registration and level set algorithms. Various data sets from different modalities including manually created test images, CT, MRI, CBCT, PET and EPID images and with different types of cancers including lung, prostate and nasal cancer were used to test these algorithms. Both subjective validations from clinicians and objective assessment (eg. Dice coefficient) were used to evaluate the performance of its applications. This framework has the potential ability to track the shape variation of the GTV and therefore provides adaptive segmentation on-line or off-line. As a result, more accurate radiation delivery could be achieved automatically based on this approach.

Chapter 4 focused on the SIFT-based rigid registration algorithm. It was tested on the phantom data sets to find how it works between multi-modality images (CT and MRI). To validate its performance on practical medical images, it was used to register planning CT images with CBCT images obtained at different fractions of treatment. Here, the transformation matrix, which was defined by radiographers and could be calculated from DICOM information, was treated as the gold standard to assess the performance of this method. Both 2D and 3D algorithms were applied on 9 CBCT data sets and all the errors calculated by comparing with the transformation matrix were recorded. Instead of using SIFT as a point matching technique, here it was only used to extract representative points (feature points) on the reference (RFP) and target image (TFP) respectively. 3×3 neighboring regions around RFP (A1), TFP (B2), regions around the same coordinates of RFP on the target image (B1) and regions around the same coordinates of TFP on the reference image (A2) were extracted and used to form two feature images (A and B). Comparing with conventional MI-based algorithms which calculate MI between images directly, it only calculates and optimizes MI between feature images. It leads to 3 advantages: 1. It minimizes the effect of background pixels and is not sensitive to noise. For the CBCT test data, it provided registration results with the average relative error less than 5% in both 2D and 3D cases; 2. It can work between different modalities which can not be achieved by conventional methods [23]; 3. It runs much faster than conventional algorithms. For the test data mentioned in Section 6.6.1, it cost 0.49s while the MATLAB function *imregister* cost

7.32s on the same machine.

Chapter 5 presented the results and validations of the non-rigid registration method. To test how SIFT-based feature extraction method works in it, the non-rigid algorithm was applied on manually warped images. The Euler distance before and after B-spline interpolation were compared to show the improvement. Also, planning CT and diagnostic MRI images from patients with focal prostate cancer were used to test this method when the Gabor filter was used as the feature extraction method instead of SIFT. The registration results were judged by the clinician who provided the original contours manually. Also, according to the clinician's experience, four ratios (R1-R4) representing the overlap rate between focal contours and corresponding prostate contours were used to assess its performance. Comparing with conventional deformable registration methods, a new similarity function was developed and the advantages include: 1. It can appropriately balance the deformation of soft tissues and the stability of bones between images from different modalities. As a result, it can identify deformed focal regions on planning CT images for more accurate RT planning; 2. It can track the variation (shape and volume) of the target organ between images taken at different time points and therefore can be used to evaluate the response of radiation.

Chapter 6 provided the workflow and three applications of the registration-segmentation framework in RT which combined the rigid and non-rigid registration algorithm with level set segmentation algorithm. As mentioned in Chapter 1, veterinary data sets are useful for studying image processing approaches designed for humans. Therefore, 5 dogs with nasal tumors from the University of Wisconsin were used to test the framework. All the pre-treatment and post-treatment images were contoured by a veterinary oncologist so that 4 Dice coefficients calculated by comparing them with automatically generated contours were used to show the improvement step by step. The proposed framework generated accurate tumor segmentation results (average Dice = 84.44%) and was treated clinically acceptable. Comparing with the conventional level set method, as presented in Section 6.6, the regular initialization (square) of level set method on manually defined positions (on or include the ROI) can't provide acceptable results because level set method can be easily trapped by irrelevant edges and therefore it is sensitive to the position and shape of the initial contour when it is used for tumor segmentation.

7.2 Conclusion and future work

From all the presented results, the conclusion can be made that SIFT method and the Gabor filter are efficient feature extraction methods and can provide useful image information for similarity calculation. The rigid registration method is capable of finding the rigid transformation between images from the same modality or different modalities. Also, the rigid method was proved to be much faster that conventional MI-based algorithms because it focused on the feature points and their neighboring points. All the recored errors for both 2D and 3D methods

on CBCT data set were under 5%. The non-rigid registration method was shown to be capable of finding the shape variation of the GTV or other organs. It is useful in the assessment of radiation responses and focal RT. For the 15 test cases, almost all the registered results were acceptable to the clinician. The registration-segmentation framework can provide automatic segmentation on the target image with appropriate input and therefore has the potential ability to achieve adaptive planning in RT. The mean Dice coefficient for 5 dogs was 84.44% and the Dice coefficients for almost all cases are above 80%.

In the future, there are 4 tasks can be done to improve the proposed framework:

1. More comprehensive data sets which have images from more modalities such as PET, SPECT and histology and images acquired at different stages in RT such as diagnosis, pre-treatment and post-treatment need to be used to test the proposed framework. Based on these data sets, parameters in the framework could be optimized for different situations and the difference between them can be assessed. In addition this could be complemented by more clinical information such as age, gender and weight of patients, image data sets can be divided into different groups and compared respectively. Further more, machine learning techniques (eg: support vector machine or artificial neural network) can be used to generate an automatic parameter setting approach based on the manually optimized parameters in training data sets.

2. The rigid registration algorithm can work in both 2D and 3D while the non-rigid registration approach can only work in 2D. As a result, although the rigid method can minimize the spatial error as a pre-processing step, the performance of the non-rigid method can still be heavily affected by small errors in z direction which may cause miss-matched slices. To solve this problem and make the proposed framework more efficient, the non-rigid method needs to be improved to work in 3D. A 3D Gabor filter or other feature extraction methods (eg: 3D texture) could be used to provide 3D features and a 3D spline technique can be used to simulate 3D distortions.

3. In this thesis, clinician's opinions were used as the gold standard to assess the performance of proposed algorithms. However, the subjective judgments vary from person to person. To achieve an objective assessment and validate the results in a practical way, models can be built for simulation of the adaptive planning generated from the framework. Moreover, this work can include different dose planning techniques and dose boost on identified focal regions. The results could be assessed with the Dice coefficient evaluation proposed in this thesis.

4. A level set method was used as the last step in the framework to achieve the further segmentation on the target image because it can find the topology changes automatically and its initialization can be generated by the registration step. However, other segmentation algorithms (eg. shape model, region growing) have their own advantages and could be easily included in the framework. Specially, with accurate image registration method, atlas-based segmentation technique may achieve promising results [25].

Appendix A

MEDSIP abstract

Scale Invariant Image Registration for Focal Treatment of Prostate Cancer by Radiotherapy

Y. Feng[1], K. Cheng[1], Y. Tian[1], D.B. McLaren[1], S. McLaughlin[2], D.J. Argyle[3], W.H. Nailon[1]
[1]Edinburgh Cancer Centre, Western General Hospital, Edinburgh, UK
[2]School of Engineering and Physical Sciences, Heriot Watt University, Edinburgh, UK
[3]The Royal (Dick) School of Veterinary Studies, Edinburgh, UK

Introduction: Structural and functional imaging can provide disease-specific insights and assist in the management of cancer patients. In radiotherapy of the prostate, computerized tomography (CT) images are acquired to provide structural information and electron density information for dose calculation [1]. Positron emission tomography (PET) images and/or magnetic resonance (MR) images provide functional information to identify the biological features of tumour regions [2]. Planning CT data can be reconstructed to form digital reconstructed radiographies (DRR) which are direct representation of the planned treatment position [3]. Electronic portal imaging devices (EPID) provide a view of the patient at the treatment position. Mapping EPID images to DRR images will ensure that the patient is positioned in the correct location for treatment. However, it is difficult to map the information in images on different modalities. Image registration is the process of aligning two or more images of the same scene acquired at different times, viewpoints, and/or by different sensors [4]. In this paper a rigid registration method based on the scale invariant feature transform (SIFT), and mutual information (MI) approach, is presented. This method has been developed to register multi-modality image data from CT, MR, DRR and EPID to plan focal radiotherapy of the prostate. However, it is suitable for other multi-modality image registration problems.

Methodology: Matching common features in the source and target image can reduce computation in an image registration approach. However, it is difficult to identify suitable features acquired on different modalities because of differences in resolution, scale and position. SIFT is a method that can find key points and their descriptors in scale space and extract robust image features. Calculation of the mutual information of these features is a powerful indicator of image match. The method presented contains four stages: pre-processing; feature extraction with SIFT; calculation of MI; and optimization. The pre-processing stage includes segmentation of the regions of interest, de-noising, resampling of the original data set and the down-sampling of the resulting images. Each pre-processed image was selected as a flow data set and SIFT features extracted. The SIFT threshold for feature extraction was set to generate 50 features on every image slice. Therefore the problem of physical background and reconstruction field background pixels, which can significantly affect the accuracy of the MI-based method, was removed [5]. An affine transform was applied to the flow data set to alter the position of the features. The MI of the key feature points on the source image and the neighbouring points on the target image were calculated using (1), where P_A and P_B are the marginal, and P_{AB} the joint, probability distributions.

$$I(A,B) = \sum_{a,b} P_{AB}(a,b) \log \frac{P_{AB}(a,b)}{P_A(a) * P_B(b)} \quad (1)$$

Simulated annealing optimization was performed on the 7-dimensional parameter space (T_x T_y T_z α β γ scale) over a 1 pixel, 1° interval to find the global maximum representing the best match.

Results: Registration performance was assessed using CT and MR image data acquired on the Radionics Phantom 2 (Radionics, Inc., Burlington, MA), a geometric verification phantom that is used for quality assurance in stereotactic radiotherapy. The CT and MR data were mapped with an average error rate of 1.5% (Figure 1). The method was found to be x10 faster than conventional MI-based registration because fewer feature points are acquired (figure 2). EPID and DRR images from patients with prostate cancer are included in the test data as well. They can be appropriately registered as shown in figure 3.

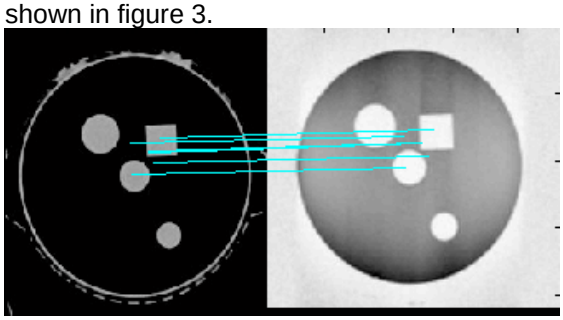

	T_x	T_y	T_z	α	γ	β
Actual	0	0	0	90	-90	0
Calculated	0	0	9	90	-90	0
Shift Range	100	100	100	/	/	/
Rotation Range	/	/	/	180	180	180
Error Rate	0	0	9%	0	0	0
Average Error Rate	1.5%					

Figure 1. Left: CT (left) and MR image (right) acquired on the Radionics Phantom 2，which is configured with a cone, cylinder, cube and sphere. The lines show corresponding SIFT features between CT and MR. Right: Affine transform parameters and results.

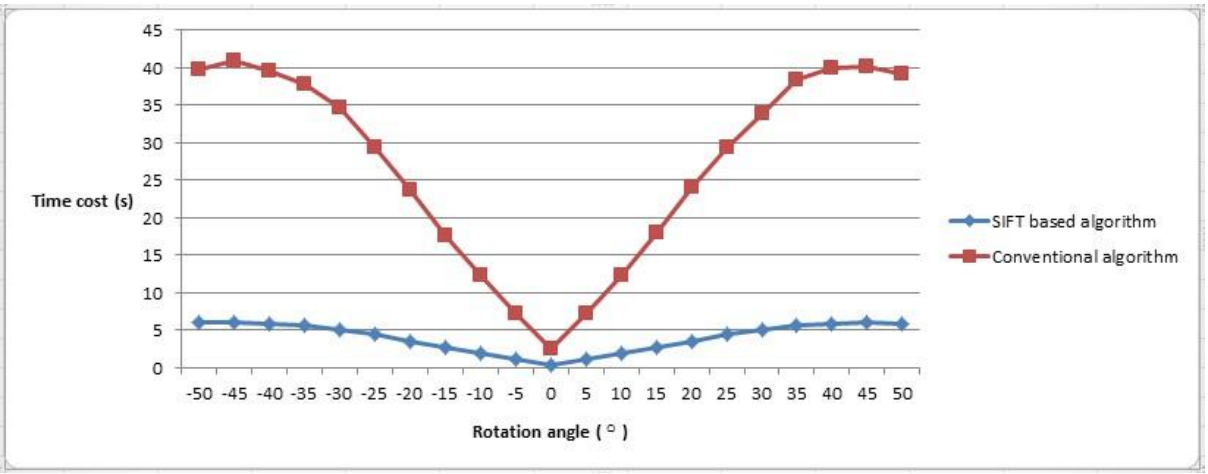

Figure 2. The registration time required by a SIFT based algorithm and a conventional algorithm on the test phantom data.

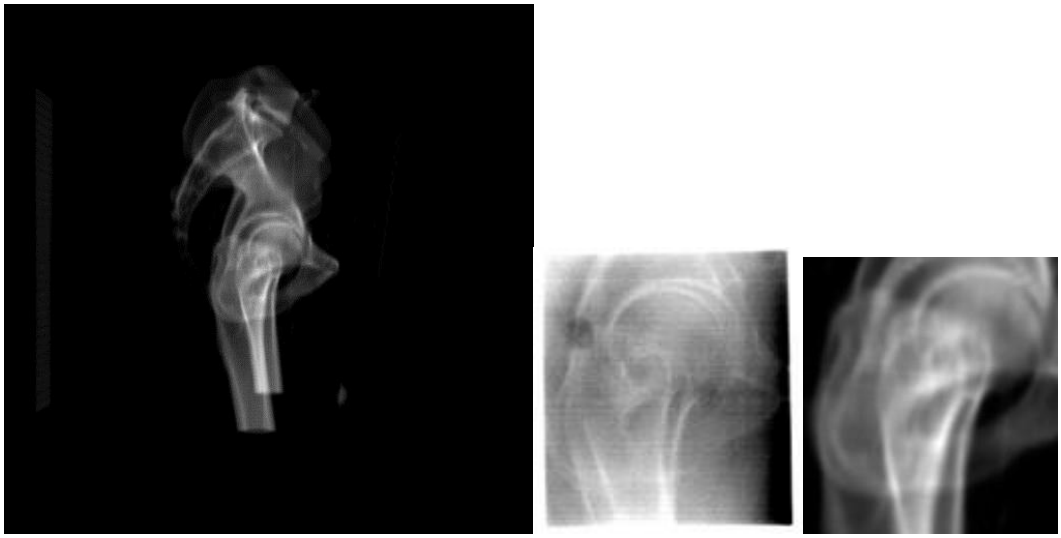

Figure 3. DRR image of the prostate area from patient with prostate cancer (512×512, left), EPID image of the same patient obtained during the radiotherapy treatment (244×244, mid) and the area of interest of registered image (244×244, right).

As shown in figure 3, the DRR and EPID images have different resolution, scale and noise. The registered image has generated with a scale factor of 2.16, a rotation angle of -5° and a shift parameter (T_x = 249, T_y = 233).

Conclusion: A method for registering multi-modality image data varying in size and scale has been presented. The method has been shown to work well on the registration between CT and MR phantom data and between EPID and DRR images.

Reference:

[1] P M Evans, “Anatomical imaging for radiotherapy.” Physics in Medicine and Biology Vol. 53(12), R151-R191.
[2] Ursula N, Wolfgang W, Michael H and Anca-Ligia G. “Biological imaging in radiation therapy: role of positron emission tomography.” Phys. Med. Biol. 54 (2009) R1–R25.
[3] N. S. Stanley, “The role of Digitally Reconstructed Radiographs in the verification process” Journal of Radiotherapy in Practice 1999 1,103-108.
[4] B. Zitová, J. Flusser, “Image registration methods: a survey.” Image Vision Comput, 21(11): 977-1000 (2003).
[5] D.G. Lowe, "Distinctive image features from scale-invariant key points." International Journal of Computer Vision, 60, 2 (2004), pp. 91-110.

Appendix B

MASSTRON abstract

SYMPOSIUM ON SMALL ANIMAL RADIOTHERAPY

ABSTRACT

Abstract title: **A NEW IMAGE REGISTRATION FRAMEWORK FOR FOCAL TREATMENT OF PROSTATE CANCER BY RADIOTHERAPY**

Authors: Y. Feng (1), K. Cheng (1), J. Lawrence (3), L. Forrest (4), D.B. McLaren (1), S. McLaughlin (2), D.J. Argyle (3), W.H. Nailon (1)

Affiliations :

(1) Edinburgh Cancer Centre, Western General Hospital, Edinburgh, EH4 2XU, UK

(2) School of Engineering and Physical Sciences, Heriot Watt University, Edinburgh, EH14 4AS, UK

(3) The Royal (Dick) School of Veterinary Studies, Edinburgh, EH25 9RG, UK

(4) The University of Wisconsin-Madison School of Veterinary Medicine, Madison, WI, USA

Email address presenting author: **s1031630@sms.ed.ac.uk**

Introduction:

Image registration is the process of aligning two or more images of the same scene acquired at different times, viewpoints, and/or by different sensors. A registration framework was designed to include both a rigid registration algorithm based on the scale invariant feature transform (SIFT) and mutual information (MI), and a non-rigid registration algorithm based on manually defined features and robust similarity function. This method has been developed to register multi-modality image data from computed tomography (CT), magnetic resonance (MR) and histology to plan focal radiotherapy of the prostate. Our hypothesis is that this framework is suitable for other multi-modality image registration problems.

Materials & Methods

SIFT is a method that can find key points and their descriptors in scale space and extract robust image features. Calculation of the MI of these features is a powerful indicator of image match. In the approach developed a rigid registration algorithm extracts feature points from the reference and target image data based on the SIFT algorithm and finds the best affine match by optimizing the MI of the SIFT features. Next a non-rigid registration algorithm is applied that uses the Euler distance between contour points and the MI between pathologically identified points as a robust similarity function. A fuzzy-to-deterministic approach is used to establish the match between feature points and a cubic B-spline method is applied after non-rigid transform. A posteriori weights for different data sets are used to adjust the similarity function and optimisation performed using simulated annealing and the Broyden–Fletcher–Goldfarb–Shanno (L-BFGS) method. Rigid registration performance was assessed using CT and MR image data acquired on the Radionics Phantom 2 (Radionics, Inc., Burlington, MA), a geometric verification phantom used for quality assurance in stereotactic radiotherapy. EPID and DRR images acquired from human prostate cancer patients were used. The non-rigid registration algorithm has been assessed on manually warped test images. The whole framework is additionally being tested on contemporaneous CT and MR series from dogs with sinonasal tumours.

Results

The mean error of the rigid method applied on the phantom data was less than 1.5% and was 10x faster than conventional MI-based registration. EPID and DRR images were registered within clinically acceptable limits. The similarity function provided a clear peak at the position of the best match between the reference and target images.

Conclusion

The rigid and non-rigid registration algorithms developed performed well on test image data. Preliminary evaluation supports the use of this framework for registration of canine nasal tumour CT and MR images and may prove useful in other tumour types. This approach is currently being investigated to establish the widespread applicability in radiation therapy.

Tick this box if you would prefer a poster ☐

Appendix C

VRU abstract

Image Registration in Veterinary Radiation Oncology: Indications, Implications and Future Advances

Yang Feng[1, 2], Jessica Lawrence[2], Kun Cheng[1], Dean Montgomery[1], Lisa Forrest[3], Duncan B. McLaren[1], Stephen McLaughlin[4], David J. Argyle[2], William H. Nailon[1]

[1]The University of Edinburgh, Department of Oncology Physics, Edinburgh Cancer Centre, Western General Hospital, Edinburgh, UK

[2]The University of Edinburgh, Royal (Dick) School of Veterinary Studies and Roslin Institute, UK

[3]The University of Wisconsin-Madison, Department of Surgical Sciences, 2015 Linden Drive, Madison WI, USA

[4]Heriot-Watt University, School of Engineering and Physical Sciences, Edinburgh, EH14 4AS, UK

Keywords: Oncology, Image Registration, Computed tomography, Radiation therapy, Magnetic resonance imaging

Running Head: Image Registration in Radiation Oncology

Funding Sources: This work was generously supported by NHS Lothian, Edinburgh and Lothians Health Foundation (charity number SC007342), the James Clerk

Maxwell Foundation, the Jamie King Uro-Oncology Endowment Fund, a University of Edinburgh Darwin Award and a University of Edinburgh Individual Stipend.

Previous Abstracts: Material has not previously been presented.

Abstract

The field of veterinary radiation therapy (RT) has gained substantial momentum in recent decades with significant advances in conformal treatment planning, image-guided radiation therapy (IGRT) and intensity-modulated (IMRT) techniques. At the root of these advancements lie improvements in tumor imaging, image alignment (registration), target volume delineation, and identification of critical structures. Image registration has been widely used to combine information from multi-modality images such as computerized tomography (CT), magnetic resonance imaging (MRI) and positron emission tomography (PET) to improve the accuracy of radiation delivery and reliably identify tumor-bearing areas. Many different techniques have been applied in image registration. This review provides an overview of medical image registration in RT and its applications in veterinary oncology. A summary of the most commonly used approaches in human and veterinary medicine is presented along with their current use in IGRT and adaptive radiation therapy (ART). It is important to realize that registration does not guarantee that target volumes, such as the gross tumor volume (GTV), are correctly identified on the image being registered as limitations unique to registration algorithms exist. Here, a novel registration-segmentation framework for automatic segmentation of the GTV on post-treatment CT images of veterinary patients has been developed and is described

with promising preliminary results based on dogs with primary nasal tumors presented to illustrate its efficacy.

Appendix D

ESTRO abstract

Title: Identifying Changes in the Gross Tumour Volume after Radiotherapy by Image Analysis

Authors: Y. Feng[1], K. Cheng[1], D. Montgomery[1], J. Lawrence[4], L. Forrest[5], D.B. McLaren[2], S. McLaughlin[3], D.J. Argyle[4] and W.H. Nailon[1]

[1]Western General Hospital, Edinburgh Cancer Centre, Department of Oncology Physics, Edinburgh, EH4 2XU, UK
[2]Western General Hospital, Edinburgh Cancer Centre, Department of Clinical Oncology, Edinburgh, EH4 2XU, UK
[3]School of Engineering and Physical Sciences, Heriot Watt University, David Brewster Building, Edinburgh, EH14 4AS, UK
[4]Royal (Dick) School of Veterinary Studies, University of Edinburgh, UK
[5]School of Veterinary Medicine, University of Wisconsin-Madison, Madison, WI, USA

Purpose/Objective

In radiotherapy (RT) identifying changes in the gross tumour volume (GTV) between pre-treatment magnetic resonance (MR), computed tomography (CT) and follow-up CT images is challenging. This is because of anatomical deformations, change in the GTV in response to RT and soft tissue contrast variability between CT and MR**.** Here a new approach for registration and segmentation of the GTV on multi-modality data acquired before, during and after RT, is presented. The approach was tested on MR and CT image data from client owned dogs undergoing RT because of the similarities between canine and human cancers and the opportunity that this presents for fast-tracking RT improvements into clinical practice for both patient groups.

Materials and Methods

Image data from two veterinary patients (P1 and P2) with nasal adenocarcinoma treated at the University of Wisconsin, School of Veterinary Medicine was used in this study. For P1, 4 data sets were available: pre-treatment T1-weighted MR (26 slices) and CT (39 slices); follow-up CT after 6 weeks (43 slices) and CT after 12 weeks (37 slices). For P2, 3 data sets were available: pre-treatment T1 weighted MR (20 slices) and CT (54 slices); follow-up CT after 12 weeks (51 slices). General Electric (GE Medical Systems, Milwaukee, WI, USA) Genesis and Signa scanners were used to acquire CT and MR data respectively. All CT images were acquired with 512 x 512 pixels of size: P1=0.31 x 0.31 mm, P2=0.39 x 0.39 mm. All MR images were acquired with 256 x 256 pixels of size 0.62 x 0.62 mm. The method developed comprises of a scale invariant feature transform (SIFT)-based rigid registration algorithm and a B-spline based non-rigid registration algorithm which are used to register pre- and post-treatment images. The registration result is next used as a prior in a gradient-based level set (LS) method for segmentation of the GTV on post-treatment images.

Results

The performance of the rigid registration algorithm was first established by rotating (Ω) and translating (T_x, T_y) CT and MR images from the same patient on which the GTV had been identified, both pre- and post-RT, by an experienced veterinary oncologist. The sum-of-squares difference (SSD) of the image intensity data and the SIFT feature points were compared to the MI of the image intensity data and the new

approach proposed, MI of SIFT. A match was defined when the clinical GTV contours and surrounding anatomical structures attained the maximum Dice coefficient, Table 1. In the next stage the performance of the non-rigid algorithm combined with LS segmentation of the GTV was investigated. Figure 1 shows typical results produced by the algorithm on pre- and post-RT CT, where the Dice coefficient was 88.01% over the whole volume.

Optimisation Parameter	**Rigid Registration Dice (%)**			
	SSD	**SSD of SIFT**	**MI**	**MI of SIFT**
Ω	0	37.97	0	76.07
(T_x, T_y)	73.93	0	0	76.07

Table 1: Dice coefficient calculated between clinically defined GTV contours on pre- and post-treatment CT and MR and GTV contours generated using the proposed algorithm. Measurements were computed over the range: $\Omega=(\pm 90°)$, $(T_x, T_y)=(\pm 40\%$ of the image size).

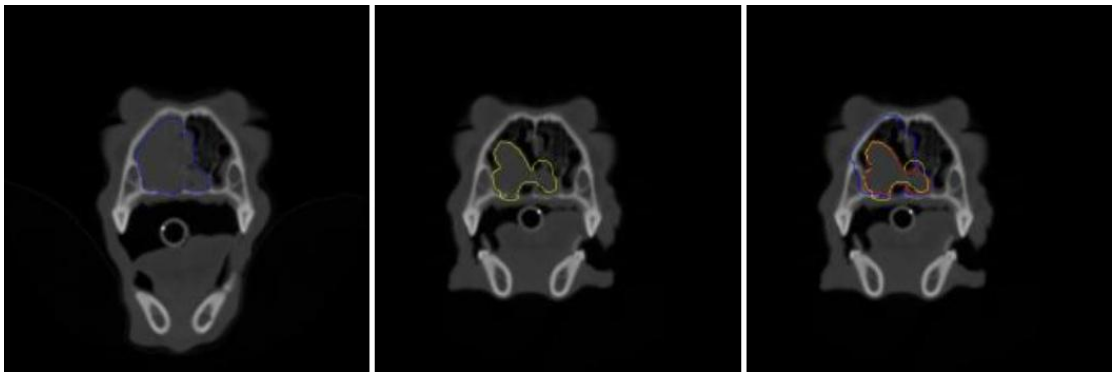

Figure 1: Left: Reference image with GTV contour (blue). Middle: target image with GTV contour (yellow). Right: The automatically generated contour (red) and the original GTV contour (yellow). The blue contour shows the reference image GTV expanded and used as the initial zero LS function.

Conclusions

The proposed registration-segmentation framework demonstrates that by using prior information from pre-treatment images it is possible to automatically segment the GTV on post-radiotherapy images with acceptable clinical accuracy (Dice = 88.01%). Work is ongoing to assess the performance of the approach on a larger human and canine data set and using other imaging modalities such as positron emission tomography (PET). On this limited data set the approach shows promise as a tool for assisting clinicians define the GTV over time in response to RT and has the potential to be used for adaptive radiotherapy.

Keywords: Adaptive Radiotherapy, Image Segmentation, Image Registration

Bibliography

[1] Dicom part 3, ps3.3 - service class specifications.

[2] ICRU report 62. prescribing, recording, and reporting photon beam therapy (supplement to ICRU report 50). Technical report, International Commission on Radiation Unites and Measurements, 1999.

[3] Magnetic resonance, a critical peer-reviewed introduction. Technical report, European Magnetic Resonance Forum, 2013.

[4] D. Adalsteinsson and J. A. Sethian. A fast level set method for propagating interfaces. *Journal of Computational Physics*, 118:269–277, 1995.

[5] R. Alterovitz, K. Goldberg, J. Pouliot, I. C. Hsu, Y. Kim, S. M. Noworolski, and J. Kurhanewicz. Registration of MR prostate images with biomechanical modeling and nonlinear parameter estimation. *Medical Physics*, 33(2):446–454, 2006.

[6] A. A. Amini, T. E. Weymouth, and R. C. Jain. Using dynamic programming for solving variational problems in vision. *IEEE Transactions on Pattern Analysis and Machine Intelligence*, 12(9):855–867, 1990.

[7] M. Andreetto, G. M. Cortelazzo, and L. Lucchese. Frequency domain registration of computer tomography data. In *The 2nd International Symposium on 3D Data Processing, Visualization and Transmission*, 2004.

[8] F. Argenti, L. Alparone, and G. Benelli. Fast algorithm for texture analysis using co-occurrence matrices. In *IEEE Proceedings Part F on Radar Signal Processing*, 1990.

[9] J. J. Aristu, R. Ciervide, J. Guridi, M. Moreno, L. Arbea, J. D. Azcona, L. I. Ramos, and J. L. Zubieta. Stereotactic radiation therapy. *Anales del Sistema Sanitario de Navarra*, 32:61–71, 2009.

[10] J. Ashburner and K. J. Friston. Nonlinear spatial normalization using basis functions. *Human Brain Mapping*, 7:254–266, 1999.

[11] D. L. Bailey, D. W. Townsend, P. E. valk, and M. N. Maisey, editors. *Positron Emission Tomography: Basic Sciences*. Springer Science & Business Media, 2003.

[12] P. G. C. Begemann. Ct-guided interventions: Indications, technique, and pitfalls. In *CT-and MR-Guided Interventions in Radiology*, pages 11–24. Springer, 2013.

[13] B. Belletti and J. S. Vaidya. Targeted intraoperative radiotherapy impairs the stimulation of breast cancer cell proliferation and invasion caused by surgical wounding. *Clinical Cancer Research*, 14:1325–1332, 2008.

[14] M. Birkner, D. Yan, M. Alber, J. Liang, and F. Nusslin. Adapting inverse planning to patient and organ geometrical variation: algorithm and implementation. *Medical Physics*, 30(10):2822–2831, 2003.

[15] S. R. Bowen, R. J. Chappell, S. M. Bentzen, M. A. Deveau, L. J. Forrest, and R. Jeraj. Spatially resolved regression analysis of pre-treatment FDG, FLT and Cu-ATSM PET from post-treatment PDG PET: an exploratory study. *Radiotherapy and Oncology*, 105: 41–48, 2012.

[16] T. J. Bradshaw, S. R. Bowen, N. Jallow, L. J. Forrest, and R. Jaraj. Heterogeneity in intratumor correlations of 18F-FDG, 18-FLT, and 61Cu-ATSM PET in canine sinonasal tumors. *Journal of Nuclear Medicine*, 54:1917–1931, 2013.

[17] T. J. Bradshaw, S. Yip, N. Jallow, L. J. Forrest, and R. Jeraj. Spatiotemporal stability of Cu-ATSM and FLT positron emission tomography distributions during radiation therapy. *International Journal of Radiation Oncology, Biology, Physics*, 89(2):399–405, 2014.

[18] L. W. Brady and T. E. Yaeger, editors. *Encyclopedia of radiation oncology*. Springer Berlin Heidelberg, 2013.

[19] D. J. Brenner and E. J. Hall. Computed tomography–an increasing source of radiation exposure. *New England Journal of Medicine*, 357:2277–2284, 2007.

[20] T. Butz and J. P. Thiran. Affine registration with feature space mutual information. In *The 4th International Conference on Medical Image Computing and Computer-Assisted Intervention*, 2001.

[21] L. Y. Carreon, S. D. Glassman, J. D. Schwender, B. R. Subach, M. F. Gornet, and S. Ohno. Reliability and accuracy of fine-cut computed tomography scans to determine the status of anterior interbody fusions with metallic cages. *The Spine Journal*, 8(6): 998–1002, 2008.

[22] B. B. Chaudhuri and N. Sarkar. Texture segmentation using fractal dimension. *IEEE Transactions on Pattern Analysis and Machine Intelligence*, 17:72–77, 1995.

[23] D. L. Collins and A. C. Evans. ANIMAL: validation and applications of non-linear registration-based segmentation. *International Journal of Pattern Recognition and Artificial Intelligence*, 11(8):1271–1294, 1997.

[24] L. E. Court, R. B. Tishler, J. Petit, R. Cormack, and L. Chin. Automatic online adaptive radiation therapy techniques for targets with significant shape change: a feasibility study. *Physics in Medicine and Biology*, 51(10):2493–2501, 2006.

[25] M. B. Cuadra, M. D. Craene, and V. Duay. Dense deformation field estimation for Atlas-based segmentation of pathological MR brain images. *Computer Methods and Programs in Biomedicine*, 84:67–75, 2006.

[26] M. D. den Hartogh. Towards mri-guided radiotherapy in early-stage breast cancer patients. 2014.

[27] B. Djavan, M. Susani, A. Basharkhah, R. Simak, and M. Marberger. Predictability and significance of multifocal prostate cancer in the radical prostatectomy specimen. *Techniques in Urology*, 5:139–142, 1999.

[28] R. O. Duda, P. E. Hart, and D. G. Stork. *Pattern classification*. Wiley, 2001.

[29] E. A. Eisenhauer, P. Therasse, J. Bogaerts, L. H. Schwartz, D. Sargent, R. Ford, J. Dancey, S. Arbuck, S. Gwyther, M. Mooney, L. Rubinstein, L. Shankar, L. Dodd, R. Kaplan, D. Lacombe, and J. Verweij. New response evaluation criteria in solid tumours: revised RECIST guideline (version 1.1). *European Journal of Cancer*, 45: 228–247, 2009.

[30] L. Fass. Imaging and cancer: a review. *Molecular oncology*, 2(2):115–152, 2008.

[31] G. H. Fletcher. *Textbook of radiotherapy*. Lea & Febiger, 1973.

[32] P. A. Freeborough and N. C. Fox. Modeling brain deformations in alzheimer disease by fluid registration of serial 3D MR images. *Journal of Computer Assisted Tomography*, 22(5):838–843, 1998.

[33] K. J. Friston, J. Ashburner, J. B. Poline, C. D. Frith, J. D. Heather, and R. S. J. Frackowiak. Spatial registration and normalization of images. *Human Brain Mapping*, 2:165–189, 1995.

[34] J. M. Galvin, G. Ezzell, and A. Eisbrauch. Implementing IMRT in clinical practice: a joint document of the American Society for Therapeutic Radiology and Oncology and the American Association of Physicists in Medicine. *International Journal of Radiation Oncology, Biology, Physics*, 58(5):1616–1634, 2004.

[35] S. Gefen, O. Tretiak, and J. Nissanov. Elastic 3D alignment of rat brain histological images. *IEEE Transactions on Medical Imaging*, 22(11):1490–1489, 2003.

[36] D. T. Gering, A. Nabavi, R. Kikinis, W. E. L. Grimson, N. Hata, P. Everett, F. Jolesz, and W. M. Wells. An integrated visualization system for surgical planning and guidance using image fusion and interventional imaging. In *The 2nd International Conference on Medical Image Computing and Computer-Assisted Intervention*, 1999.

[37] M. J. Gooding, K. Rajpoot, S. Mitchell, P. Chamberlain, S. H. Kennedy, and J. A. Noble. Investigation into the fusion of multiple 4D fetal echocardiography images to improve image quality. *Ultrasound in Medicine and Biology*, 36(6):957–966, 2010.

[38] C. Grau and L. P. Muren. Image-guided adaptive radiotherapy - integration of biology and technology to improve clinical outcome. *Acta Oncologica*, 47:1182–1185, 2008.

[39] H. Gray. *Anatomy of the human body*. Lea & Febiger, 1918.

[40] M. V. Green, J. Seidel, J. J. Vaquero, E. Jagoda, I. Lee, and W. C. Eckelman. High resolution PET, SPECT and projection imaging in small animals. *Computerized Medical Imaging and Graphics*, 25(2):79–86, 2001.

[41] N. M. Grosland, R. Bafna, and V. A. Magnotta. Automated hexahedral meshing of anatomic structures using deformable registration. *Computer Methods in Biomechanics and Biomedical Engineering*, 12(1):35–43, 2009.

[42] M. Haghighat, S. Zonouz, and M. Abdel-Mottaleb. Identification using encrypted biometrics. In *The 15th International Conference of Computer Analysis of Images and Patterns, Lecture Notes in Computer Science*, 2013.

[43] Hall and J. Eric. *Radiobiology for the radiologist*. Philadelphia: Lippincott Williams Wilkins, 2000.

[44] E. J. Hall and C. S. Wuu. Radiation-induced second cancers: the impact of 3D-CRT and IMRT. *International Journal of Radiation Oncology, Biology, Physics*, 56(1):83–88, 2003.

[45] A. E. Hansen, F. McEvoy, S. A. Engelholm, I. Law, and A. T. Kristensen. FDG PET/CT imaging in canine cancer patients. *Veterinary Radiology and Ultrasound*, 52:201–206, 2011.

[46] R. M. Haralick and L. G. Shapiro. Image segmentation techniques. *Computer Vision, Graphics, and Image Processing*, 29:100–132, 1985.

[47] J. Harmon, H. Yoshikawa, J. Custis, and S. LaRue. Evlauation of canine prostate intrafractional motion using serial cone beam computed tomography imaging. *Veterinary Radiology and Ultrasound*, 54:93–98, 2013.

[48] C. Harris and M. Stephens. A combined corner and edge detector. In *Alvey vision conference*, volume 15, page 50. Citeseer, 1988.

[49] L. B. Harrison, M. Chadha, R. J. Hill, K. Hu, and D. Shasha. Impact of tumor hypoxia and anemia on radiation therapy outcomes. *Oncologist*, 7(6):492–508, 2002.

[50] N. Hayakawa, K. Uemura, K. Ishiwata, Y. Shimada, N. Ogi, and T. Nagaoka. A PET-MRI registration technique for PET studies of the rat brain. *Nuclear Medicine and Biology*, 27(2):121–125, 2000.

[51] P. Hellier and C. Barillot. A hierarchical parametric algorithm for deformable multimodal image registration. *Computer Methods and Programs in Biomedicine*, 75(2): 107–115, 2004.

[52] G. T. Herman. *Fundamentals of Computerized Tomography: Image Reconstruction from Projections*. Springer Science & Business Media, 2009.

[53] H. S. Jans, A. M. Syme, S. Rathee, and B. G. Fallone. 3D interfractional patient position verification using 2D-3D registration of orthogonal images. *Medical Physics*, 33(5): 1420–1439, 2006.

[54] M. Jenkinson and S. Smith. A global optimization method for robust affine registration of brain images. *Medical Image Analysis*, 5(2):143–156, 2001.

[55] M. Jobse, J. Davelaar, E. Hendriks, R. Kattevilder, H. Reiber, and B. Stoel. New algorithm for the registration of portal images to planning images in the verification of radiotherapy, as validated in prostate treatments. *Medical Physics*, 30(9):2274–2281, 2003.

[56] C. A. Johnson, J. Seidel, R. E. Carson, W. R. Gandler, A. Sofer, M. V. Green, and M. E. Daube-Witherspoon. Evaluation of 3D reconstruction algorithms for a small animal PET camera. *IEEE Transactions on Nuclear Science*, 44(3):1303–1308, 1997.

[57] H. J. Johnson and M. McCormick. *ITK software guide*, 2013.

[58] A. A. Joshi, A. J. Chaudhan, C. Li, J. Dutta, S. R. Cherry, D. W. Shattuck, A. W. Toga, and R. M. Leahy. DigiWarp: a method for deformable mouse atlas warping to surface topographic data. *Physics in Medicine and Biology*, 55(20):6197–6214, 2010.

[59] H. Kalvian, P. Hirvonen, L. Xu, and E. Oja. Probabilistic and non-probabilistic Hough transform: Overview and comparisons. *Image and Vision Computing*, 13:239–252, 1995.

[60] M. Kass, A. Witkin, and D. Terzopoulos. Snakes: Active contour models. *International Journal of Computer Vision*, 1(4):321–331, 1988.

[61] M. S. Kent, I. K. Gordon, I. Benavides, P. Primas, and J. Young. Assessment of the accuracy and precision of a patient immobilization device for radiation therapy in canine head and neck tumors. *Veterinary Radiology and Ultrasound*, 50:550–554, 2009.

[62] M. L. Kessler. Image registration and data fusion in radiation therapy. *British Journal of Radiology*, 79:s99–s108, 2006.

[63] M. L. Kessler, S. Pitluck, P. L. Petti, and J. R. Castro. Integration of multimodality imaging data for radiotherapy treatment planning. *International Journal of Radiation Oncology, Biology, Physics*, 21:1653–1667, 1991.

[64] M. A. Keyerleber, M. C. McEntee, J. Farrelly, and M. Podgorsak. Completeness of reporting of radiation therapy planning, dose, and delivery in veterinary radiation oncology. *Veterinary Radiology and Ultrasound*, 53:221–230, 2012.

[65] S. Klein, M. Staring, and J. P. W. Pluim. Evaluation of optimization methods for non-rigid medical image registration using mutual information and B-splines. *IEEE Transactions on Image Processing*, 16(12):2879–2890, 2007.

[66] R. Kong and B. Zhang. Design of Gabor filter's parameter. *Control and Decision*, 27: 1277–1280, 2012.

[67] L. N. Kubicek, S. Seo, R. J. . Chappell, R. Jeraj, and L. J. Forrest. Helical tomotherapy setup variations in canine nasal tumor patients immobilized with a bite block. *Veterinary Radiology and Ultrasound*, 53:474–481, 2012.

[68] J. J. W. Lagendijk, B. W. Raaymakers, A. J. E. Raaijmakers, J. Overweg, K. J. Brown, and e. a. E. M. Kerkhof. Mri/linac integration. *Radiotherapy and Oncology*, 86(1): 25–29, 2008.

[69] S. M. LaRue and I. K. Gordon. *Radiation Therapy. In: Small Animal Clinical Oncology, 5th ed.* Elsevier Inc, 2013.

[70] W. C. Lavely, C. Scarfone, H. Cevikalp, R. Li, D. W. Byrne, and A. J. Cmelak. Phantom validation of co-registration of PET and CT for image-guided radiotherapy. *Medical Physics*, 31(4):1083–1092, 2004.

[71] J. Lawrence, M. Vanderhoek, D. Barbee, R. Jeraj, D. B. Tumas, and D. M. Vail. Use of 3'-deoxy-3'-[18F] fluorothymidine PET/CT for evaluating response to cytotoxic chemotherapy in dogs with non-Hodgkin's lymphoma. *Veterinary Radiology and Ultrasound*, 50:660–668, 2009.

[72] J. A. Lawrence, L. J. Forrest, M. M. Turek, P. E. Miller, T. R. Mackie, H. A. Jaradat, D. M. Vail, R. R. Dubielzig, R. Chappell, and M. P. Mehta. Proof of principle of ocular sparing in dogs with sinonasal tumors treated with intensity-modulated radiation therapy. *Veterinary Radiology and Ultrasound*, 51:561–570, 2012.

[73] A. K. LeBlanc and K. Peremans. PET and SPECT imaging in veterinary medicine. *Seminars in Nuclear Medicine*, 44:47–56, 2014.

[74] A. K. LeBlanc, B. W. Jakoby, D. W. Townsend, and G. B. Daniel. 18FDG-PET imaging in canine lymphoma and cutaneous mast cell tumor. *Veterinary Radiology and Ultrasound*, 50:215–223, 2009.

[75] A. K. LeBlanc, A. N. Miller, G. D. Galyon, T. D. Moyers, M. J. Long, A. C. Stuckey, J. S. Wall, and F. Morandi. Preliminary evaluation of serial 18F FDG-PET/CT to assess response to toceranib phosphate therapy in canine cancer. *Veterinary Radiology and Ultrasound*, 53:348–357, 2012.

[76] T. Li, X. Zhu, D. Thongphiew, W. R. Lee, Z. Vujaskovic, Q. Wu, F. F. Yin, and Q. J. Wu. On-line adaptive radiation therapy: feasibility and clinical study. *Journal of Oncology*, doi:10.1155/2010/407236, 2010.

[77] H. Livyatan, Z. Yaniv, and L. Joskowicz. Gradient-based 2-D/3-D rigid registration of fluoroscopic X-ray to CT. *IEEE Transactions on Medical Imaging*, 22(11):1395–1406, 2003.

[78] D. G. Lowe. Distinctive image features from scale-invariant keypoints. *International Journal of Computer Vision*, 60(2):91–110, 2004.

[79] F. Maes, A. Collignon, D. Vandermeulen, G. Marchal, and P. Suetens. Multimodality medical image registration by maximization of mutual information. *IEEE Transactions on Medical Imaging*, 16(2):187–198, 1997.

[80] J. B. A. Maintz and M. A. Viergever. A survey of medical image registration. *Medical Image Analysis*, 2(1):1–36, 1998.

[81] D. Maksimov, J. Hesser, C. Brockmann, S. Jochum, T. Dietz, A. Schnitzer, C. Duber, S. O. Schoenberg, and S. Diehl. Graph-matching based CTA. *IEEE Transactions on Medical Imaging*, 28(12):1940–1954, 2009.

[82] R. Malladi, J. A. Sethian, and B. C. Vemuri. Shape modeling with front propagation: a level set approach. *IEEE Transactions on Pattern Analysis and Machine Intelligence*, 17(2):158–175, 1995.

[83] B. Martin, M. Julien, D. Jouke, D. H. Tobias, W. W. Axel, Q. Ivo, L. K. Eric, W. G. M. L. Clemens, H. C. R. Johan, and P. F. l. Boudewijn. Atlas-based whole-body segmentation of mice from low-contrast Micro-CT data. *Medical Image Analysis*, 14(5):723–737, 2010.

[84] D. Mattes, D. R. Haynor, H. Vesselle, T. K. Lewellen, and W. Eubank. PET-CT image registration in the chest using free-form deformations. *IEEE Transactions on Medical Imaging*, 22(1):120–128, 2003.

[85] C. R. Maurer, J. M. Fitzpatrick, M. Y. Wang, R. L. Galloway, R. J. Maciunas, and G. S. Allen. Registration of head volume images using implantable fiducial markers. *IEEE Transactions on Medical Imaging*, 16(4):447–462, 1997.

[86] M. C. McEntee. Portal radiography in veterinary radiation oncology: options and considerations. *Veterinary Radiology and Ultrasound*, 49:s57–s61, 2009.

[87] C. R. Meyer, J. L. Boes, K. Boklye, P. H. Bland, K. R. Zasadny, P. V. Kison, K. Koral, K. A. Frey, and R. L. Washl. Demonstration of accuracy and clinical versatility of mutual information for automatic multimodality image fusion using affine and thin-plate spline warped geometric deformations. *Medical Image Analysis*, 1(3):195–206, 1997.

[88] X. Ming, Y. Feng, Y. Guo, and C. Yang. A new automatic segmentation method for lung tumor based on suv threshold on 18 f-fdg pet images. In *2012 IEEE International Conference on Virtual Environments Human-Computer Interfaces and Measurement Systems (VECIMS)*, pages 5–8. IEEE, 2012.

[89] J. Modersitzki. *FAIR: Flexible algorithms for image registration*. Institute of Mathematics and Image Computing, University of Lübeck, Germany.

[90] S. Murphy, A. Gutierrez, J. Lawrence, D. Bjorling, T. Mackie, and L. Forrest. Laparoscopically implanted tissue expander radiotherapy in canine transitional cell carcinoma. *Veterinary Radiology and Ultrasound*, 49:400–405, 2008.

[91] J. R. Nieset, J. F. Harmon, and S. M. LaRue. Use of cone-beam computed tomography to characterize daily urinary bladder variations during fractionated radiotherapy for canine bladder cancer. *Veterinary Radiology and Ultrasound*, 52:580–588, 2011.

[92] C. Nikou, F. Heitz, and J. P. Armspach. Robust voxel similarity metrics for the registration of dissimilar single and multimodal images. *Pattern Recognition*, 32:1351–1368, 1999.

[93] M. W. Nolan, L. Kogan, L. R. Griffin, J. T. Custis, J. F. Harmon, B. J. Biller, and S. M. LaRue. Intensity-modulated and image-guided radiation therapy for treatment of genitourinary carcinomas in dogs. *Journal of Veterinary Internal Medicine*, 26:987–995, 2012.

[94] C. A. Pelizzari, G. T. Chen, D. R. Spelbring, and R. R. Weichselbaum. Accurate three-dimensional registration of CT, PET, and/or MR images of the brain. *Journal of Computer Assisted Tomography*, 13:20–26, 1989.

[95] S. Periaswamy and H. Farid. Elastic registration in the presence of intensity variations. *IEEE Transactions on Medical Imaging*, 22(7):865–874, 2003.

[96] M. Peroni, D. Ciardo, M. F. Spadea, M. Riboldi, S. Comi, D. Alterio, G. Baroni, and R. Orecchia. Automatic segmentation and online virtual CT in head-and-neck adaptive radiation therapy. *International Journal of Radiation Oncology, Biology, Physics*, 84(3): 427–433, 2012.

[97] J. P. M. Pluim and J. M. Fitzpatrick. Image registration. *IEEE Transactions on Medical Imaging*, 22(11):1341–1343, 2003.

[98] E. B. Podgorsak, editor. *Radiation oncology physics: a handbook for teachers and students*. International Atomic Energy Agency, 2005.

[99] M. Pourhomayoun, M. L. Fowler, and Z. Jin. A novel method for tumor localization and tracking in radiation therapy. In *IEEE Asilomar Conference on Signals, Systems and Computers*, 2012.

[100] J. L. Prince and J. M. Links. *Medical imaging signals and system*. Pearson Education, 2006.

[101] N. Ramesh, J. H. Yoo, and I. K. Sethi. Thresholding based on histogram approximation. In *IEEE Proceedings on Vision, Image and Signal Processing*, 1995.

[102] E. Randall, S. Loeber, and S. Kraft. Physiologic variants, benign processes, and artifacts from 106 canine and feline FDG-PET/computed tomography scans. *Veterinary Radiology and Ultrasound*, 55:213–226, 2014.

[103] E. Ricci and R. Perfetti. Retinal blood vessel segmentation using line operators and support vector classification. *IEEE Transactions on Medical Imaging*, 26(10):1357–1365, 2007.

[104] T. Rohlfing and C. R. Maurer. Intensity-based nonrigid registration using adaptive multilevel free-form deformation with an incompressibility constraint. In *The 4th International Conference on Medical Image Computing and Computer-Assisted Intervention*, 2001.

[105] B. C. Rohrer, A. Sumova, M. Roos, and B. Kaser-Hotz. Irradiation of brain tumors in dogs with neurologic disease. *Journal of Veterinary Internal Medicine*, 19:849–854, 2005.

[106] D. Rueckert, L. I. Sonoda, C. Hayes, D. L. G. Hill, M. O. Leach, and D. J. Hawkes. Non-rigid registration using free-form deformations: application to breast MR images. *IEEE Transactions on Medical Imaging*, 18(8):712–721, 1999.

[107] A. E. Sakdinawat, K. Iwata, A. B. Hwang, H. R. Tang, K. H. Wong, and B. H. Hasegawa. Development of external fiducial markers for image registration in small animal SPECT/CT. *IEEE Nuclear Science Symposium conference record*, 2:842–845, 2002.

[108] B. Schaly, J. A. Kempe, G. S. Bauman, J. J. Battista, and J. V. Dyk. Tracking the dose distribution in radiation therapy by accounting for variable anatomy. *Physics in Medicine and Biology*, 49(5):791–805, 2004.

[109] J. A. Schnabel, C. Tanner, A. D. Castellano-Smith, A. Degenhard, O. L. Martin, D. R. Hose, D. L. G. Hill, and D. J. Hawkes. Validation of nonrigid image registration using finite element methods: application to breast MR images. *IEEE Transactions on Medical Imaging*, 22(2):238–247, 2003.

[110] M. D. Seemann. Whole-body pet/mri: the future in oncological imaging. *Technology in cancer research & treatment*, 4(5):577–582, 2005.

[111] J. A. Sethian and J. Strain. Crystal growth and dendritic solidification. *Journal of Computational Physics*, 98(2):231–253, 1992.

[112] N. Sharma and L. M. Aggarwa. Automated medical image segmentation techniques. *Journal of Medical Physics*, 35(1):3–14, 2010.

[113] N. Sharma and A. K. Ray. Computer aided segmentation of medical images based on hybridized approach of edge and region based techniques. In *Proceedings of International Conference on Mathematical Biology*, 2006.

[114] D. Shen and C. Davatzikos. HAMMER: hierarchical attribute matching mechanism for elastic registration. *IEEE Transactions on Medical Imaging*, 21(11):1421–1439, 2002.

[115] Y. Shimada, K. Uemura, B. A. Ardekani, T. Nagaoka, K. Ishiwata, H. Toyama, K. Ono, and M. Senda. Application of PET-MRI registration techniques to cat brain imaging. *Journal of Neuroscience Methods*, 101(1):1–7, 2000.

[116] J. J. Sonke and J. Belderbos. Adaptive radiotherapy for lung cancer. *Seminars in Radiation Oncology*, 20(2):94–106, 2010.

[117] P. Spyridonos, D. Cavouras, P. Ravazoula, and G. Nikiforidis. Neural network-based segmentation and classification system for automated grading of histologic sections of bladder carcinoma. *Analytical and Quantitative Cytology and Histology*, 24(6):317–324, 2002.

[118] C. Studholme, D. L. G. Hill, and D. J. Hawkes. An overlap invariant entropy measure of 3D medical image alignment. *Pattern Recognition*, 32(1):71–86, 1999.

[119] C. Studholme, R. T. Constable, and J. S. Duncan. Accurate alignment of functional EPI data to anatomical MRI using a physics-based distortion model. *IEEE Transactions on Medical Imaging*, 19(11):1115–1127, 2000.

[120] D. Thongphiew, Q. J. Wu, W. R. Lee, V. Chankong, S. Yoo, R. McMahon, and F. F. Yin. Comparison of online IGRT techniques for prostate IMRT treatment: adaptive vs repositioning correction. *Medical Physics*, 36(5):1651–1662, 2009.

[121] K. R. Thulborn, J. C. Waterton, P. M. Matthews, and G. K. Radda. Oxygenation dependence of the transverse relaxation time of water protons in whole blood at high field. *Biochimica et Biophysica Acta*, 714(2):265–270, 1982.

[122] M. Unser. Texture classification and segmentation using wavelet frames. *IEEE Transactions on Image Processing*, 4(11):1549–1560, 1995.

[123] T. Vercauteren, X. Pennec, A. Perchant, and N. Ayache. Nonparametric diffeomorphic image registration with the demons algorithm. In *The 10th International Conference on Medical Image Computing and Computer-Assisted Intervention*, 2007.

[124] P. A. Viola and W. M. Wells. Alignment by maximization of mutual information. In *The 5th International Conference on Computer Vision*, 1995.

[125] M. T. Vlaardingerbroek and J. A. Boer. *Magnetic resonance imaging: theory and practice*. Springer Science & Business Media, 2013.

[126] C. Vollmar, J. O'Muircheartaigh, G. J. Barker, M. R. Symms, P. Thompson, V. Kumari, J. S. Duncan, M. P. Richardson, and m. j. Koepp. Identical, but not the same: intra-site and inter-site reproducibility of fractional anisotropy measures on two 3.0 t scanners. *Neuroimage*, 51(4):1384–1394, 2010.

[127] H. A. Vrooman, C. A. Cocosco, F. Lijn, R. Stokking, M. A. Ikram, M. W. Vernooij, M. M. Breteler, and W. J. Niessen. Multi-spectral brain tissue segmentation using automatically trained k-nearest-neighbor classification. *NeuroImage*, 37(1):71–81, 2007.

[128] M. Wildeman, M. Baiker, M. J. T. Reinders, C. W. G. M. Lowik, J. H. C. Reiber, and B. P. F. Lelieveldt. 2D/3D registration of micro-CT data to multi-view photographs based on a 3D distance map. In *IEEE International Symposium on Biomedical Imaging*, 2009.

[129] D. J. Withey and Z. J. Koles. Three generations of medical image segmentation: Methods and available software. *International Journal of Bioelectromagnetism*, 9:67–68, 2007.

[130] S. K. Woo, K. M. Kim, T. Lee, J. Y. Kim, J. H. Jung, K. S. Woo, W. S. Jung, J. H. Kang, G. J. Cheon, C. W. Choi, and S. M. Lim. Experimental condition and registration method for the tumor detection of lung metastasis small animal PET and CT whole body images. *IEEE Nuclear Science Symposium conference record*, 5:3372–3375, 2007.

[131] Q. Wu, G. Ivaldi, J. Liang, D. Lockman, D. Yan, and A. Martinez. Geometric and dosimetric evaluations of an online image-guidance strategy for 3D-CRT of prostate cancer. *International Journal of Radiation Oncology, Biology, Physics*, 64(5):1596–1609, 2006.

[132] D. Yan, F. Vicini, J. Wong, and A. Martinez. Adaptive radiation therapy. *Physics in Medicine and Biology*, 42(1):123–132, 1997.

[133] C. C. Yang, T. H. Wu, M. H. Lin, Y. H. Huang, W. Y. Guo, C. L. Chen, T. C. Wang, W. H. Yin, and J. S. Lee. Multimodality imaging combination in small animal via point-based registration. *Nuclear Instruments and Methods in Physics Research Section A*, 569(2): 240–244, 2006.

[134] H. Yoshikawa, E. K. Randall, S. L. Kraft, and S. M. LaRue. Comparison between 2-18F-fluoro-2-deoxy-D-glucose positron emission tomography and contrast-enhanced computed tomography for measuring gross tumor volume in cats with oral squamous cell carcinoma. *Veterinary Radiology and Ultrasound*, 54:307–313, 2013.

[135] M. J. Zelefsky, Z. Fuks, L. Happersett, H. J. Lee, C. C. Ling, C. M. Burman, M. Hunt, T. Wolfe, E. S. Venkatraman, and A. Jackson. Clinical experience with intensity modulated radiation therapy (imrt) in prostate cancer. *Radiotherapy and Oncology*, 55 (3):241–249, 2000.

[136] X. Zheng, H. Xishi, Z. Xiaobo, S. Youxian, N. Vasilis, and T. C. W. Stephen. Registration of 3-D CT and 2-D flat images of mouse via affine transformation. *IEEE Transactions on Information Technology in Biomedicine*, 12(5):569–578, 2008.

[137] O. Zvitia, A. Mayer, R. Shadmi, S. Miron, and H. K. Greenspan. Co-registration of white matter tractographies by adaptive-mean-shift and gaussian mixture modeling. *IEEE Transactions on Medical Imaging*, 29(1):132–145, 2010.